

A MULTI-BAND METAMATERIAL ABSORBER DESIGN FOR SOLAR CELL  
APPLICATIONS

A THESIS SUBMITTED TO THE BOARD OF GRADUATE PROGRAMS

OF

MIDDLE EAST TECHNICAL UNIVERSITY, NORTHERN CYPRUS CAMPUS

BY

BATUHAN MULLA

IN PARTIAL FULFILLMENT OF THE REQUIREMENTS

FOR

THE DEGREE OF MASTER OF SCIENCE

IN

SUSTAINABLE ENVIRONMENT AND ENERGY SYSTEMS

AUGUST 2016

Approval of the Board of Graduate Programs

\_\_\_\_\_  
Prof. Dr. Tanju Mehmetođlu  
Chair person

I certify that this thesis satisfies all the requirements as a thesis for the degree of Master of Science.

\_\_\_\_\_  
Assoc. Prof. Dr. Ali Muhtarogđlu  
Program Coordinator

This is to certify that we have read this thesis and that in our opinion it is fully adequate, in scope and quality, as a thesis for the degree of Master of Science.

\_\_\_\_\_  
Assoc. Prof. Dr. Cumali Sabah  
Supervisor

**Examining Committee Members**

Assoc. Prof. Dr. Cumali Sabah      Electrical and Electronics \_\_\_\_\_  
Engineering Dept.  
METU NCC

Assoc. Prof. Dr. Murat Fahriođlu      Electrical and Electronics \_\_\_\_\_  
Engineering Dept.  
METU NCC

Assoc. Prof. Dr. Huseyin Ademgil      Computer Engineering Dept. \_\_\_\_\_  
European University of Lefke

**I hereby declare that all information in this document has been obtained and presented in accordance with academic rules and ethical conduct. I also declare that, as required by these rules and conduct, I have fully cited and referenced all material and results that are not original to this work.**

Name, Last name: Batuhan Mulla

Signature :

## **ABSTRACT**

### **A MULTIBAND METAMATERIAL ABSORBER DESIGN FOR SOLAR CELL APPLICATIONS**

Mulla, Batuhan

M.Sc. Sustainable Environment and Energy Systems Program

Supervisor: Assoc. Prof. Dr. Cumali Sabah

Solar energy is one of the most abundant energy in nature. Harvesting this energy in a more efficient way can be realized by metamaterials. Metamaterials which are manmade artificial materials can provide great absorption characteristics as well as reduced material costs with their compact structures. In this thesis, unique metamaterial absorber designs for thermo-photovoltaic and for photovoltaic applications are proposed and numerically analyzed in terms of their absorption capacity, polarization and incident angle stability and thermal stability. Moreover, absorption enhancement techniques such as applying graphene or indium thin oxide layers are discussed and implemented to the absorber design.

Keywords: Metamaterial, perfect absorber, multi- band, solar cells.

## ÖZ

# GÜNEŞ PİLİ UYGULAMALARI İÇİN ÇOK-BANTLI METAMALZEME SOĞURUCUSU TASARIMI

Batuhan Mulla

Yüksek Lisans, Sürdürülebilir Çevre ve Enerji Sistemleri Programı

Tez Yöneticisi: Doç. Dr. Cumali Sabah

Güneş enerjisi doğada en fazla bulunan enerji türlerinden bir tanesidir. Bu enerjiyi daha verimli bir şekilde elde etme meta malzemeler aracılığıyla gerçekleştirilebilir. İnsan yapımı, yapay malzemeler olan meta malzemeler, çok yüksek seviyedeki emicilik kapasitelerinin yanında sıkıştırılmış yapıları nedeniyle kullanılan malzemenin fiyatında da düşüş sağlayabilme özelliğine sahiptirler. Bu tezde, fotovoltaiik ve termofotovoltaiik uygulamaları için özgün meta malzeme emici tasarımları sunulmuş ve numerik olarak, emicilik özellikleri, ışığın kutuplaşması ve geliş açısı kararlılıkları ile termal özellikleri açısından incelenmişlerdir. Ek olarak, graphene ve indiyum kalay oksit katmanları uygulamak gibi emicilik geliştirme teknikleri de incelenmiş ve uygulanmıştır.

Anahtar kelimeler: Meta malzeme, Mükemmel soğurucu, çok-bantlı, Güneş pili uygulamalar

## **DEDICATION**

I dedicate this work to my family, for all their support.

## ACKNOWLEDGEMENTS

Foremost, I would like thank to my thesis supervisor, Assoc. Prof. Dr. Cumali Sabah whose immense knowledge, understanding, and patience, considerably contributed to my graduate experience. His guidance always helped me during my research and for completing of this study.

Besides my supervisor, I also would like to thank to thesis jury members: Assoc. Prof. Dr. Murat Fahriođlu and Assoc. Prof. Dr. Hüseyin Ademgil for their valuable suggestions and constructive criticisms during this study.

I would like also to thank Assist. Prof. Dr. Furkan Dinçer for his help and suggestions. I must also acknowledge other colleagues in the metamaterial research group; Patrick Rufangura and Mehmet Paşa Üstünsoy for their constructive ideas during this study.

Last but not least, I would like to thank my family for their support, and encouragement during my research.

## TABLE OF CONTENTS

ETHICAL DECLARATION.....	iii
ABSTRACT.....	iv
ÖZ.....	v
DEDICATION.....	vi
ACKNOWLEDGEMENTS.....	vii
TABLE OF CONTENTS.....	viii
LIST OF FIGURES.....	xi
LIST OF TABLES.....	xvi
NOMENCLATURE.....	xvii
CHAPTER 1	
INTRODUCTION.....	1
1.1. Solar Energy .....	1
1.2. Maxwell’s Equations .....	3
1.3. Metamaterials .....	4
1.4. Metamaterials Absorber.....	6
1.4.1. Metamaterial Absorbers for Thermo-photovoltaics Applications.....	7
1.4.2. Metamaterial Absorbers for Photovoltaics Applications.....	8
CHAPTER 2	
DESING AND ANALYSIS OF METAMATERIAL ABSORBERS.....	9
2.1. Methodology for the Design.....	9
2.2. Analyzing Approach .....	11

## CHAPTER 3

PRIOR ART INVESTIGATION, PRELIMINARY DESIGN, AND VALIDATION.....	14
3.1. Introduction.....	14
3.2. Numerical Validation.....	14
3.2.1. Prior Art Investigation.....	14
3.2.2. Validation of FIT based numerical results with FEM based software.....	17
3.3. Theoretical Validation.....	19
3.3.1. Interference Theory.....	19
3.4. Conclusion.....	23

## CHAPTER 4

SINGLE AND DUAL BAND METAMATERIAL ABSORBERS.....	24
4.1. Introduction.....	24
4.2. Single-Band Metamaterial Absorber.....	24
4.2.1. Design and Simulation.....	24
4.2.2. Result and Discussion.....	25
4.3. Dual-Band Metamaterial Absorber.....	30
4.3.1. Design and Simulation.....	30
4.3.2. Result and Discussion.....	31
4.4. Conclusion.....	35

## CHAPTER 5

MULTIBAND METAMATERIAL ABSORBER TOPOLOGY.....	37
---	----

5.1.	Introduction.....	37
5.2.	Design and Simulation .....	38
5.3.	Results and Discussion.....	39
5.3.1.	Multiband Topology .....	40
5.3.2.	Geometrical Effects on the Absorption Response.....	45
5.4.	Conclusion.....	50

## CHAPTER 6

### MULTIBAND METAMATERIAL ABSORBER FOR THERMO-PHOVOLTAIC APPLICATIONS.....

51

6.1.	Introduction.....	51
6.2.	Design and Simulation.....	52
6.3.	Result and Discussion.....	54
6.4.	Theoretical Verification.....	61
6.5.	Conclusion.....	62

## CHAPTER 7

### MULTIBAND METAMATERIAL ABSORBER FOR PHOTOVOLTAIC APPLICATIONS.....

63

7.1.	Introduction.....	63
7.2.	Design and Simulation.....	63
7.3.	Results and Discussion.....	64
7.4.	Conclusion.....	71

## CHAPTER 8

### APPLICATIONS OF THE ABSORPTION ENHANCEMENT THECNQUES.....

72

8.1. Introduction.....	72
8.2. Hole at the Back Metallic Plate.....	72
8.3. Graphene.....	75
8.4. Indium Tin Oxide.....	78
8.5. Conclusion.....	82
CHAPTER 9	
CONCLUSION.....	83
9.1. Conclusion of the Thesis.....	83
9.2. Future Work.....	84
BIBLIOGRAPHY.....	85

## LIST OF FIGURES

Figure 1-1. Solar irradiance spectrum [6] .....	2
Figure 1-2. Electromagnetic properties of materials .....	5
Figure 2-1. Illustration of the different wave modes.....	11
Figure 3-1. (a) The geometric structure of the design of Hao et al. [61]. (b) The reflection and transmission results obtained by Hao et al. [61] by FDTD based solver.....	16
Figure 3-2. The reflection and transmission results obtained by redesigning and simulating the metamaterial absorber by FIT based software.....	16
Figure 3-3. The geometry of the unit cell of a metamaterial absorber design for the validation. The magnitude of the geometrical dimensions are provided next to the related part.....	18
Figure 3-4. Comparison between the FEM and FIT based solvers for the design given in Figure 3-3.....	19
Figure 3-5. Illustration of the unit cell of the models used for the theoretical validation (a) Coupled model, (b) Decoupled model.....	20
Figure 3-6. Illustration of the way of the rays and their coefficients.....	21
Figure 3-7. Obtained results from the simulation of the decoupled model. (a) S-parameters, (b) Phase of S- parameters.....	22
Figure 3-8. Comparison between results obtained by FEM and FIT based solvers with the theoretical result (red curve).....	23
Figure 4-1. (a)The geometric structure of design, (b) the unit cell of structure with dimensions (side view).....	25
Figure 4-2. (a) Dependence of absorption and resonance frequency on (a) dielectric thickness, (b) on the length of the strips.....	26

Figure 4-3. Reflection and absorption results obtained from the simulation. Geometric dimensions are: $d=135$ nm $w=20$ nm $a=12$ nm $h=20$ nm $x=420$ nm and $y=125$ nm.....	27
Figure 4-4. Real and imaginary part of the relative impedance.....	27
Figure 4-5. Simulation results for absorption under different polarization angle, $\Theta$ , at normal incidence.....	28
Figure 4-6. Absorption spectra for different incident angles (a) TE mode, (b) TM mode.....	27
Figure 4-7. Half power bandwidth of absorber.....	29
Figure 4-8. (a) Z-component of electric field distribution at 403.5 THz, (b) Surface current distribution of the structure at 403.5 THz.....	29
Figure 4-9. Unit cell geometry of the proposed metamaterial absorber.....	31
Figure 4-10. Reflection and absorption spectra. Geometric dimensions are: $d=60$ nm $w=20$ nm $a=b=50$ nm $h=50$ nm $p=455$ nm and $l=170$ nm and $g=40$ nm.....	32
Figure 4-11. Field distributions at resonance frequencies. (a) Electric field distribution at 654.9 THz, (b) Electric field distribution at 708.3 THz, (c) magnetic field distribution at 654.9 THz, (d) magnetic field distribution at 708.3 THz.....	33
Figure 4-12. Dependence of the absorption response on a) SiO <sub>2</sub> thickness, b) the gap between the strips, c) the width of the strips.....	35
Figure 4-13. Polarization spectra of the proposed absorber.....	35
Figure 5-1. Unit cell design of the proposed absorber.....	38
Figure 5-2. Absorption spectrum of the proposed absorber. $a=150$ nm, $b=135$ nm, $c=80$ nm, $d=65$ nm, $e=f=g=100$ nm, $h=50$ nm, $t=15$ nm and $p=980$ nm.....	40
Figure 5-3. Absorption spectra for different geometric structures of the design. (a) Without resonators, (b) only inner quadruple resonators are used, (c) only middle	

quadruple resonators are used, (d) only outer quadruple resonators are used, (e) combined structure.....	42
Figure 5-4. Electric field distributions of the structure at (a) 148.9 THz (b) 179.8 THz, (c) 213.1 THz, (d) 269.8 THz, (e) 287.2 THz.....	44
Figure 5-5. Magnetic field distributions of the structure at (a) 148.9 THz (b) 179.8 THz, (c) 213.1 THz, (d) 269.8 THz, (e) 287.2 THz.....	44
Figure 5-6. Surface current distributions of the structure at (a) 148.9 THz (b) 179.8 THz, (c) 213.1 THz, (d) 269.8 THz, (e) 287.2 THz.....	45
Figure 5-7. Variation of absorption spectra for a) outer resonator pairs (parameter a), b) middle resonator pairs (parameter b), c) inner resonator pairs (parameter c), d) when all the dimensions are varied (parameter N).....	47
Figure 5-8. Variation of absorption spectra for a) dielectric layer thickness (parameter d), b) period of the absorber (parameter p).....	48
Figure 5-9. Extracted effective parameters a) effective permittivity b) effective permeability.....	49
Figure 5-10. a) Absorption spectra for various polarization angles for TEM mode b) absorption spectra for various incident angles for TE mode c) absorption spectra for various incident angles for TM mode.....	50
Figure 6-1. Geometry of the unit cell of the proposed metamaterial absorber structure. a) Perspective view b) Front view.....	53
Figure 6-2. The reflectance and absorption spectra of the structure in the visible frequency region.....	55
Figure 6-3. The reflectance and absorption spectra of the structure a) in infrared frequency region b) in ultraviolet frequency region.....	55
Figure 6-4. The contribution of the resonators to the absorption spectrum. a) Represents the contribution of the patches at the corners and b) represents the contribution of the strips and the patch at the central of the structure. c) Comparison of the effects of the central patch on the absorption spectrum.....	56

Figure 6-5. (a1)- (c1) X-component of the electric field distributions. (a2)- (c2), Z-component of the electric field distributions. (a3)- (c3), Magnitude of the electric field distributions on the dielectric layer. (a4)- (c4) Y-component of the magnetic field distributions. (a5)- (c5) Surface current distributions. All the Figures are given for the first second and third resonances respectively. The scales of the corresponding distributions are given at the bottom of each group.....57

Figure 6-6. Variation of absorption spectra for a) dielectric layer thickness (parameter d), b) resonator thickness, (parameter e), c) strip length (parameter c), d) strip width (parameter t).....58

Figure 6-7. Normalized effective impedance of the absorber. The inner table shows the real and imaginary parts of the impedance at resonant frequencies.....60

Figure 6-8. The absorption spectra under for various polarization angles.....61

Figure 6-9. Comparison of the Theoretical and simulation results for absorption.....61

Figure 7-1. Proposed metamaterial absorber design.....64

Figure 7-2. Absorption and reflectance response of the proposed absorber. The values taken for the parameters are: a=250 nm, d=10 nm, h=50 nm, t=10 nm and p=590 nm.....65

Figure 7-3. Distributions at resonance frequencies. (a) electric field at 439.95 THz, (b)electric field at 508.35 THz, (c) magnetic field at 439.95 THz(d) magnetic field at 508.35 THz, (e)surface current at 439.95 THz (f) surface current at 508.35 THz. Electric and magnetic field distributions are given on x-y plane where surface current distributions are given on y-z plane at x=295 nm.....68

Figure 7-4. The dependence of the absorption spectra on the geometric variables. (a) Dependence on the unit cell period. (b) Dependence on the semiconductor height. (c) Dependence on the side length of the isosceles triangular resonators. The variation of the absorption spectra of amorphous silicon are represented in the inset of each of the figures..... 69

Figure 7-5. Dependence of the absorption on polarization angle under normal incidence mode of the electromagnetic radiation.....	70
Figure7-6. Absorption response under various incident angles (a) TE mode (b) TM mode.....	70
Figure7-7. Thermal characterization of the absorber between 0° C and 60° C.....	71
Figure 8-1. Illustration of the reshaped back silver plate. (a) Square shaped hole, (b) cross shaped hole, (c) triangular hole.....	73
Figure 8-2. The place and the geometric structure of the applied graphene. (a) First design, (b) Second design.....	76
Figure 8-3. Variation of the absorption spectra according to the number of graphene layer used.....	78
Figure 8-4. Illustration of the design after the usage of ITO layer. (a) Presence of ITO only the top of the design, (b) Simultaneously presence of ITO between the resonators and on the top of the design.....	80
Figure 8-5. Variation of the absorption spectra according to the depth of ITO layer when ITO was utilized only the top of the design (Figure 8-4a).....	81
Figure 8-6. Variation of the absorption spectra according to the depth of ITO layer when ITO was utilized both on the design and between the resonators (Figure 8-4b). .....	81

## LIST OF TABLES

Table 5-1. Geometric dimensions of the design.....	38
Table 6-1. Values associated with each parameter in nanometer.....	52
Table 7-1. Total absorption rates of a-Si over the whole spectrum for various geometric dimensions.....	68
Table 8-1. The absorption rates over whole spectrum for various square hole dimensions.....	74
Table 8-2. The absorption rates over whole spectrum for various strip lengths.....	74
Table 8-3. The absorption rates over whole spectrum for various side lengths of triangles.....	75
Table 8-4. The absorption rates over whole spectrum for various number of graphene layers. The rates are given for the fully graphene covered structure (Figure 8-2a).....	77
Table 8-5. The absorption rates over whole spectrum for various number of graphene layers. The rates are given for the partially graphene covered structure (Figure 8-2b).....	78
Table 8-6. The absorption rates over whole spectrum for various ITO layer thicknesses. The rates are given for the design presented in Figure 8-4a.....	82
Table 8-7. The absorption rates over whole spectrum for various ITO layer thicknesses. The rates are given for the design presented in Figure 8-4b.....	82

## NOMENCLATURE

<i>PV</i>	Photovoltaic
<i>MTM</i>	Metamaterials
<i>TPV</i>	Termo-Photovoltaic
$\mu$	Magnetic permeability
$\varepsilon$	Electric permittivity
<i>E</i>	Electric field (V.m <sup>-1</sup> )
<i>H</i>	Magnetic field (A.m <sup>-1</sup> )
$\omega$	Angular frequency (Hz)
<i>k</i>	Extinction coefficient
<i>c</i>	Speed of light (m s <sup>-1</sup> )
<i>THz</i>	Terahertz
<i>nm</i>	nanometer
<i>ITO</i>	Indium Tin Oxide
<i>TCO</i>	transparent conductive oxides
<i>e</i>	Charge of electron (1.60217657 × 10 <sup>-19</sup> C)
$\Gamma$	Damping Constant
$\omega_p$	Plasma frequency
$\varepsilon_0$	Permittivity free space ( 8.85 x 10 <sup>-12</sup> F/m )
<i>R</i> ( $\omega$ )	Frequency dependent reflection coefficient
<i>A</i> ( $\omega$ )	Frequency dependent absorption coefficient
<i>T</i> ( $\omega$ )	Frequency dependent transmission coefficient

$Z(\omega)$	Frequency dependent impedance
$MA$	Metamaterial absorber
$FWHM$	Full Width at Half Maximum
$TE$	Transverse Electric
$TM$	Transverse Magnetic
$TEM$	transverse electromagnetic
$FBW$	Frequency Bandwidth
$FIT$	Finite Integration Technique
$FEM$	Finite Element Method
$FDTD$	Finite Difference Time Domain
$\delta$	Skin depth (m)
$GaAs$	Gallium Arsenide
$UV$	Ultraviolet
$IR$	Infrared
$Al$	Aluminum
$Si$	Silicon
$SiO_2$	Silicon Dioxide
$\sigma$	Electric conductivity ( $s\ m^{-1}$ )
$\rho$	Electric resistivity
$h$	Plank's constant ( $6.62606957 \times 10^{-34} m^2 kg\ s^{-1}$ )
$k_B$	Boltzmann's constant ( $1.3806 \times 10^{-23} m^2 kg\ s^{-2} K^{-1}$ )
$Ag$	Silver



## CHAPTER 1

### INTRODUCTION

The energy requirements of human beings are increasing every day. This energy demand is mainly provided by fossil fuel-fired power plants, hydroelectric energy plants and nuclear fuel burning energy plants. Considering the 2014 BP Statistical Review of World Energy report, %87 of world electricity necessity is provided by fossil fuels [1]. These sources lead to the adverse effects to the environment, to the atmosphere and also to the humanity when burned. Global temperature also effected from this condition. Enhancement of the mentioned greenhouse gases causes the increment of the temperature in globally [2]. Moreover, this enhancement can cause many unwanted side-effects on earth and human health. In addition to these, the instability of the prices of coal and oil is being another problem. As the main electricity supply are these sources, this circumstance can result with the increase in the price of electricity.

One solution for not employing the fossil fuels could be the usage of the nuclear sources. Nuclear power plants emit less greenhouse gases to the atmosphere with respect to fossil fuel-fired power plants. However it is an enemy of the environment. Lastly the in secureness of nuclear power was shown by Fukushima Daiichi accident in japan on March 2011 [3].

Hydro power is a clean source but it needs a huge amount of water to operate and should be located on the way of this huge amount of water. Providing the energy demand without releasing greenhouse gasses to the atmosphere can be realized by using renewable energy sources.

#### **1.1.Solar Energy**

One of the most popular and preferred energy source is the solar energy. This source can be used to supply clean energy by the utilization of the solar cells. There are different forms of the solar cells being photovoltaic (PV) thermo-photovoltaic (TPV) cells. Solar energy utilization performance of solar cells is limited due to the reason that they cannot completely convert all solar radiation in the solar spectrum [4-5].

Solar irradiance which is a wavelength depended quantity, is given in Figure 1-1 [6]. This spectrum covers the range between 100 THz to 1000 THz (100 nm to 1000 nm as wavelength). The solar spectrum consist three different frequency regions. These regions are: infrared region (100 THz to 400 THz) visible region (400 THz to 750 THz) and ultraviolet region (750 THz to 1000 THz). However, most of the energy is located between 400 THz and 750 THz as can be seen from Figure 1-1[7].

The performance of the solar cells can be further improved if the losses which cause the inefficiency of solar cell could be minimized. Some of these loses are being the optical loses and recombination loses. In addition to loses, the production and the fabrication cost of a unit cell of solar cells also have crucial role when the usage density of these cells are being considered. The developed fabrication techniques open the road for the lesser cost for the fabrication of unit cells. Material cost can be minimized by employing the materials among the suitable ones, according to their abundancy in the nature.

By considering the mentioned issues, metamaterials could have the critical role for eliminating loses [8]. In addition, with the developed fabrication techniques these devices can be produced as compact as possible so that they occupy smaller areas with improved efficiencies.

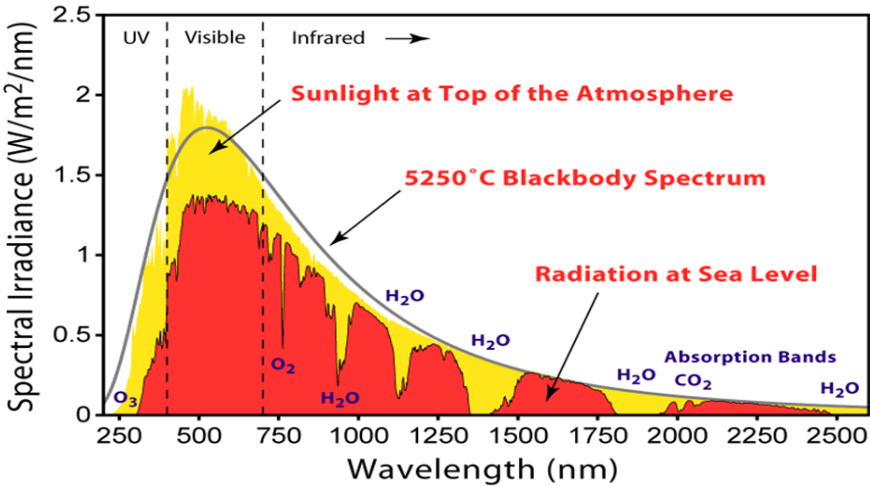


Figure 1-1. Solar irradiance spectrum [6].

## 1.2. Maxwell's Equations

The interaction of light radiation and matter can be well understood by studying Maxwell's equations in an isotropic medium. The differential form of the Maxwell equations are represented in relations (1.1)-(1.4).

$$\nabla \cdot \vec{D} = 0 \quad (1.1)$$

$$\nabla \cdot \vec{B} = 0 \quad (1.2)$$

$$\nabla \times \vec{E} = -\frac{\partial \vec{B}}{\partial t} \quad (1.3)$$

$$\nabla \times \vec{H} = \frac{\partial \vec{D}}{\partial t} \quad (1.4)$$

In equation (1.1),  $D$  represents the electric flux density in  $C/m^2$  while  $B$  in equation (1.2) symbolize the magnetic flux density.  $E$  and  $H$  are the electric field and magnetic field (A/m) respectively.

In homogeneous isotropic medium  $D$  and  $B$  can be given by equations (1.5) and (1.6).

$$\vec{D} = \epsilon \vec{E} \quad (1.5)$$

$$\vec{B} = \mu \vec{H} \quad (1.6)$$

Maxwell's equations in isotropic medium can be rewritten as shown in equations (1.7)-(1.10) when equations (1.5) and (1.6) are considered together.

$$\nabla \cdot \epsilon \vec{E} = 0 \quad (1.7)$$

$$\nabla \cdot \mu \vec{H} = 0 \quad (1.8)$$

$$\nabla \times \vec{E} = -\mu \frac{\partial \vec{H}}{\partial t} \quad (1.9)$$

$$\nabla \times \vec{H} = \epsilon \frac{\partial \vec{E}}{\partial t} \quad (1.10)$$

When the relations for the electric and magnetic fields (equations (1.11) and (1.12)) and Maxwell's equations are combined together equations (1.13) and (1.14)

$$\vec{E}(\omega, \vec{k}) = \vec{E}_0 e^{i(\vec{k}\vec{z} - \omega t)} \quad (1.11)$$

$$\vec{B} = \vec{B}_0 e^{i(\vec{k}\vec{z} - \omega t)} \quad (1.12)$$

$$\vec{k} \times \vec{E} = -\frac{\omega}{c} \mu \vec{H} \quad (1.13)$$

$$\vec{k} \times \vec{H} = \frac{\omega}{c} \varepsilon \vec{E} \quad (1.14)$$

Where wave vector, angular frequency of electromagnetic wave and speed of light in free space can be symbolize by  $\vec{k}$ ,  $\omega$ , and  $c$  correspondingly.

### 1.3. Metamaterials

In recent years, significant attentions have been attracted on the artificial materials (namely metamaterials) as they can dramatically manipulate the incident electromagnetic wave [9-10]. In addition to effects on the incident wave, they exhibits exotic properties (negative refractive index [11-14], invisibility cloaking [15] and so on) which are not possible to observe by natural materials.

The material properties are strongly dependent on their complex permittivity ( $\varepsilon$ ) and complex permeability ( $\mu$ ) values which are provided in equation 1.15 and equation 1.16 correspondingly [16].

$$\varepsilon(\omega) = \varepsilon'(\omega) + i\varepsilon''(\omega) \quad (1.15)$$

$$\mu(\omega) = \mu'(\omega) + i\mu''(\omega) \quad (1.16)$$

These values are frequency dependent values. This means that the response is changing with the frequency. In general, the properties of the materials according to their electromagnetic characteristics are represented in Figure 1-2. The materials that have positive permeability and negative permittivity is the metals at optical frequencies and the plasmas while the dielectrics have both positive values of these quantities. The magnetic materials have permeability lesser than zero and electric permittivity greater

that zero. These three types explained above are called right handed materials and they be found in the nature. However, the ones that have both of the permittivity and the permeability negative cannot be found in the nature [17-18].

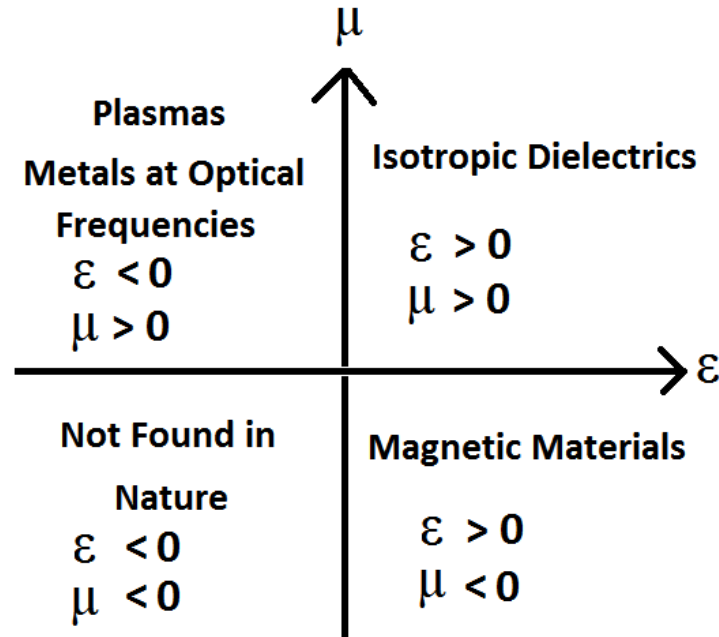


Figure 1-2. Electromagnetic properties of materials.

Optical response of a material can be discovered by its refraction index shown with the equation 1.17. In this relation,  $n$  is the real part while  $k$  is the imaginary part of the index. Metamaterials show native values for this relation which cannot be come across with the natural materials.

$$\tilde{n} = n + ik \quad (1.17)$$

Metamaterials dimensions should be the smaller than the wavelength of interest wavelength especially in the lateral directions. The material composition of the metamaterials are various. They are usually composed of different layers with various materials. Because of this, they are inhomogeneity in the appearance. However, as they are smaller than the wavelength, the incoming radiation point of view, they are homogeneous. This makes them to behave as one material while being the combination of various materials.

By the help of the improved fabrication techniques, the compact metamaterials can be produced. This results with the lesser space requirement and thus the reduced material cost. The strong ability of these materials to manipulate the light makes them the possible future for the solar energy sector.

After the first metamaterial absorber proposed and experimental demonstrated by Landy *et al* [19], there has been many researches made for single band [20] wide band [21-23] multi band [24-26] metamaterial absorbers for different frequency realms such as microwave [22] terahertz [23] optical [24-25] for variety of applications.

Due to these extraordinary properties mentioned above, there are many potential application areas of metamaterial such as; sensors [27-28], switches [29], absorbers [30] among these application areas, perfect absorption is crucial for applications like micro-bolometers, sensors, thermal imagers, and solar energy utilization.

#### **1.4. Metamaterials as Absorbers**

One of the most critical applications of these structures is the perfect absorption. Perfect absorption can be obtained when the transitivity and the reflectivity of these materials are simultaneously reduced to zero so that all the incident electromagnetic radiation is absorbed by the material [31-33]. Although metamaterial absorber compose of different layers, they behave as an effective material as they are subwavelength structures with respect to the incident wave [34-36]. Therefore, effective parameters, which are permittivity and permeability, specify the properties of the metamaterial absorbers. Especially, these parameters can be arranged so that the effective impedance of the absorber becomes same with the impedance of the free space [37-39]. Under these circumstances, the reflected and transmitted waves minimized simultaneously and the perfect absorption is achieved [40]. The relation for impedance can be calculated via equation 1.18. The resonant response of the metamaterial absorbers are strongly dependent on to the geometric dimensions of the structure. By varying these dimensions, the electrical and optical responses of metamaterial absorbers can easily be tuned. If the geometrical dimensions of a

metamaterial absorber are properly adjusted the match of the impedances might be realized.

$$(z(w) = \sqrt{\mu(w)/\varepsilon(w)} ). \quad (1.18)$$

In addition, plasmon polaritons at higher frequencies can create the plasmonic resonances so that the incident wave is totally absorbed [41-43].

#### **1.4.1. Metamaterial Absorbers for Thermo-Photovoltaics Applications**

Heat or thermal energy can be converted into usable forms of energy (mainly electricity) by the utilization of thermo-photovoltaics. If the appropriate material combinations (which causes the heat generation) are selected and the metamaterial absorber has a good absorption rate in the solar range, then, this absorber can be used for the very efficient utilization of the solar energy. Thus, some of the energy requirements of the human beings supplied by sun as a renewable and sustainable sources can be increased with this original arrangements.

TPV's are the combination of an absorber/emitter, a photodiode, and an external heat source. [44-45]. Working mechanism of thermo-photovoltaics start with the absorption and re-emission of the energy coming from the heat source. Re-emitted radiation can be used by the photovoltaic cells to convert solar or heat energy into the electricity. Therefore, the absorption property of the metamaterial absorber can be used to capture the solar radiation by the integration of such absorbers into the photovoltaic and/or thermo-photovoltaic systems. In this sense, a metamaterial absorber can be used to improve the miniaturization and the efficiency of thermo-photovoltaics or photovoltaics.

Although solar energy covers three frequency region, (visible infrared and ultraviolet) most of the previous studies focused on only one frequency region. For example Ayas *et al.* [46] worked on a metamaterial absorber structure which was designed to work in visible frequency range. Their design has three bands in this range. Liu *et al.* [47] designed an aluminum based metamaterial absorber. Their absorber designed to operate in the ultraviolet frequency range. Moreover generally, in the literature,

multilayered absorber designs are employed in order to absorb solar energy. Using a multilayer design can enhance the absorption rate. On the other hand it increases the necessary material cost and the complexity of the absorber structure. Liang *et al* [48] presented a metamaterial solar energy absorber which has a pyramidal shape. They utilized vertically cascaded metal-dielectric layers in order to obtain perfect absorption in the solar range. Moreover, Wu *et al.* [49] investigated the absorption effects in grating-based devices. Their structure is designed to operate in infrared frequencies. They also utilized vertically cascaded metal-dielectric grating for obtaining multiband absorption.

#### **1.4.2. Metamaterial Absorbers for Photovoltaics Applications**

The perfectly absorptivity property of the metamaterials can be utilized in the photovoltaic cell to convert the solar energy directly into the electric energy. For photovoltaic response, generally an active material is needed to absorb and convert the absorbed energy into the useful forms [50]. Active material is a semiconducting material where the light energy are transformed into electron hole pairs [51]. These pairs are then separated to the electrodes and finally the energy can be taken as the form of electric current from these electrodes [52].

The losses occurred within or out of the solar cell, reduce their performance and cause the inefficiently converting the solar energy into the usable forms [53]. These losses includes the energy lost in the metallic parts. This condition leads to the generation of heat which is a side effect for photovoltaic application [54].

Another disadvantage could be the thickness of the active material. As the depth of this beneficial material increases, the previously created electron hole pairs might recombined together [55]. This result with an inefficient working. As the metamaterials are compact structures and they are small in dimension, they can help the prevention of these loses occurred within the cell. Moreover, the plasmonics responses discussed above, can cause the creation of the new resonance and therefore the absorption behaviors.

The main objective of this thesis is the employment of the metamaterials for the utilization of the solar energy as a renewable source.

## CHAPTER 2

### DESIGN AND ANALYSIS OF METAMATERIAL ABSORBERS

Designing a perfect absorber which shows the metamaterial characteristics (double negativity), requires some specification with respect to the dimensions. The usage area of the designed absorber is also an important issue while determining frequency ranges for analysis and choosing the right materials to be used in the design. In addition to these, numerical modelling and analyzing of the metamaterials should be done in a correct manner in order to make sure the accuracy and the reality of the obtained results. Therefore, in this chapter, the approaches that have been used in this thesis for designing, analyzing, and characterizing the metamaterial absorbers are briefly explained.

#### 2.1. Methodology for the Design

The first step is designing the absorber. One of the most important issue while designing is to choose of the right material for efficiently absorbing and utilizing the solar radiation. Each particular applications of solar energy harvesting requires some specific properties. Therefore, the key material varies from one application area to another. Among the suitable materials for the desired application, the ones that are abundant in nature, have no side effects to the humanity and the environment have the usage priority in this thesis. In addition to these, the cost is another deterministic issue. Throughout the thesis, the materials that assure the above conditions and have the minimal cost are chosen, as long as they provide the optimum material requirements. The reason of choice of the materials for each individual design will also be explained in the related chapters of the thesis.

In this study, the analysis and the characterization of the designed absorbers have been carried on through the numerical simulation method. Thus, after determining the suitable material, selected materials are needed to be introduced to the simulation software. The electromagnetic and optical properties of the materials rely on frequency; especially for higher frequencies [56]. Therefore, frequency dependent constants which can be permittivity (both real and imaginary), conductivity, and refractive index are defined by using the empirical data in the frequency range of

interest. If the empirical data sets will be used, the number of measurements and the measurement intervals for frequencies are important for the reliable results. For some of the materials, the sufficient number of data are not given in the literature. For these materials some dispersion models like Drude Model, Drude-Lorentz [57-59] model or some dispersion formulas like Kubo formula [60] are also employed in order to introduce the material to the software effectively. The detailed information about the sources of the empirical data and/or the dispersion model used for modelling and introducing the materials are provided for every individual design in the related sections.

After the selection of the right material and introducing it to the simulation software, the geometrical dimensions of the model is needed to be determined. The lateral directions of the metamaterial absorber has to be smaller than the wavelength of the incident radiation [34-61, 62]. Therefore, when determining the geometric dimensions of the design, the attention have been paid on this essential rule. Moreover, minimizing the geometric dimensions also reduces the amount of material to be used in the unit cell. Hence, as the required material amount decreases, the material cost also decreases. However, due to the studied lengths for dimensions are in nanometer scale, it is not practical for the real applications to design the structure as small as possible. In addition, the complex geometric structures and smaller geometric scales increase the necessary fabrication costs. Because of the mentioned issues, throughout this work, these considerations are taken into account.

In addition, as explained before, the geometrical dimensions of the metamaterial absorber have a very critical role in determining the absorption characteristics [9, 19, and 34]. Perfect absorption takes place when the effective impedance of the absorber,  $z(w)$ , matches with the impedance of the free space [37-39]. This condition ensures the zero reflection and transmission of the incident wave.  $z(w)$  is strongly related with the effective permeability,  $\mu(w)$ , and effective permittivity,  $\varepsilon(w)$ , of the absorber ( $z(w) = \sqrt{\mu(w)/\varepsilon(w)}$ ). Effective permittivity and permeability are highly dependent on the geometric dimensions of the metamaterial absorber. Thus, impedance matching (so that perfect absorption) occurs when the electric and magnetic resonances exist

simultaneously. Therefore the dimensions of the structure should be determined very sensitively.

Although the single and narrow band Metamaterial absorbers in the literature are generally composed of three layers [5, 28, 37], for multiband and wide band absorption, metamaterial absorber designs are generally composed of more than three layers [63, 64, 72]. However, designing the absorber by using only three effective layers reduce the necessary material amount and also reduce the fabrication costs in terms of the practical applications. Therefore, in this thesis the idea of having multiband and wide band absorption response by utilizing the combination of three effective layers has been adopted.

In general, the mentioned three layers are made up of two metallic layers and a dielectric plate sandwiched between these metallic plates. For the basement metallic plate, the known terminology “skin depth” has been used to determine the thickness [65-66]. If the thickness of the basement metallic plane is greater than the skin depth of that material at the interested frequency ranges, then it acts like an optical mirror and prevents the transmissions that pass through the structure. Under this circumstances, transmission becomes negligible (approximately zero) [67]. In this thesis, the thickness of the bottom plates are designed to be greater than the skin depth of that material under the studied frequency intervals so that it does not transmit any radiation through.

## **2.2. Analyzing Approach**

In this thesis, the modelling and the characterization of the designed structure is carried out by finite integration technique based computer simulation software. The frequency dependent absorption response of the designed structure is analyzed by the frequency domain solver of this simulation software. The more detailed information about finite integration technique will be given in chapter 3.

All of the metamaterial absorber designs in this thesis is for solar cell applications. Therefore, the frequency range is chosen as the solar frequency range (100 THz 1000 THz). The whole material selections, dimensions, material properties, absorption

responses are analyzed under this regime. However, solar range is a very wide frequency range and different portions serves different properties. Due to this reason, for some of the designs, this wide frequency regime is divided into sub ranges (being infrared, visible and ultraviolet) and the proposed structures are analyzed separately.

Appropriate boundary conditions for the simulations are used for each of the design. In general, boundary conditions for the simulations are chosen to be periodic in  $x$  and  $y$ -directions and open boundaries are used along  $z$ -direction (lateral direction).

Periodic boundary conditions replicates primary unit cell (designed unit cell) in  $x$  and  $y$ -directions. This forms an endless lattice which consist of virtual unit cells along these directions. Therefore not only the response coming from the primary unit cell are displayed, but also the interactions between the primary cell with the adjacent virtual cells are also considered [68]. As only the unit cell of the metamaterial absorbers are designed in this thesis, this boundary condition is appropriate to virtualize the electrical and optical properties of the unit cell for a complete system [69].

The Propagation direction of the incident electromagnetic radiation is assumed to be in the  $z$ -direction for all of the simulations in this thesis. Unless it is stated, the modes of the polarization of the incident wave is assumed to be transverse electromagnetic mode (TEM). However, the polarization of the light can be in the other modes which are transvers electric (TE) and transvers magnetic (TM) modes [70]. Therefore, these modes are also analyzed for the designs. The differences between these modes is illustrated in Figure 2-1. Here, “E” is the electric field component while “B” and “k” represent the magnetic field and the propagation direction of the incident wave.

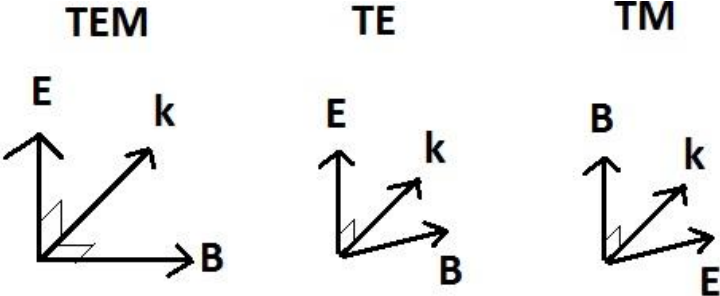


Figure 2-1. Illustration of the different wave modes.

Meshing is another important issue which plays a very important role while solving the electromagnetic problem. The simulation software divides the designed structure into the small elements which are called mesh. The accuracy of the obtained results are directly related with mesh type and the used mesh density. If the defined mesh density is not enough to solve electromagnetic problem, in this case the results become inconsistent or incorrect [71].

Through the thesis, physics controlled tetrahedral and hexahedral mesh with the adaptive mesh refreshment are used. Adaptive mesh refreshment ensures the sufficient mesh density generation for the accurate and reliable results. It increases the number of generated mesh cells and simulates the structure in each time, until the difference between the simulation results become smaller than the defined accuracy level. The accuracy for the adaptive the mesh density generation is set to be  $1 \times 10^{-6}$  accuracy level.

The output of the simulation software is the scattering parameters (S – parameters). By using the obtained scattering parameters, transmission and reflection coefficients can be obtained. In general, optical absorption behavior of a structure can be calculated by using Equation (2.1) where the frequency dependent parameters  $A(\omega)$ ,  $R(\omega)$ , and  $T(\omega)$  represent the absorption reflectance and transmittance, in order. As it is mentioned before,  $T(\omega)$  can be neglected because of the optical preventative characteristics of the bottom Al plate. Therefore, Equation (2.1) reduces to Equation (2.2). Using the obtained scattering parameters ( $S_{11}$  and  $S_{21}$ ) from the simulations, the absorption can be calculated via Equation (2.3) [72-74].

$$A(\omega) = 1 - |R(\omega)| - |T(\omega)| \quad (2.1)$$

$$A(\omega) = 1 - |R(\omega)| \quad (2.2)$$

$$A(\omega) = 1 - |S_{11}|^2 \quad (2.3)$$

## **CHAPTER 3**

### **PRIOR ART INVESTIGATION, PRELIMINARY DESIGN, AND VALIDATION**

#### **3.1. Introduction**

Validating the obtained results is a very essential step in order to ensure the reliability of the results. Thus, in this chapter the accuracy of the results are proved by a prior art investigation and a preliminary design. In order to do the mentioned analysis, two different types of methods are employed. These methods are numerical validation methods and theoretical validation method. Numerical validation include both verifying by using a previously reported metamaterial absorber from literature, and also the verification of the mainly used simulation software by another simulation method via a preliminary design. The second validating approach is the theoretical verification which is carried out by employing the interference theory.

In this chapter, as well as the validation analysis both for numerical and theoretical methods which show the reliability and the accuracy of the obtained results are carried out, the introductions of the numerical methods are also provided.

#### **3.2. Numerical Validation**

Throughout this thesis, finite integration method based software is the mainly employed computer software for numerical simulations. For the verification of the numerical simulation software, two types of method are performed. One of these methods is the validating the accuracy by a previously reported metamaterial absorber while the other is verifying the mainly used software by different numerical method based software.

##### **3.2.1. Prior Art Investigation**

In order to validate results, firstly a previously reported design in the literature is chosen. While determining the proper metamaterial absorber model in the literature for verifying the results, some important steps are considered. It is important to validate the results with the same range of the operation frequencies. Therefore, the

selected design from the literature, has to be operate within the higher frequencies. The metamaterial absorber design of Hao *et al.* [75] is selected for verification as it provides the desired properties.

Hao *et al.* [74]. Have studied on a metamaterial absorber which operates in the visible frequency ranges. Their proposed absorber is made up of three layers which is given in Figure 3-1a. The topmost layer of their design is a silver (Ag) patch, while the bottommost layer is composed of a continuous Ag plate. Between these plates a dielectric plate is employed as the separation layer between the two Ag layers. The dielectric material that they preferred to use is alumina ( $\text{Al}_2\text{O}_3$ ). For alumina, the optical refractive index has been taken as 1.75 while the permittivity of Ag has been described by employing Drude model. Drude model have been utilized as it consist the sufficient information for the introduction for the optical properties of Ag at the operation wavelengths. The parameters that they have used for Drude model are given as  $\omega_p = 1.37 \times 10^{16} \text{ s}^{-1}$  for plasma frequency and  $\gamma = 8.5 \times 10^{13} \text{ s}^{-1}$  for the collision frequency. They have assumed that all of the materials are not magnetic. They performed numbers of numerical simulations to optimize the geometric dimensions of the structure. They have used the finite-difference-time-domain (FDTD) based simulation software for numerical simulations. After optimization, the optimized parameters for their structures have been found as:  $W_x = W_y = 50 \text{ nm}$ ,  $t = 30 \text{ nm}$ ,  $d = 12 \text{ nm}$ ,  $h = 80 \text{ nm}$ , and  $a = 250 \text{ nm}$ . In order to discover features and the mechanism of their proposed metamaterial absorber, they have use the known relation of  $A = I - R - T$ . The results that they have obtained are given in Figure 3-1b. According to their results, their absorber provides a single band absorption at the wavelength of 596 nm with the absorptivity of 99.9%.

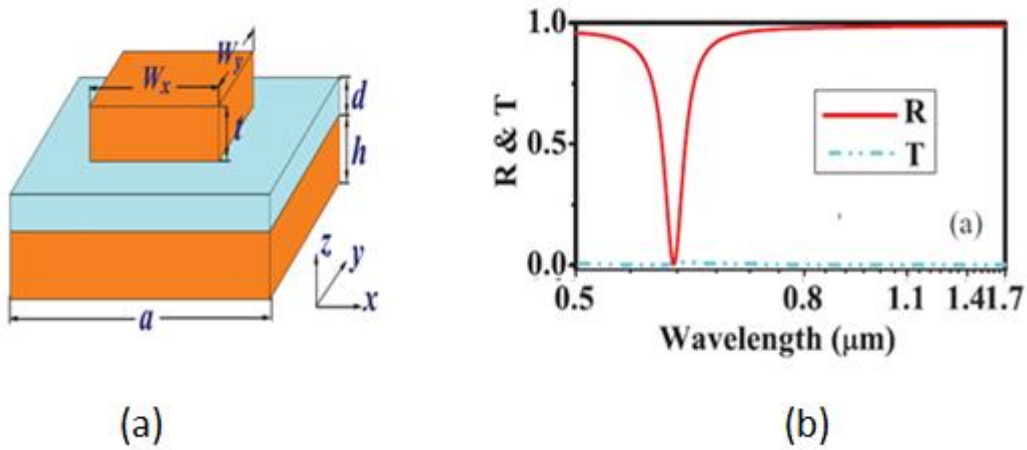


Figure 3-1. (a) The geometric structure of the design of Hao *et al.* [75], (b) the reflection and transmission results obtained by Hao *et al.* [75] by FDTD based solver.

The design of Hao *et al.* presented in Figure 3-1a is remodeled and simulated by using finite integrating technique (FIT) based software. The obtained results for reflection and transmission coefficients are provided in Figure 3-2. They mentioned that their design produce the absorption response at 596 nm with the rate of 99.9%. The redesigned and reanalyzed results indicate that the peak response is obtained at 600 nm with the absorptivity of 99.3%. The closeness of the obtained results indicate that the verification is realized.

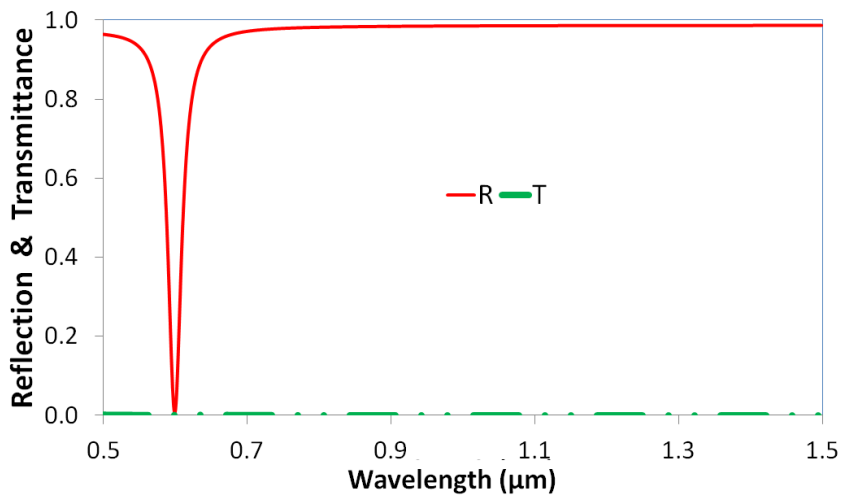


Figure 3-2. The reflection and transmission results obtained by redesigning and simulating the metamaterial absorber by FIT based software.

### **3.2.2. Validation of FIT Based Numerical Results with FEM Based Software**

There are lots of computer modeling software which use different solver methods. Here, the basic three of them will be introduced.

One of the powerful numerical analyzing methods is the finite element method (FEM). This method uses the differential form of the well-known Maxwell's equations to find the solution for the electromagnetic study. The solver works in a way that it separates the space into smaller parts called elements and analyses the problem over these subdivided elements [76]. The main advantages of using this method based software is that; it is flexible in the sense of designing the geometrical model. However the negative sides of the solver could be the necessity of high computational performance and therefore the necessity for the longer times for solution.

Another known numerical modeling method is the finite difference time domain method (FDTD). This method, which firstly introduced by Yee [77], performs the solution for the differential forms of the Maxwell equations like FEM based solver [78]. This solver is independent from the iterative solvers while it permits the parallel computation. This is an important property for the improved accuracy of the complex models. The main disadvantage of the solver is that; it needs the gridding of all the area for analysis. Due to this reason it requires very long time for analyzing. Thus, it is not preferred to be used for the smaller structures compared to wavelength.

In 1977 a new simulation method has been introduced by Weiland [76]. This method is being known as Finite Integration Technique (FIT) which utilizes the integral form of Maxwell equations. Moreover, it also uses the complete vector elements of electrical and magnetically strength [76]. This method enables the electromagnetic modeling and analysis of complex models. Both the time and frequency domains can be used within this solver. One of the benefit of FIT is the possible usage of the Cartesian and non-orthogonal grids. Another benefit of using this software is that; it requires lesser memory and lesser mesh for a complex structure when compared to the other solvers [79].

Among these methods, FIT base solver has been preferred and has been employed throughout the thesis. However, as previously discussed, validating the obtained results from many point of view are very crucial. Therefore, in addition to the

validation from literature, the obtained results are also analyzed by using the FEM based software. FEM based software is preferred instead of FDTD because, in the previous section Hao *et al.* utilized the FDTD based software for their design. As that result was validated with the FIT based software, in this part, only FEM is remained unused. Therefore, it has been preferred to be use in this section.

In order to compare the results obtained from FIT and FEM based solvers, a metamaterial absorber design presented in Figure 3-3 has been used. The yellow parts in Figure 3-3 are aluminum while silicon (Si) is preferred between the metallic parts in the design. The geometrical dimensions used for the modelling are also provided next to the related parts in Figure 3-3. The absorption and reflection responses obtained by simulating this structure in FEM and FIT based software is shown in Figure 3-4. The mentioned model gives a dual band absorption response at 160.3 THz and 355 THz with the magnitudes of 99.9% and 93.8% when FIT was used. The same resonances are provided at 160 THz and 358 THz with the absorptivity of 99.1% and 94.9% and 99.1% correspondingly by FEM based software. Both of the methods give the similar responses with a smaller shift in the frequency especially for the second resonance. Under this circumstances, these results ensure the verification of the software due to the similarities in the absorption characteristics and the closeness of the results at the peak points.

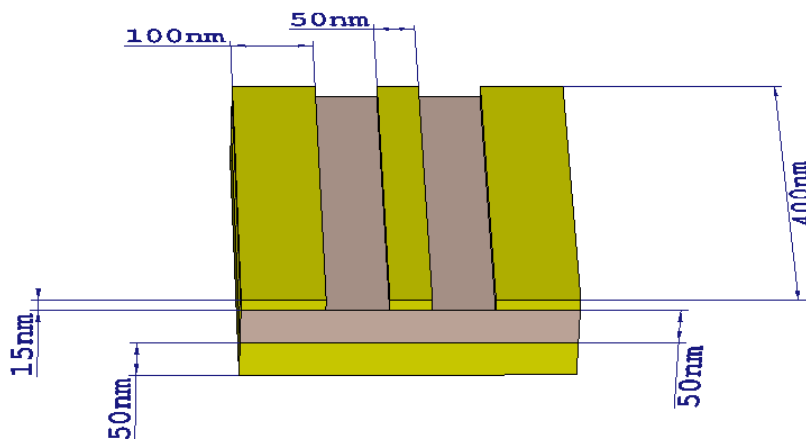


Figure 3-3. The geometry of the unit cell of a metamaterial absorber design for the validation. The magnitude of the geometrical dimensions are provided next to the related part.

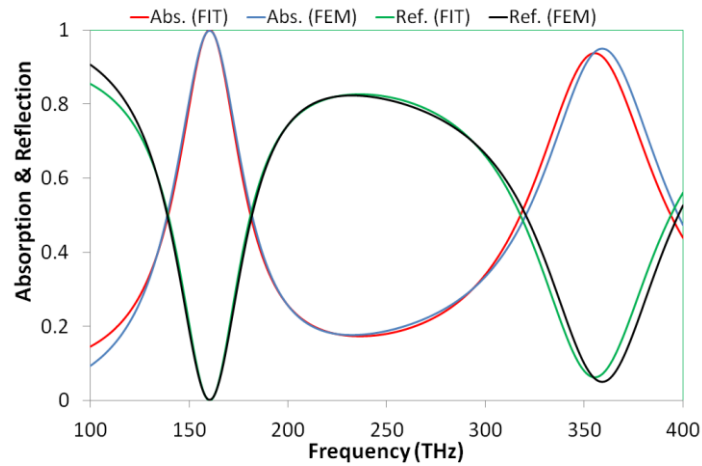


Figure 3-4. Comparison between the FEM and FIT based solvers for the design given in Figure 3-3.

### 3.3. Theoretical Validation

In addition to the validation with various simulation packages, in this section the verification is also carried out by using the theory. The well-known interference theory, which is given in the next section, have been employed for the theoretical investigation.

#### 3.2.1. Interference Theory

In this part, verification of the numerical result for the design given in the previous section is done by using interference theory model [80]. In the previous section the design used for the simulation was composed of three layers in which the basement layer is made up of a metallic film. The thickness of this metallic sheet had been arranged so that it does not let the rays to pass through the model. If a metamaterial model is arranged in a way that it has a thick metal sheet (generally thickness being greater than the skin depth) as the basement layer, in this case it has been named as “coupled model”. Coupled models have been used for the numerical simulations. The interference theory that is employed for the theoretical verification, requires the omission of the basement metal layer. In this case the model is called “decoupled model” [81]. The coupled and decoupled models are illustrated in Figure 3-5a and Figure 3-5b in order.

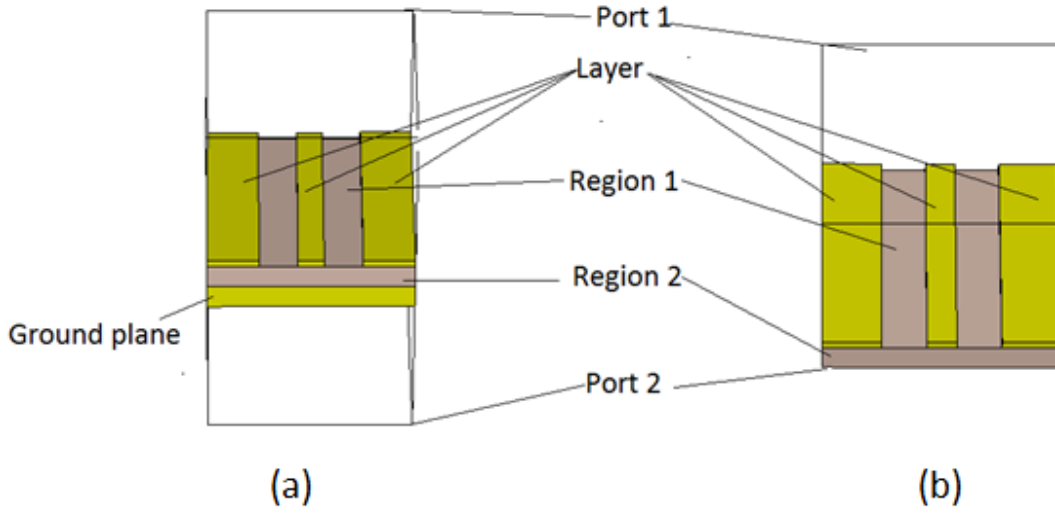


Figure 3-5. Illustration of the unit cell of the models used for the theoretical validation (a) Coupled model, (b) Decoupled model.

There are three possible conclusion when a wave meets with a surface. The first condition is the reflection of the incoming radiation back by region 1 as represented in Figure 3-6. The non-reflected portion of the received rays may transmitted from the Region 1 to Region 2 while the others are absorbed. The coefficients of layer 1 are :  $S_{11}=|s_{11}|e^{j\theta_{11}}$  ,  $S_{21}=|s_{21}|e^{j\theta_{21}}$  ,  $S_{12}=|s_{12}|e^{j\theta_{12}}$  and  $S_{22}=|s_{22}|e^{j\theta_{22}}$  Here,  $S_{11}$  gives the reflection coefficient from region 1 to region 1,  $S_{21}$  represents transmission coefficient from region 1 to region 2,  $S_{12}$  represents transmission coefficient from region 1 to region 2 and  $S_{22}$  represents the reflection coefficient from region 2 to region 2. According to these coefficients, the extended interference model, which calculates the total  $S_{11}$  parameter, can be represented by Equation (3-1) [82-83].

$$\begin{aligned} \sum S_{11} = & S_{11} + S_{12}e^{-j(2\beta+\pi)}S_{21} + S_{12}e^{-j(2\beta+\pi)}(S_{22}e^{-j(2\beta+\pi)})S_{21} + \\ & S_{12}e^{-j(2\beta+\pi)}(S_{22}e^{-j(2\beta+\pi)})^2S_{21} + S_{12}e^{-j(2\beta+\pi)}(S_{22}e^{-j(2\beta+\pi)})^3S_{21} + \\ & S_{12}e^{-j(2\beta+\pi)}(S_{22}e^{-j(2\beta+\pi)})^4S_{21} + \dots + S_{12}e^{-j(2\beta+\pi)}(S_{22}e^{-j(2\beta+\pi)})^nS_{21} \end{aligned} \quad (3.1)$$

Here  $\beta$  is the complex propagation phase.  $\beta=kd$  where  $k$  and  $d$  represents the wavenumber in region 2 and the propagation distance of the transmitting wave from layer 1 respectively.

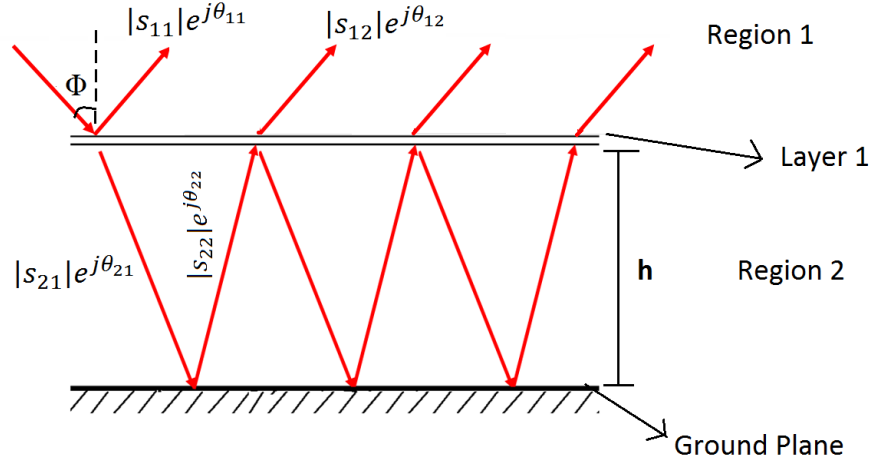


Figure 3-6. Illustration of the way of the rays and their coefficients.

If the Equation 3.1 is simplified, Equation 3.2 can be obtained and if it is arranged according to the superposition rule, the total reflection coefficient ( $S_{11}$ ) from region 1 to the region 1 can be obtained by using Equation (3.3)

$$\Sigma S_{11} = S_{11} + S_{12}e^{-j(2\beta+\pi)} (\Sigma_{n=0}^{\infty} (S_{22}e^{-j(2\beta+\pi)})^n) S_{21} \quad (3.2)$$

$$S_{11total} = S_{11} + \frac{S_{12}S_{21}e^{-j(2\beta+\pi)}}{1-S_{22}e^{-j(2\beta+\pi)}} \quad (3.3)$$

By bringing the S-parameters and their phases represented in Figure 3-7b, Equation (3.3) turns into Equation (3.4)

$$\Sigma S_{11} = |S_{11}|e^{j\theta_{11}} + \frac{|S_{12}||S_{21}|e^{-j(2\beta+\pi-\theta_{12}-\theta_{21})}}{1-|S_{22}|e^{-j(2\beta+\pi-\theta_{22})}} \quad (3.4)$$

Here in Equation (3.5), the magnitude of  $S_{21}$  could be considered as same with the magnitude of  $S_{12}$  due to the obtaining same results in the absorber model similar to

this. In this case, Equation (3.4) reduces to Equation (3.5) which can be used for the theoretical analysis.

$$\sum S_{11} = |S_{11}|e^{\theta_{11}} + \frac{|S_{12}|e^{-j(2\beta+\pi-2\theta_{12})}}{1-|S_{22}|e^{-j(2\beta+\pi-\theta_{22})}} \quad (3.5)$$

In order to apply the interference theory explained above, the ground layer of the model introduced in the previous section has been taken out. Under this circumstances, the newly obtained model is called the decoupled model and it is presented in Figure 3-5b. This model is then simulated by the FIT based software. The results for the magnitude of S-parameters and the phase of these parameters provided by the model are given in Figure 3-7a and Figure 3-7b correspondingly. These results are then used to find the total S-parameters of the combined structure via Equation (3.5). The output of Equation (3.5) are compared with the results obtained from the numerical validation section. The obtained results are provided in Figure 3-8. Similar absorption responses with almost same absorptivity levels are obtained when compared with the only simulation based results. It can be said that the results are theoretically verified.

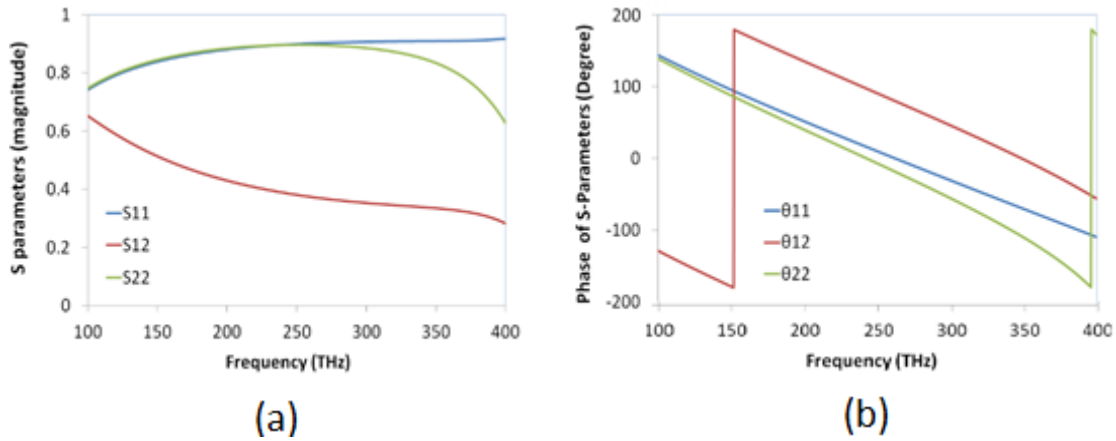


Figure 3-7. Obtained results from the simulation of the decoupled model. (a) S-parameters, (b) Phase of S-parameters.

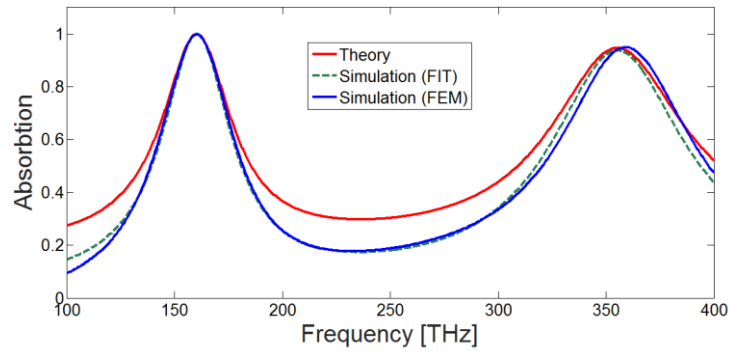


Figure 3-8. Comparison between results obtained by FEM and FIT based solvers with the theoretical result (red curve).

### 3.4. Conclusion

The numerical and the theoretical verification techniques are introduced in this chapter. In addition, the validation of the software is provided by both validating the previously reported design in the literature and by using the different solution methods. The mainly used solver method FIT in this thesis, is verified by FEM method based software. Moreover, both of the obtained numerical results are compared with the response of the interference theory. The results indicate the reliability and the accuracy of the results and the simulations used throughout the thesis.

## CHAPTER 4

### SINGLE AND DUAL BAND METAMATERIAL ABSORBERS

#### 4.1. Introduction

In the first chapter, the properties of the metamaterials and their ability of perfectly absorbing solar radiation is discussed. Afterwards, the designing and analyzing methodology and the validation technics are discussed. This chapter briefly introduces two different metamaterial absorber designs which have the potential to be used for utilizing the solar light striking on earth. Here, two applications of metamaterial absorbers for solar energy harvesting are presented in different sections. Section 4.2 demonstrates a design for the photovoltaic applications while section 4.3 is designed for the thermo-photovoltaic applications. The mentioned absorber models demonstrated here, exhibit the metamaterial double negative characteristics and polarization independent properties in the different portions of the visible light region.

#### 4.2. Single-Band Perfect Metamaterial Absorber

This section introduces a single band absorber model which utilizes the metallic strips for the generation of the surface plasmon polaritons. The proposed single band absorber is design is suitable to be used for the photovoltaic applications. According to the results this absorber gives perfect absorption in the visible range and it is also polarization independent. In addition, the fractional bandwidth (FBW) of the absorption region is calculated and 22.2% FBW is obtained which a promising result for a single band absorber.

##### 4.2.1. Design and Simulation

The geometric illustration of a single unit cell of proposed metamaterial absorber is presented in Figure 4-1a. The structure consists of aluminum plate at the bottom which prevents the transmission through the structure. Gallium arsenide (GaAs) plate is placed on the top of the aluminum plate as the dielectric material. In order to prevent the reflection, two aluminum strips are put on to the GaAs plate. The Drude model approximation is used for aluminum to calculate its electrical properties where the

collision frequency is calculated to be  $f_c=1074$  THz and plasma frequency  $f_p= 3812$  THz [83]. The optical properties of GaAs for visible and near infrared frequency ranges can be found in [84].

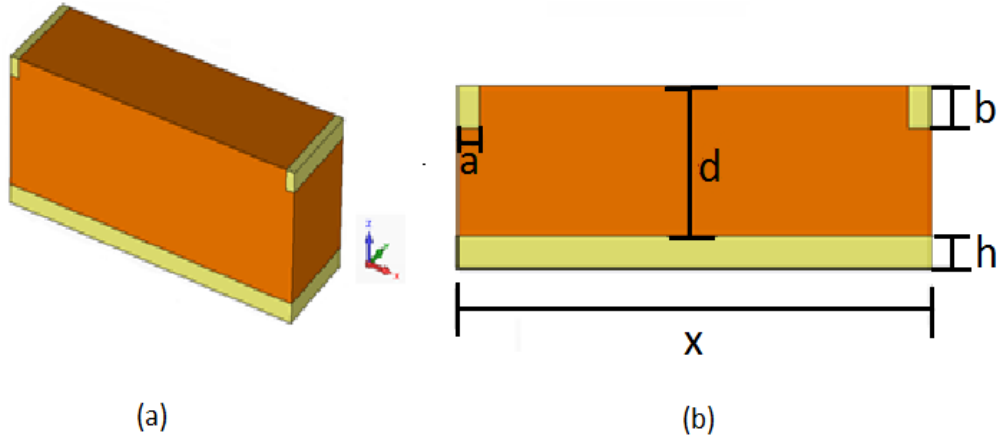


Figure 4-1. (a)The geometric structure of design, (b) the unit cell of structure with dimensions (side view).

The boundary conditions along x and y axis are selected to be electric and magnetic in order, whereas open boundary conditions with isotropic perfectly matched layer are used along z –axis. When the reflected radiation from material hits to the open boundary, it might be reflected back by the boundary. Perfectly match layer completely absorbs the incoming radiation. Thus, it ensures that there will not be any reflection from the boundary back to the designed material [85-86]. The frequency range for simulation is chosen to be the visible and near infrared in order to utilize solar energy efficiently.

The frequency dependent absorption ability of the structure is calculated by  $A(\omega) = 1 - R(\omega) - T(\omega)$  where  $A(\omega)$ ,  $R(\omega)$  and  $T(\omega)$  are absorption, reflectance and transmission respectively [87]. It is obvious that if one wants to maximize  $A(\omega)$ ;  $R(\omega)$  and  $T(\omega)$  should be minimized. Thus in this study, ground layer of the structure is chosen to be a metallic plate which prevents the transmission. In this case  $T(\omega) = 0$  and absorption will directly depend on the reflection,  $R(\omega)$  which can be calculated by the scattering parameters (S) gained from the simulation.  $R(\omega) = |S_{11}|^2$  where  $S_{11}$  is the ratio of power that reflects from port 1, to the power incident on port 1. The aim of this work is to minimize  $S_{11}$  to get perfect absorption.

#### 4.2.2. Result and Discussion

Parametric studies with respect to the dimensions of the structure are carried out to characterize the absorber. The dielectric thickness (parameter  $d$ ) is one of the important parameter for this structure. The magnitude of the absorption and the resonance frequency as a function of dielectric thickness are separately presented in Figure 4-2a. It is obvious from this figure that the resonance frequency and the absorption are highly dependent on dielectric thickness. By increasing parameter  $d$ , simultaneously the absorption enhances, reaches its maximum value, and starts to decrease. Moreover, resonant frequency is decreasing monotonously, with the increase in parameter  $d$ . Figure 4-2a represents that the highest absorption value (%99.99) which is obtained at 403.5 THz, when the parameter  $d$  is adjusted to be 135 nm. The other important parameter for our structure is the length of the aluminum strips (parameter  $a$ ) which are located at the top of the structure. The dependence of the absorption and the resonance frequency to this parameter is represented in Figure 4-2b. Here the variation is relatively small. Meanwhile, the thickness of the aluminum plate at the bottom (parameter  $h$ ) is set to be  $h=20$  nm which is greater than the skin depth of the aluminum. This is needed necessarily, in order to prevent the transmission through the structure.

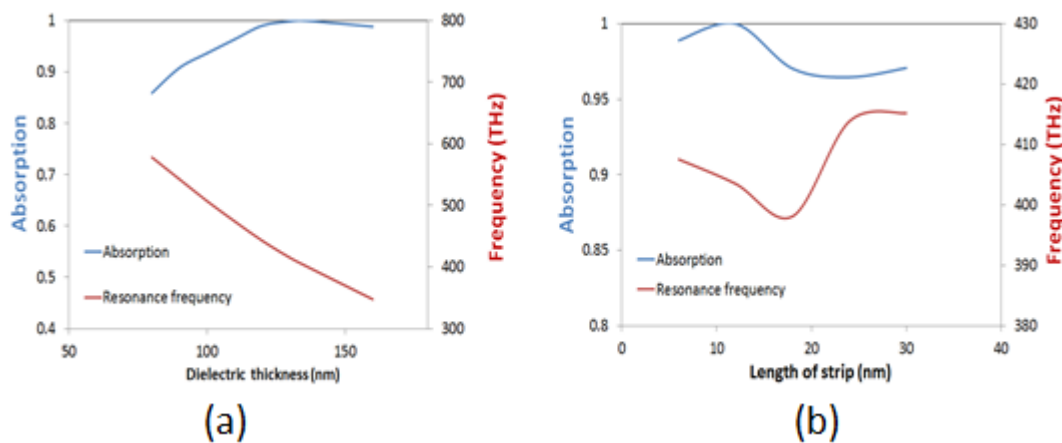


Figure 4-2. (a) Dependence of absorption and resonance frequency on (a) dielectric thickness, (b) on the length of the strips.

After carrying out parametric studies, the simulation results for each parameter to find out the optimum parameter values for the designed structure have been combined. Maximum absorption is obtained around 99, 99% at 403.5 THz when the parameters

were set to be  $d=135$  nm  $w=20$  nm  $a=12$  nm  $h=20$  nm  $x=420$  nm and  $y=125$  nm. Absorption and s parameter results which were obtained from the simulation for the final structure are shown in Figure 4-3.

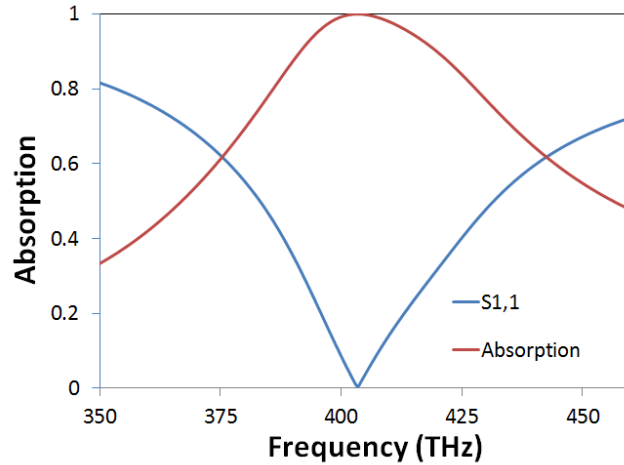


Figure 4-3. Reflection and absorption results obtained from the simulation. Geometric dimensions are:  $d=135$  nm  $b=20$  nm  $a=12$  nm  $h=20$  nm  $x=420$  nm and  $y=125$  nm.

The relative wave impedance of proposed MMA is also calculated and presented in Figure 4. As can be seen from Figure 4-4, at the resonant frequency, the real part and the imaginary part of the wave impedance are nearly  $R(\tilde{z}) \approx 1$  and  $Im(\tilde{z}) \approx 0$  respectively. This situation ensures the matching of the wave impedance with the impedance of free space, which results with the perfect absorption [88].

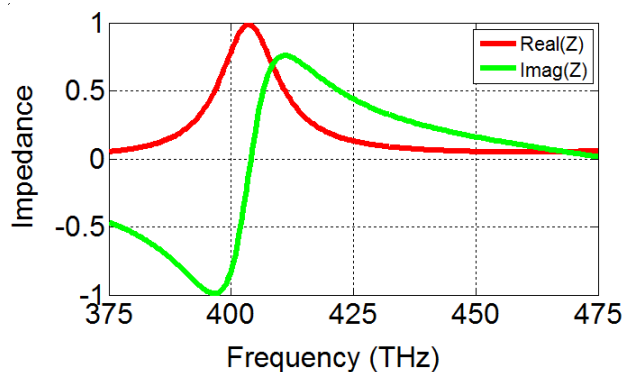


Figure 4-4. Real and imaginary part of the effective impedance.

The absorption spectra of the structure under different polarization angles have also presented for normal incidence as shown in Figure 4-5. The polarization angle has been changed from  $0^\circ$  to  $90^\circ$  with the step of  $30^\circ$ . It is found that the proposed MMA

has perfect absorption for all polarization angles and can be said that the design is polarization insensitive.

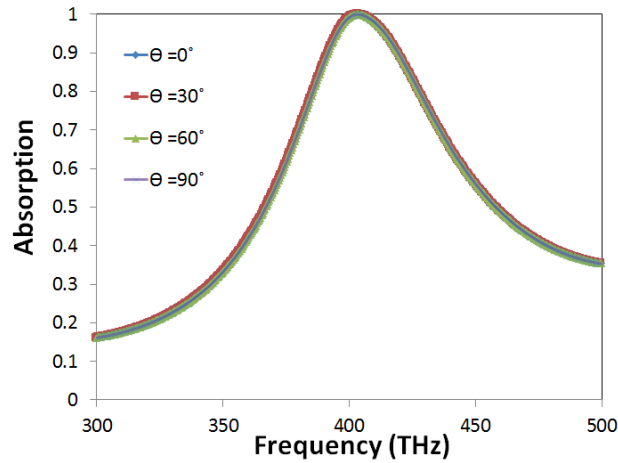


Figure 4-5. Simulation results for absorption under different polarization angle,  $\Theta$ , at normal incidence.

The results and discussion which were discussed up to now are for the normal incidence case. On the other hand, in reality, electromagnetic wave can strike to the absorber with an oblique angle. Because of this reason the absorption spectra under different incident angles have presented. Figure 4-6a and Figure 4-6b shows the transverse electric (TE) and transverse magnetic (TM) absorption curves for different incident angles respectively. For both cases the incident angle has been changed from  $0^\circ$  to  $90^\circ$  with the step of  $15^\circ$ . The magnitude of the absorption for each case is also presented beside the corresponding angle. According to the simulation results, there are some slight changes at the magnitude of the absorption for both TE and TM case. However it remains higher than % 99 for all cases, which means that stability is achieved and can be said that the structure is incident angle insensitive [89-90].

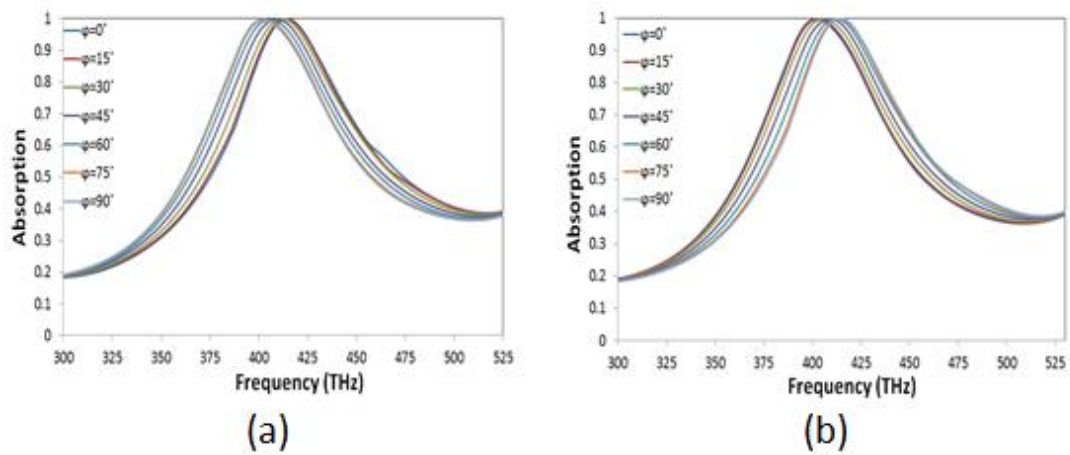


Figure 4-6. Absorption spectra for different incident angles (a) TE mode, (b) TM mode.

Moreover, fractional bandwidth (FBW) of the absorption region of proposed MTM absorber at resonant frequency have also calculated. FBW is the fraction of half-power bandwidth ( $\Delta f$ ) to the center frequency ( $f_0$ ) and gives information about the quality of the absorber. The bandwidth of the proposed structure can be seen in Figure 4-7. In our work  $\Delta f=89.67$  THz and  $f_0= 403.5$  THz according to that values FBW is found %22.2 which means the quality of the absorber is good with respect to the bandwidth.

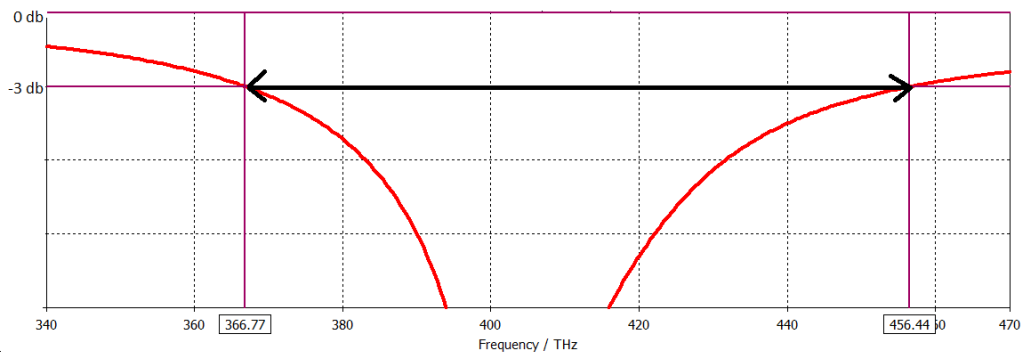


Figure 4-7. Half power bandwidth of absorber.

Electric field and surface current distributions at resonant frequency which are shown in Figure 4-8a and Figure 4-8b respectively, will help us to understand the operation mechanism of the structure. It can be clearly seen from Figure 4-8a that strong electric field localized near the strips, at the top, and on the top of the aluminum plate at the bottom. It can be said that, these are the locations which are responsible from absorption. From Figure 4-8b, it can be seen that the strong surface current takes place

on the two side of the structure which are antiparallel. In addition small amount of surface current takes place on the bottom aluminum plate.

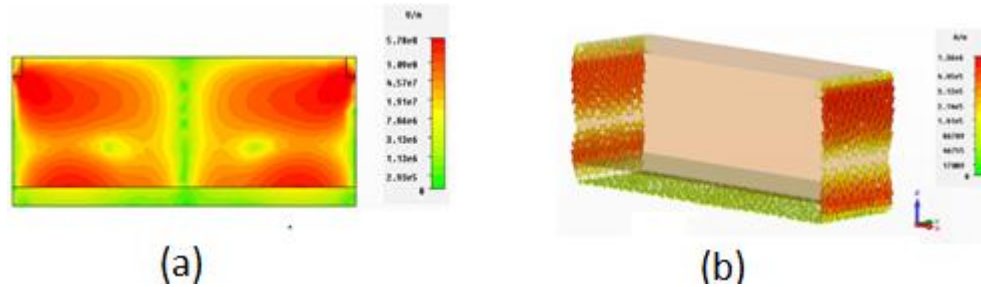


Figure 4-8. (a) Z–component of electric field distribution at 403.5 THz, (b) Surface current distribution of the structure at 403.5 THz.

### 4.3. Dual-Band Metamaterial Absorber

In the previous section, a single band metamaterial absorber design which consist of two metallic strip (source of the surface plasmon polaritons) embedded into the semiconductor layer is introduced. In This section, a new metamaterial absorber design which has four strips in its structure and gives dual band absorption response in the visible range is formed.

#### 4.3.1. Design and Simulation

The front view of the unit cell (as well as the geometric parameters) is presented in Figure 4-9. The geometry of the presented structure is composed of two identical long strips at the edges of the structure and other two other identical short strips located at the inner parts of the structure. The gap between the longer and shorter strips is represented with parameter “g” as shown in Figure 4-9. The mentioned stripes give rise to the dual band absorption response which will be presented in the next section. The denoted letters for the geometrical parameters in Figure 4-9, p, d, a, b, l, t and h represent the unit cell periodicity, dielectric spacer thickness, longer strip width, shorter strips width, length of the shorter strip, thickness of the strips and the thickness of the basement Aluminum (Al) plate correspondingly.

For this design, the metallic parts are aluminum where the dielectric is chosen as silicon dioxide ( $\text{SiO}_2$ ) because lossless characteristics. Al and  $\text{SiO}_2$  are selected as they are low costed, abundant materials and meets the needed minimum material properties

for this design.  $\text{SiO}_2$  is a lossless material. Therefore all the energy is absorbed in the aluminum parts. These types of designs can be used in thermo-photovoltaic (TPV) applications of metamaterials. The detailed information about thermo-photovoltaics will be provided in the chapter 7.

The complex dielectric constants of the used materials are taken from [84] and introduced into the simulation software. Periodic boundaries are used in  $x$  and  $y$  directions and perfectly matched layer are used in the propagation axis. The operation frequency for the numerical simulations are chosen to be the visible frequency regime.

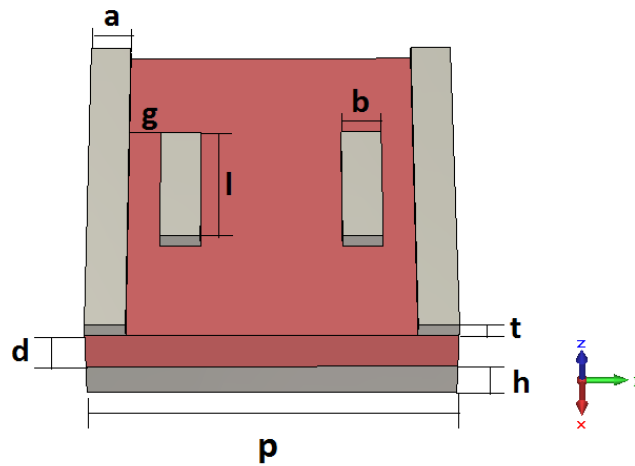


Figure 4-9. Unit cell geometry of the proposed metamaterial absorber.

#### 4.3.2. Result and Discussion

The design mention in the previous section, exhibits dual band absorption response at 654.9 THz and 708.3 THz respectively. The Obtained absorption and reflectance spectrum are given in Figure 4-10. The absorption levels are 99.8 % and 99.1% at 654.9 THz and 708.3 THz correspondingly. The numerical study shows that the optimum parameters are  $d=60$  nm  $w=20$  nm  $a=b=50$  nm  $h=50$  nm  $p=455$  nm and  $l=170$  nm and  $g=40$  nm for the designed structure in order to have dual band absorption with maximum absorption levels in the visible range.

In order to show better understanding of the absorption behavior of the design, field distributions at resonant frequencies are obtained and presented in Figure 4-11.

Moreover, the parametric studies in terms of the geometric dimensions of some important parameters are also generated and given in Figure 4-12.

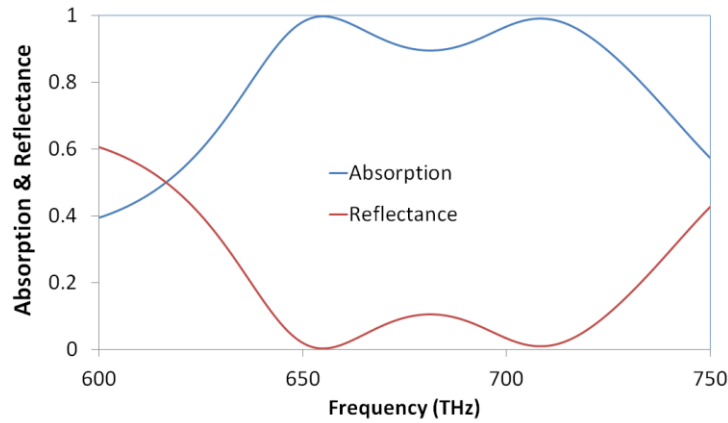


Figure 4-10. Reflection and absorption spectra. Geometric dimensions are:  $d=60$  nm  $w=20$  nm  $a=b=50$  nm  $h=50$  nm  $p=455$  nm and  $l=170$  nm and  $g=40$  nm

The field distributions at 654.9 THz and 708.3 THz are demonstrated in Figure 4-11. The electric field (E-field) distribution of the structure at the place where the first absorption response took place is represented at Figure 4-11a. Here, electric field is concentrated under the edges of the short strips. Moreover, electric response is also localized on two sides of the design and at the middle of the structure. These are the places where the origin for the electric responses for 654.9 THz are formed. Additionally, the magnetic response for the absorption for 654.9 THz is mainly generated by the interaction between the shorter strips and the Al plate at the ground. This condition is virtualized in the Figure 4-11c. Due to the coexisting electric and magnetic effects, the total absorption occurred at 654.9 THz. The origin of the resonance formed at 708.3 THz, is the interaction between the longer strips with the short one as shown in Figure 4-11 b and d. These interactions helped generation of the electric and the magnetic responses. So that the simultaneously generated responses matched the impedance of the absorber with the free space and the total absorption is fulfilled.

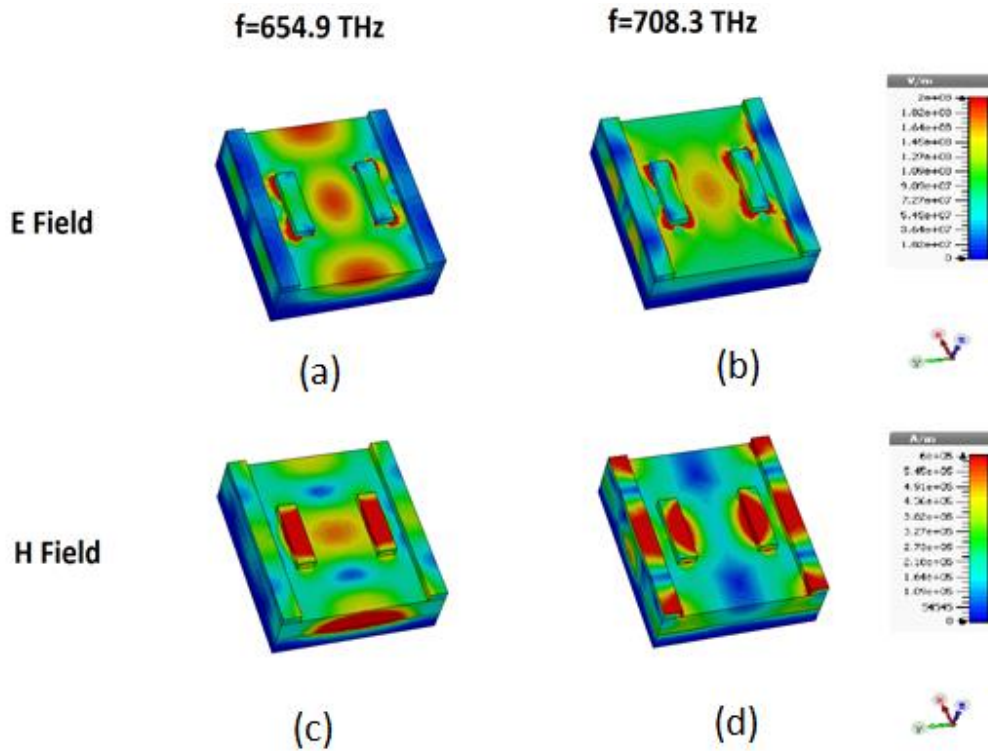


Figure 4-11. Field distributions at resonance frequencies. (a) Electric field distribution at 654.9 THz, (b) Electric field distribution at 708.3 THz, (c) magnetic field distribution at 654.9 THz, (d) magnetic field distribution at 708.3 THz

The underlying working mechanism of the design is investigated by analyzing the dependence of the absorption response on to the geometrical variables. In order to reveal the effects of the geometric variables, some important parameters are selected and the variation of the absorption spectra is analyzed.

Firstly, the thickness of SiO<sub>2</sub> layer is varied and the absorption spectra is investigated as shown in Figure 4-12a. The thickness of the SiO<sub>2</sub> layer (parameter “d”) is critical as it helps the coupling between the basement aluminum plate and the strips located on SiO<sub>2</sub> layers. When the thickness is increased starting from 40 nm up to 60 nm, blue shift and the enhancement of the absorption levels are observed. However, at the thickness of 70 nm the absorptions magnitudes of both of the bands became lower when compared to the optimum thickness. The thickness above and below 60 nm are not enough to couple the resonances between the strips and the Al plate. Under this circumstances, the requirements for the generation of the magnetic response are not

provided. So that the perfect absorption was not observed. For the perfect absorption, the mentioned parameter are needed to spark the magnetic response so that the perfect absorption will take place.

The other crucial parameter that determines the absorption magnitude is parameter “g”. This parameter represents the gap between the short and the long strips. The variance of this parameter is given in Figure 4-12b. The optimum gap distance is observed when “g” is selected as 40 nm. Below this length, the second resonance tends to become weaker while above the optimum length, the first resonance starts to be weakened. The optimum distance between the strips are critical as it makes the strips to interact with each other which couples them and creates the electric and magnetic responses. Hence this path ends with the impedance matching and the perfect absorption.

The width of the strips are also effects the place and the level of the absorption as shown in Figure 4-12c. When the widths of the strips are small ( $a=30$  nm), interaction between the strips give rise to the weaker absorption resonances especially for the first resonance. However, as the widths starts to become larger, the absorption behaviors caused by the strips start to become stronger up to  $a=50$  nm. This results with the dual band absorption. Increasing the width more than 50 nm results with the blue shift to the out of the spectrum. In addition, the absorption magnitudes of the resonances also becomes lower due to the insufficient electric and magnetic resonance and mismatch of the impedance. As a result, the absorption behavior is directly related with both of the strips. The width of the strips are equal and denoted with the letters of “a” and “b” ( $a=b$ ).

Lastly, the absorption results under different polarization angles are analyzed and effects are given in Figure 4-13. The demonstrated absorber model in Figure 4-9, has four folded symmetry. Therefore, as it is expected the absorption spectra of the given design is insensitive for various polarization directions.

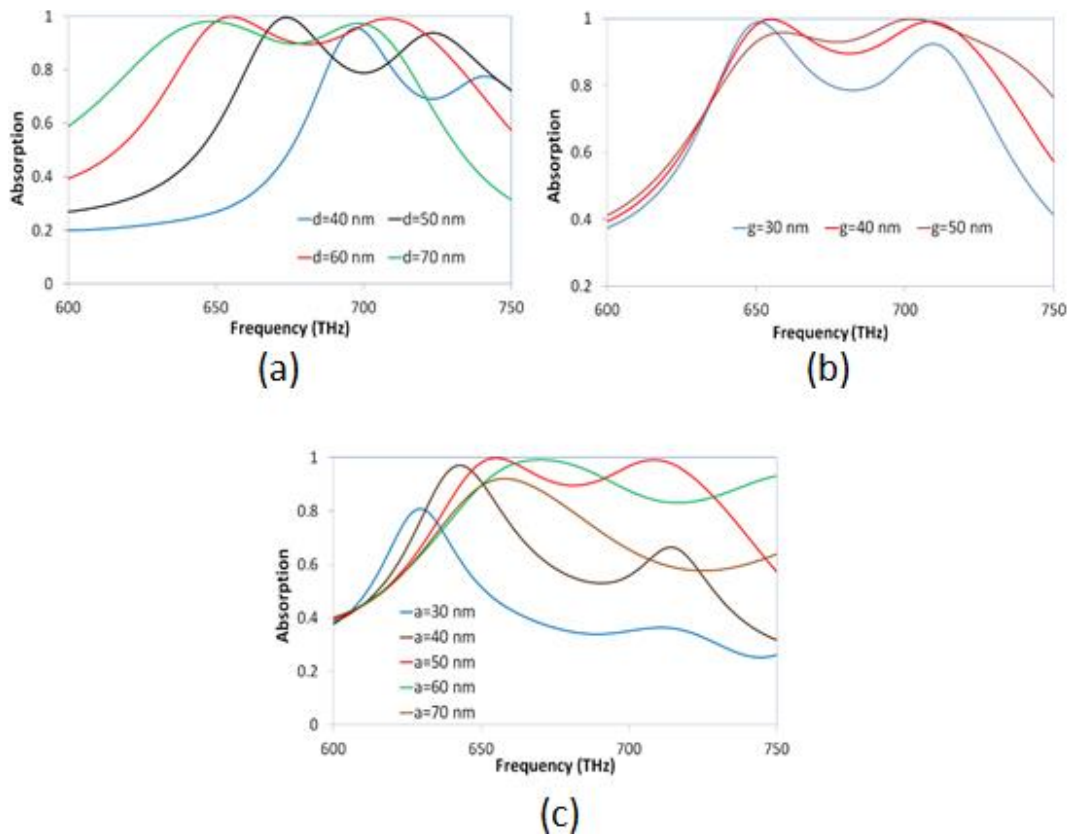


Figure 4-12. Dependence of the absorption response on a) SiO<sub>2</sub> thickness, b) the gap between the strips, c) the width of the strips.

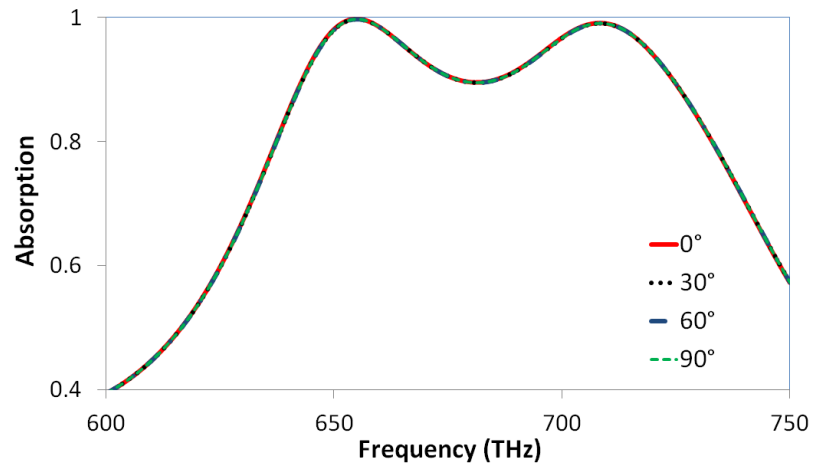


Figure 4-13. Polarization spectra of the proposed absorber.

#### 4.4. Conclusion

In this chapter, two different metamaterial absorber model are proposed. These absorber has potential to be used for utilizing the solar light. In addition to the solar radiation, they can be used for detecting and sensing the visible light. However, the absorption behavior of the introduced designs are not completely meet the necessary

standards for using them as high efficient solar cells. The wider absorption range is crucial for solar cell applications.

Here in this chapter, the single band absorber is formed by two identical strips. For dual band absorption two sets of identical strips are used to obtain dual band response. However, multiband absorption mechanism is still not clear enough. Moreover, the symmetricity of the designs are needed to be improved in order to have the less incident angle insensitive metamaterial absorber designs.

## CHAPTER 5

### MULTI-BAND METAMATERIAL ABSORBER TOPOLOGY

#### 5.1. Introduction

In the previous chapters, designing and analyzing methodologies of a metamaterial absorber are introduced. In chapter 4, single and dual band absorber designs are formed by using strip shaped resonators. However, it is essential to introduce a logical way of forming multiband metamaterial absorber designs in order to reveal the working mechanism of the multiband absorbers.

Forming multiband or wideband metamaterial absorber for high frequencies are mainly provided by adding multiple layers or utilizing various dielectric materials in the lateral directions. For example, He *et al.* [87] numerically demonstrated an ultra-broadband, metamaterial absorber designed by combining three pairs of metal-dielectric layers with different dielectric constants. They numerically show that their polarization-insensitive design has an ultra-broadband absorption response over the solar spectrum. Dayal *et al.* [91] proposed a metamaterial absorber design which consist of, tri-layers of metal–dielectric–metal disks. Their design works between the wavelengths range of 3-10  $\mu\text{m}$  and have the multiband characteristics. In their design, they have utilized different dielectric materials which determine the absorption bands and forms the multiband character.

However, for infrared frequencies, there has not been any study done for three layers of metamaterial absorber design, in order to form the multiband absorber topology.

In this chapter, a new multiband metamaterial absorber design (composed of only three layers) is introduced and the multiband topology is formed by using the differently sized quadruplet resonator. In order to understand, characterize and form the multiband topology, the individual responses of each quadruplets as well as the analysis of the geometric parameters of the structure are examined.

### 5.2. Design and Simulation

The unit cell of the proposed metamaterial absorber consist of three layers; which are aluminum layer at the bottom, resonators at the top and a silicon layer between these metallic layers. The bottom layer is utilized in order to prevent the transmissions through the structure as the thickness of this plate is greater than the skin depth of aluminum in the studied frequency range. The geometric structure of the unit cell and the geometric dimensions associated with the parameters are given in Figure 5-1 and Table 1 respectively. The metallic parts of the structure are aluminum (Al) while silicon (Si) is used between the Al layers. The topological formation and the uniqueness of the design is arisen by the arrangements, dimensions and the orientation of the resonators. There are three pairs of quadruplets with different geometric dimensions. They are arranged so that the dimensions of each pairs of quadruplets increases as going from the inner parts of the design through to the outer portion. This arrangement raises to the generation of the multiband absorption resonances at different frequency positions which will be discussed in the next section. In addition to this arrangement, the orientation of quadruplets has 45°angle with the x-axis which reduces the required space for the resonators and also reduces the material cost. Having differently sized resonator pairs in a combined unit cell, gives rise to the individual absorption response of each of these quadruplets at a certain frequency. The contribution of the quadrupled resonators to the absorption spectrum will be discussed in the next section.

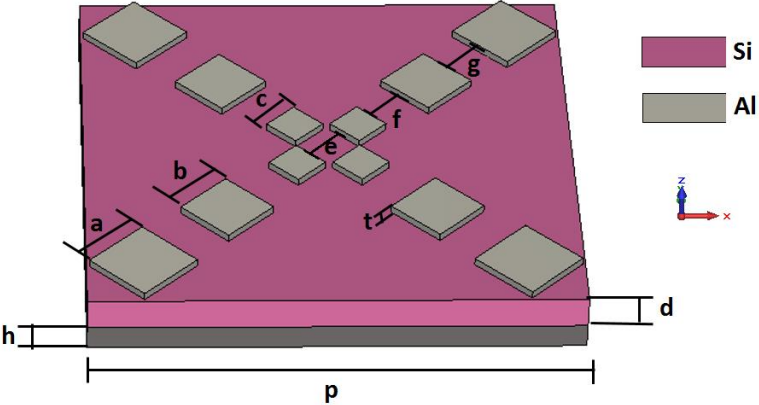


Figure 5-1. Unit cell design of the proposed absorber.

In order to characterize the unit cell, numerical simulations are performed. The numerical simulations are carried out by a simulation software which is based on finite integration technique and has great capability to solve Maxwell's equations. In the numerical simulations, Al and Si are modeled by introducing their frequency dependent electrical parameters into the simulation software which were extracted from Palik's book [84]. Throughout the numerical analysis, appropriate boundary conditions (periodic in  $x$  and  $y$  directions and open boundaries along  $z$ -direction) and appropriate polarization for the incident electromagnetic radiation (E field polarized along  $x$ -direction whereas H field polarization is in  $y$ -direction) are used. All the numerical simulations are performed under transverse electromagnetic (TEM) wave unless it is stated.

Optical absorption responses of the proposed structure can be calculated by using the known equation  $A(\omega) = I - R(\omega) - T(\omega)$ . Here  $A(\omega)$ ,  $R(\omega)$ , and  $T(\omega)$  represents the frequency dependent absorption reflectance and transmittance respectively. When the bottom layer is thick enough i.e. thicker than the skin depth of the material,  $T(\omega)$  can be neglected because the ground layer becomes optically opaque. Under this circumstances the equation reduces to  $A(\omega) = I - R(\omega)$ . Therefore the absorption can be calculated by using the scattering parameter gathered from the numerical simulations.

Table 5-1. Geometric dimensions of the design.

<b>Parameter</b>	<b>a</b>	<b>b</b>	<b>c</b>	<b>d</b>	<b>e</b>	<b>f</b>	<b>g</b>	<b>h</b>	<b>t</b>	<b>p</b>
<b>Value (nm)</b>	150	135	80	65	100	100	100	50	15	980

### 5.3. Results and Discussion

The proposed metamaterial absorber design has five absorption peaks in the infrared frequency regime which is presented in Figure 5-2. When the optimized parametric values given at Table 5-1 are used, absorption responses are observed at 148.9 THz, 179.8 THz, 213.1 THz, 269.8 THz, and 287.2 THz with the absorption levels of 98.90 %, 99.39 %, 86.46 %, 92.80 % and 97.96 % respectively. In order to better understand the origin of each of these resonances, the individual responses of each of the quadruplet resonators, as well as their field distributions at resonance frequencies, are investigated and multi-band topology in which the number of resonances depend on

the number of the quadruplets used in the unit cell is formed. Moreover, the dependencies of the resonant frequencies and the absorption levels on the geometric parameters are also examined to get a better insight into the absorptivity mechanism and verify the multiband topology.

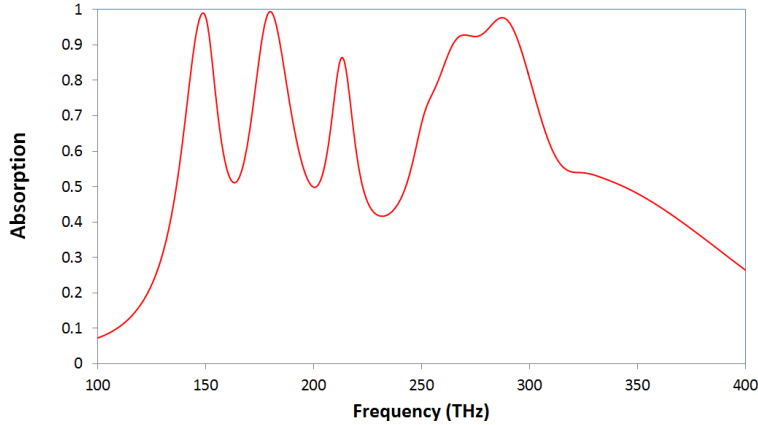


Figure 5-2. Absorption spectrum of the proposed absorber.  $a=150$  nm,  $b=135$  nm,  $c=80$  nm,  $d=65$  nm,  $e=f=g=100$  nm,  $h=50$  nm,  $t=15$  nm and  $p=980$  nm.

### 5.3.1 Multi-band Topology

In this part, the absorption characteristics of the proposed absorber and the contribution of each of the resonator pairs to the absorption band are investigated and analyzed. The individual absorption responses of different pairs of resonators (quadruplets) is presented in Figure 5-3. Figure 5-3a represents the absorption result when the resonators are not utilized in the design. Nevertheless, it is clear that the structure exhibits a wide band absorption response with a lower absorption level. The origin of this resonance is the interaction of the Si layer with the bottom Al layer which gives rise to the resonance at around 262 THz [92]. In order to reveal the absorption responses of each quadruplets, each pair is included individually into the design and the electromagnetic responses are monitored. Firstly, the inner quadruplet, which is the smallest resonator pair, is included. When this resonator pair is added, (Figure 5-3b), three resonances are observed. Here, the contribution of the inner quadruplet is occurring at 207.4 THz where the other two resonances are formed because of the interaction of the bottom Al plate and the Si layer as explained before. It can be clearly seen that the wide-band resonance in Figure 5-3a is splitted into two peaks and formed a dual band response. Note that the absorption level are also enhanced because of the

interaction. After observing the response of the inner pair, second quadruplet which is middle in size and has the middle position on design, is individually analyzed. The influence of this resonator pair is presented in Figure 5-3c. As it can be seen from here that a new resonance at 180.1 THz is formed. This absorption resonance takes place slightly left side of the response caused by the inner resonator pair. The influence of the outer resonator pair is presented in Figure 5-3d. The outer pair, which is the largest in dimension, gives the left most resonance at around 146.2 THz. Note that the other provided small responses are due to the interactions between this quadruplet pair and the other parts of the structure as happened for the other resonator pairs. Furthermore, as the position of the resonators moved from inner to the outer with respect to the design, the resonance frequency is also shifting to the left portion of the electromagnetic spectrum (redshift) which can be explained by the interactions of the metamaterial elements.

After investigating the individual responses of the metamaterial elements, all the quadruplets are combined in one unit cell. For the final condition, the absorption spectra is given in Figure 5-3e. It is clear that, combining all the quadruplets in one design, combines the individual responses of metamaterial elements. Therefore, five absorption peaks (three of them coming from the quadruplets and two of them coming from the Al - Si interactions) are formed. If one compares the position of the resonance frequencies of each individual quadruplets and the resonant position of the combined structure, it can be seen that, these positions are matched with a small frequency redshift. This is mainly because of the interaction between the resonator pairs with each other and the other parts of the structure. This interaction not only affected the resonance frequency, but also caused the enhancement in the absorption magnitudes of the resonances. In addition, this situation proves the above explanations for the multiband topology.

As discussed above, three absorption peaks are obtained by adding differently sized three quadruplet pairs to the design. It can be concluded that, the number of absorption resonances depend on the number of quadruplets added to the design. Hence, by carefully designing and adding “n” number of differently sized quadruplets to the unit cell design, will provide “n” number of absorption resonances caused by these quadruplets (excluding the interaction resonances) [93].

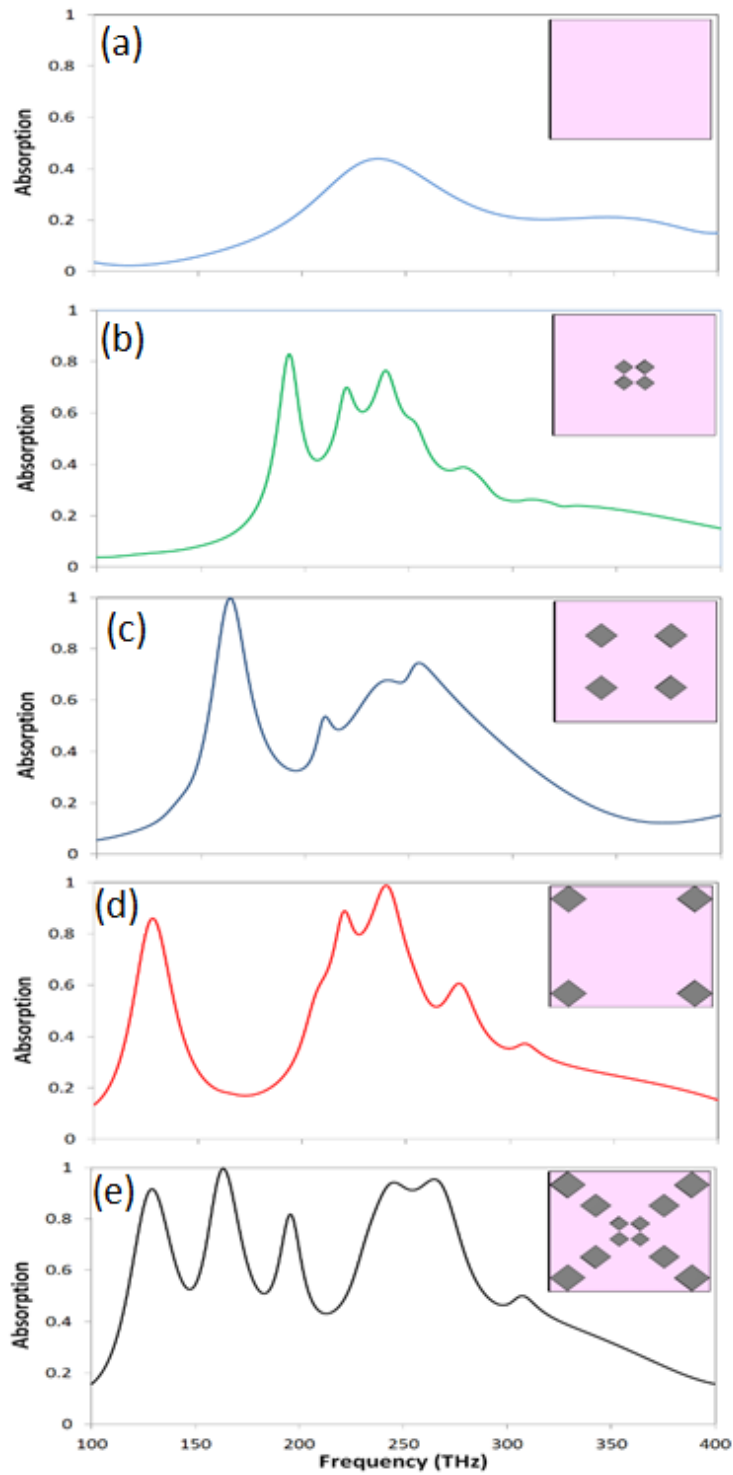


Figure 5-3. Absorption spectra for different geometric structures of the design. (a) Without resonators, (b) only inner quadruple resonators are used, (c) only middle quadruple resonators are used, (d) only outer quadruple resonators are used, (e) combined structure.

In addition to the above explanations, the topology can also be explained by analyzing the field distributions of the absorber at resonance frequency. The results of electric

field, magnetic field and surface current distributions are given in Figure 5-4, Figure 5-5 and Figure 5-6 respectively. Note that electric field and magnetic field profile are given for Y-Z axis and X-Z axis, while surface current distributions are presented at the center of related quadruplet. For the first resonance at 148.9 THz, electric and magnetic field is localized around the outer quadruplet. The concentration of strong electric field like this, separated the opposite charges which coupled the bottom Al plate and the outer quadruplet. This coupling created a circulating current profile around the outer quadruplet (Figure 5-6a) which formed the origin of the magnetic response. Hence, the simultaneously observed electric and magnetic resonances yields perfect absorption. Moreover, from Figure 5-4a and 5-5a, small interactions between the outer quadruplet and the other resonators are observed. Although these small interactions influenced and enhanced the absorption response at this frequency, the origin of the first resonance is the presence of the outer (largest) quadruplet. The results obtained for the second resonance at 178.9 THz and the third resonance at 213.1 THz shows the same type of electric and magnetic field distributions. However, for these resonances, the absorption responses are originated from different resonator elements. Second resonance is mainly caused by the middle quadruplets while third one is created because of the presence of the inner quadruplet. Furthermore, not only the highly concentrated distributions are observed, but also small interactions between the resonator pairs can also be seen from the field distributions given at Figure 5-4 (b)-(c) and Figure 5-5 (b)-(c). As it was discussed before, the fourth and the fifth resonances are caused by the bottom Al and Si interactions which can also be seen by the field distributions given at Figure 5-4 (d)-(e) and Figure 5-5 (d)-(e). Moreover, for the fourth resonance, the circulating current loop occurred not at a specific location, instead it took place within the structure. This condition satisfies that this resonance is caused by the structures itself. For the fifth resonance, antiparallel current profile (Figure 5-6e) are observed on the Si layer and the bottom Al plate. These antiparallel currents created the magnetic response. In addition, the electric and the magnetic field located around the quadruplets causes the enhancement of the absorption level of the fourth and the fifth resonances. Due to this interaction, the absorption spectra (given at Figure 5-3a with the magnitude 0.37) splits into two and enhances to the levels of 0.91 and 0.98

respectively. Therefore these results are consistent with the above results and explanations. Hence the multiband topology is formed.

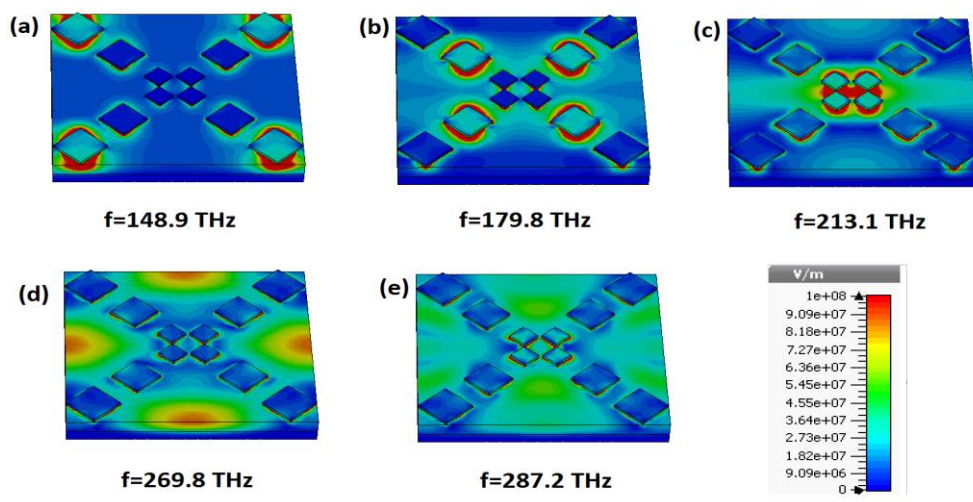


Figure 5-4. Electric field distributions of the structure at (a) 148.9 THz (b) 179.8 THz, (c) 213.1 THz, (d) 269.8 THz, (e) 287.2 THz.

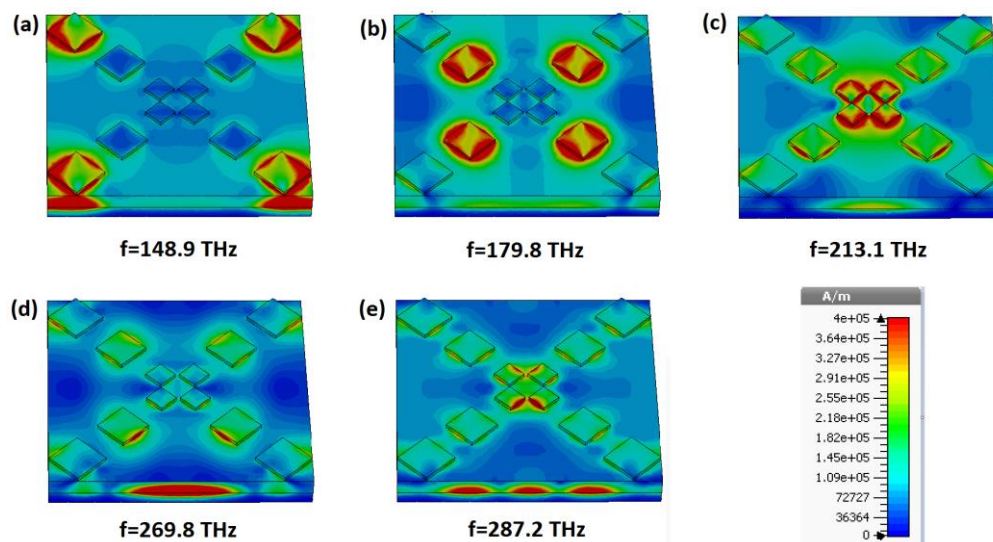


Figure 5-5. Magnetic field distributions of the structure at (a) 148.9 THz (b) 179.8 THz, (c) 213.1 THz, (d) 269.8 THz, (e) 287.2 THz.

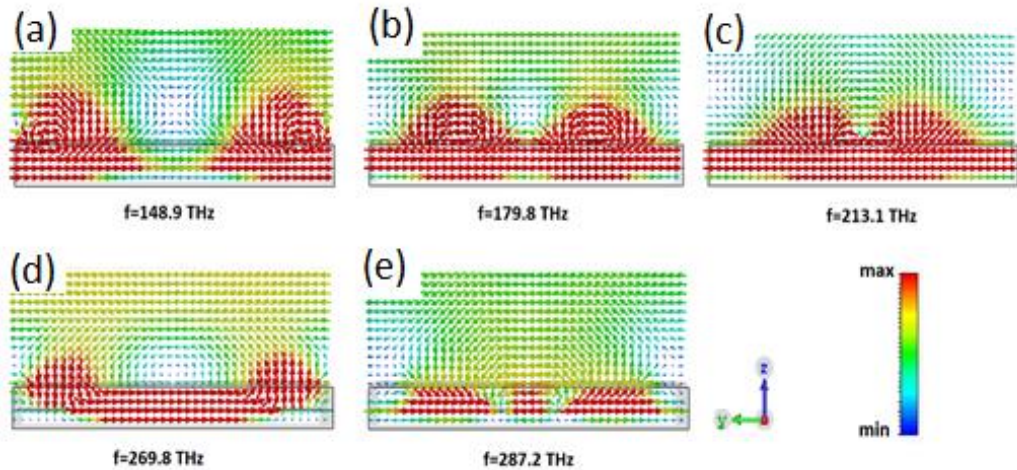


Figure 5-6. Surface current distributions of the structure at (a) 148.9 THz (b) 179.8 THz, (c) 213.1 THz, (d) 269.8 THz, (e) 287.2 THz.

### 5.3.2 Geometrical Effects on the Absorption Response

In order to understand the effects of the geometric parameters on the absorption characteristics of the absorber, the dependencies of the absorption strengths and the resonant frequencies on the geometric parameters are examined. To get an insight into the absorption mechanism, the most important parameters, which are the dimensions of the resonators (parameter a, parameter b, parameter c), dielectric thickness (parameter d) and the periodicity of the structure (parameter p), are chosen and the variation of the absorption spectra when these parameters are altered (while the other parameters are kept constant) are investigated.

The dimensions of the quadruplets have the crucial role in this absorber design. Therefore the dimensions of quadruplets are chosen carefully in order to obtain one resonance from each quadruplets. The results for the dimension variation of quadruplets are demonstrated in Figure 5-7a-c while Figure 5-7d represents the variation of absorption spectrum when all the dimensions in *x* and *y* directions are altered simultaneously with a defined ratio N. For the mentioned Figures, the red curves represent the desired absorption results. Therefore, for the perfect absorption, those geometric parameters are chosen as the optimum parameters.

When the dimensions of outer quadruplet are decreased from 150 nm to 130 nm, it is obvious that the resonance is shifting to the right portion of the absorption spectrum (blue shift) while the others are not affecting much (Figure 5-7a). This blue shift occurs in the way so that when the parameter “a” is selected to be 130 nm, it can be seen that the first resonance is relocating at the position of second resonance. As explained before, second resonance forms due to the middle quadruplets. Under this circumstances, it is clear that the dimensions of the quadruplets are important to form the resonances at the different position of the spectrum. The similar explanations can be followed for Figure 5-7a and Figure 5-7b where the second resonance tends to shift to the position of the first resonance, and where the third resonances is shifting through the positing of the forth resonance respectively. It is certain that, when parameter “b” is adjusted to have the same value with parameters “c”, the position of the resonances will be overlapped. Furthermore, third resonance tends to disappear when parameter “c” is lessen.

Maximum dimensions for the Figure 5-7a-c is selected to be the optimum dimensions of each quadruplets, as it is not possible to make more enhancement in the dimensions as they exceed the Si layer in  $x$  and  $y$  directions. Because of this reason, parameter “N” is defined which simultaneously changes all the parameters in  $x$  and  $y$ -directions. The results for this parameter are given in Figure 5-7d. Decreasing the dimensions by a factor of 0.8, lowers the sizes of quadruplets and causes the shift in the resonance frequency and absorption strengths. Moreover, the comprehension of the structure, disturbs the constructive interaction occurred between the metamaterial elements. Eventually, this situation causes with a reduction of the absorption strength and a blue shift of resonance frequencies. In addition increasing the dimensions by the factor of 1.2, destroys the second and third resonances and reduces the absorption level of the first resonance.

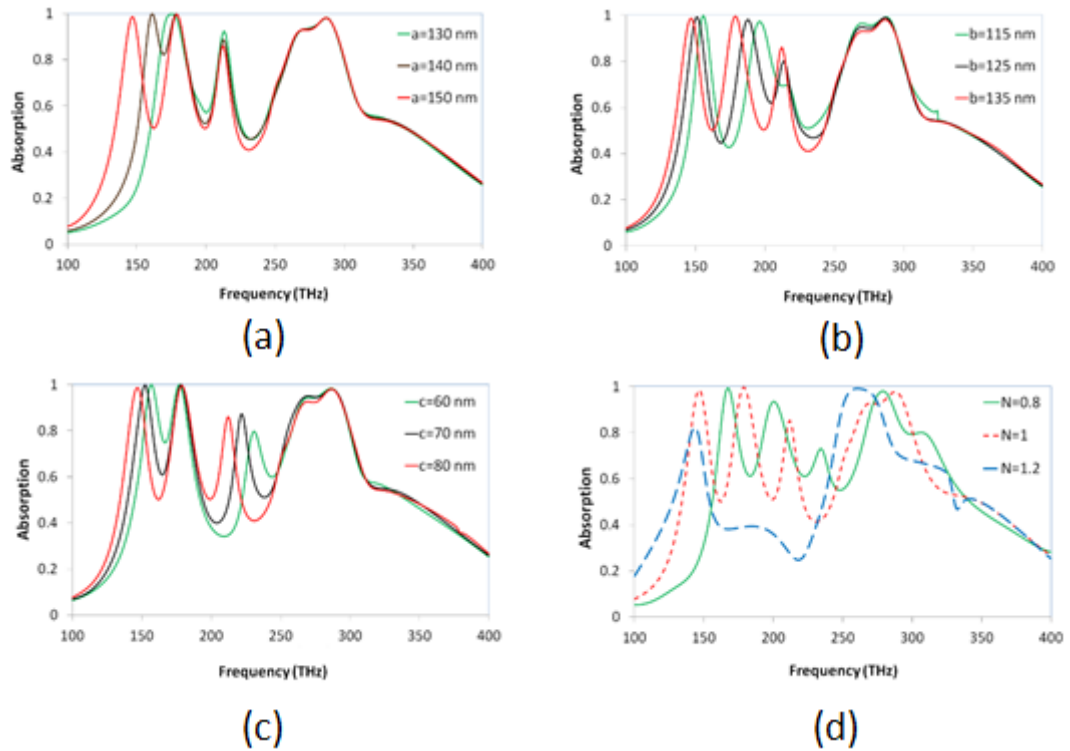


Figure 5-7. Variation of absorption spectra for a) outer resonator pairs (parameter a), b) middle resonator pairs (parameter b), c) inner resonator pairs (parameter c), d) when all the dimensions are varied (parameter N).

In addition, dielectric thickness (parameter d) and the unit cell periodicity (parameter p) are also examined and the variations are observed (Figure 5-8). The thickness of the Si layer mainly causes the coupling between the electric responses occurred on the quadruplet resonators with the bottom Al layer. Thus, because of this coupling, the magnetic response is created and this condition makes the effective impedance of the absorber to be equal to the impedance of the free-space. It is observed that not only the absorption rates are changing with “parameter d”, but also the number of resonances created are also effecting. Therefore, the absorption strength and the number of resonances created are simultaneously analyzed with different thicknesses of Si layer and represented in Figure 5-8a. It is clear from here that, second and third resonances have their maximum when “d” is selected to be 65 nm (optimum thickness). Although the first resonance has its maximum when “d” is around 70 nm, selecting 70 nm as the optimum parameter would result with the reduction at the total absorption strength due to the relatively lower absorption rate of the other resonances for this thickness. Furthermore, fourth resonance has its minimum level around d=65 nm. Reduction in

the absorption level of the fourth resonance at  $d=65$  nm, caused the split in the fourth resonance and this yields to the formation of the fifth resonance.

Lastly, Figure 5-8b represents the dependence of the absorption spectrum to the unit cell period. When period is increased, first resonance, which is created by the outer quadruplet, is much more affected than the other resonance. This is mainly because of the changing of the position of these resonators relative to the structure which disturbs the created electric and magnetic responses of the structure. Hence the maximum absorption frequencies are effecting. Furthermore, increasing the periodicity results with the increase in the absorption levels of the fourth and the fifth resonances. As discussed before, this resonances are caused by the interaction of the Si layer and the bottom Al plate. Because of this, increasing the area of these materials increases the absorption strength. However, scaling up the dimensions also increases the material cost. Therefore the smallest possible period which is  $p= 980$  nm is chosen for this metamaterial absorber.

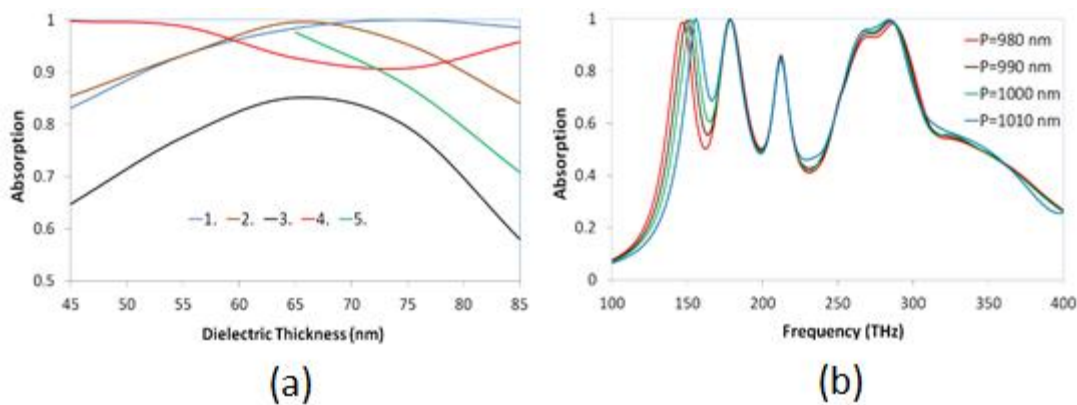


Figure 5-8. Variation of absorption spectra for a) dielectric layer thickness (parameter  $d$ ), b) period of the absorber (parameter  $p$ ).

In addition, effective permittivity ( $\epsilon$ ) and effective permeability ( $\mu$ ) of the absorber are extracted. The results of frequency dependent extracted effective permittivity is given in Figure 5-9a where Figure 5-9b represents the effective permeability results. From these results, it is observed that the proposed absorber shows double negativity (both the real part of  $\epsilon$  and the real part of  $\mu$  are negative) around the resonant frequency.

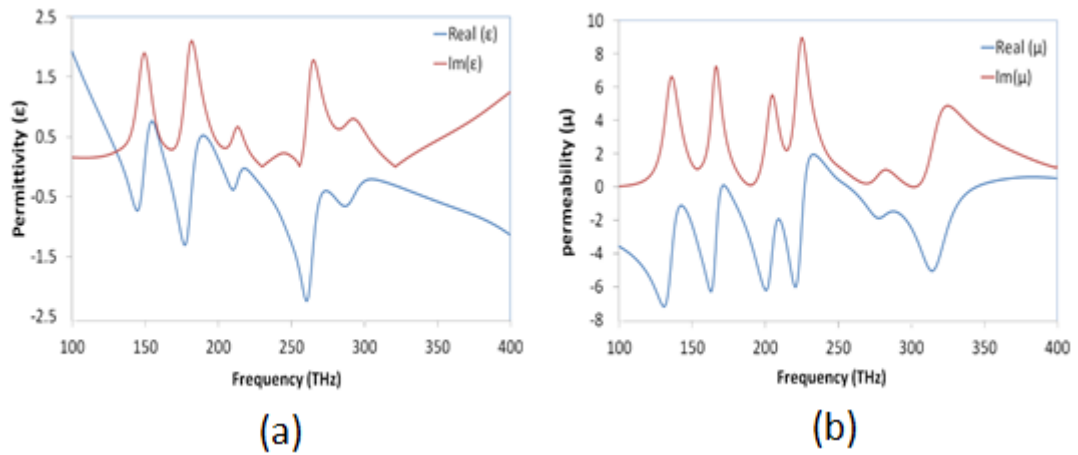


Figure 5-9. Extracted effective parameters a) effective permittivity b) effective permeability.

Moreover, absorption characteristics under different polarization angles for normal incidence are analyzed and results are given in Figure 5-10a. Due to the four-folded symmetric geometric design of the absorber, it provides polarization independent characteristics under transverse electromagnetic (TEM) wave mode.

In order to fully characterize performance of the absorber, the absorption spectra under different incident angles are analyzed. Figures 5-10b represents the absorption results for transverse electric (TE) mode while Figure 5-10c shows the variation spectra for transverse magnetic (TM) mode. When the results for TE and M modes are compared, one can say that the TE mode is much more sensitive to the incident angle than TM mode. Especially, when the incident angle “ $\theta$ ” is  $45^\circ$ , the third resonance is almost disappeared. Furthermore, beyond  $45^\circ$ , absorption levels for all the resonances at TE mode are reduced to less than 0.6. This is due to the fact that the intensity of the magnetic field component of the incident radiation is dependent on the incident angle “ $\theta$ ” and it becomes smaller as the “ $\theta$ ” becomes greater [31-32]. Thus, in this case the magnetic responses are not effectively excited. Eventually the inefficient excitation of the magnetic polaritons results with increase in the amount of reflected radiation, impedance mismatch and finally the loss of absorption resonances. However, the absorption strength is still greater than 0.9 (except the third resonance which is around 0.6) even when “ $\theta$ ” reaches to  $45^\circ$ . Therefore, it can be commented that the introduced absorber exhibits the previously mentioned absorption characteristics over a vast range of incident angles for TE and TM modes.

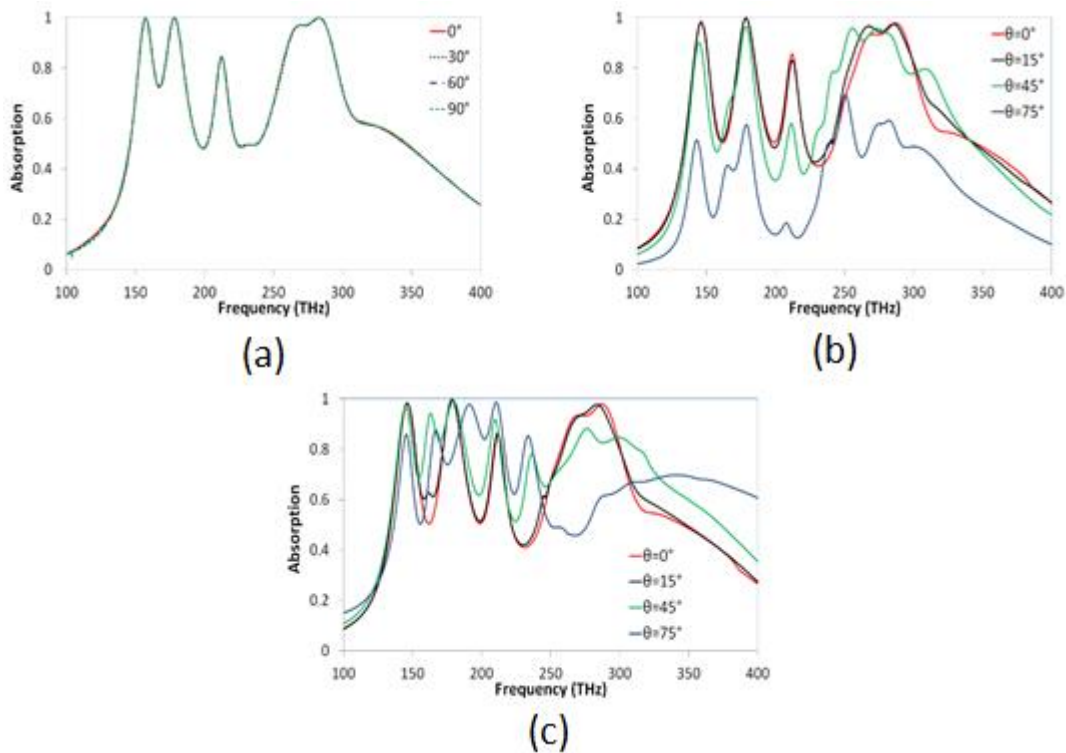


Figure 5-10. a) Absorption spectra for various polarization angles for TEM mode b) absorption spectra for various incident angles for TE mode c) absorption spectra for various incident angles for TM mode.

#### 5.4. Conclusions

In conclusion, in this work, a metamaterial absorber design formed by the combination of the three effective layers is introduced. Unlike the numerous studies which are mainly originated by the combination of the multiple layers in the literature, multiband is formed by utilizing only the three effective layers. The analysis and characterization of the multiband resonances are carried out and the multiband topology is formed. Moreover, the origins of the resonances are demonstrated by analyzing the field distributions of the absorber at resonant frequencies. In addition to better understand the absorption mechanism, the dependency of the absorption on the geometric parameters is also presented. As a conclusion, the proposed design serves the polarization and incident angle insensitive characteristics and the introduced multiband metamaterial absorber design can be good candidate for the applications in solar energy, sensing applications, absorption of solar radiation, detection and imaging in the solar spectrum.

## CHAPTER 6

### MULTIBAND METAMATERIAL ABSORBER FOR THERMO- PHOTOVOLTAIC APPLICATIONS

#### 6.1. Introduction

In the previous chapter, the logical mechanism of forming multiband metamaterial absorbers is introduced. However, solar energy harvesting through the metamaterial absorbers for can be realized by two different types of applications. In this chapter, a new metamaterial absorber design is introduced for thermo-photovoltaic application of solar energy.

Heat or thermal energy can be converted into usable forms of energy (mainly electricity) by the utilization of thermo-photovoltaics. These devices are the combination of an absorber/emitter, a photodiode, and an external heat source. [21-26]. The working mechanism of thermo-photovoltaics start with the absorption and re-emission of the energy coming from the heat source. Re-emitted radiation can be used by the photovoltaic cells to convert solar or heat energy into the electricity. Therefore, the absorption property of the metamaterial absorber can be used to capture the solar radiation by the integration of such absorbers into the photovoltaic and/or thermo-photovoltaic systems. In this sense, a metamaterial absorber can be used to improve the miniaturization and the efficiency of thermo-photovoltaics or photovoltaics.

Most of the previous studies focused on only one frequency region. For example Ayas *et al.* [46] worked on a metamaterial absorber structure which was designed to work in visible frequency range. Their design has three bands in this range. Liu *et al.* [47] designed an aluminum based metamaterial absorber. Their absorber designed to operate in the ultraviolet frequency range. In addition, some of the studies in the literature focused on the multilayered absorber in order to absorb solar energy. Liang *et al.* [48] presented a metamaterial solar energy absorber which has a pyramidal shape. They utilized vertically cascaded metal-dielectric layers in order to obtain perfect absorption in the solar range. Moreover, Wu *et al.* [49] investigated the absorption effects in grating-based devices. Their structure is designed to operate in

infrared frequencies. They also utilized vertically cascaded metal-dielectric grating for obtaining multiband absorption.

In this chapter, a new metamaterial absorber design which is composed of a metallic ground plane, a dielectric spacer layer and metallic resonators is introduced to be used in the thermo-photovoltaic applications. The characterization of the resonators and analysis of the geometric parameters of the structure are carried out to understand the absorption mechanism of the proposed metamaterial absorber. According to the results, multiband (one being wide) perfect absorption is achieved in the visible realm.

## **6.2. Design and simulation**

The geometry of the design is presented in Figure 6-1. This absorber is composed of three layers; the continuous metallic bottom layer with the thickness “h”, dielectric separator with the thickness “d” and the metallic resonator at the top of the structure with the thickness “e”. The resonator itself has different geometric configurations which can be expressed as corner patches, central patch and strips. The geometric dimensions and the letters denoted to these dimensions are given in Figure 6-1b while the values associated with each parameter are presented in Table 6-1. The unit cell periodicity of the proposed design is given by “p”. Each of the resonator pairs shown in Figure 6-1 are responsible from the resonance at different frequencies. The contribution of these resonators to the absorption spectrum will be discussed in the next section. The metallic parts of the structure are aluminum (Al) where the silicon dioxide (SiO<sub>2</sub>) is used as dielectric material. Aluminum has been chosen because of its relatively lower material cost and lower skin depth (especially when compared with silver and gold) which might reduce the total cost in practical applications. Frequency dependent complex dielectric parameters of Al and SiO<sub>2</sub> are taken from Palik’s book [71].

In order to characterize the unit cell and understand the absorption mechanism of the design, some simulations are performed. Optimum parameters for the proposed metamaterial absorber are obtained by varying and simulating all the mentioned parameters in Table 1 simultaneously. These simulations are carried out by a commercial simulation software which uses finite integration technique to solve the Maxwell’s equations. Boundary conditions for the simulations are chosen to be

periodic in  $x$  and  $y$  directions and open boundaries are used along  $z$ -direction. In the numerical analysis, the electric and magnetic field components of the incident plane wave are assumed to be polarized in  $x$  and  $y$ -direction, respectively. The direction of propagation is along the  $z$ -direction, as shown in Figure 6-1b.

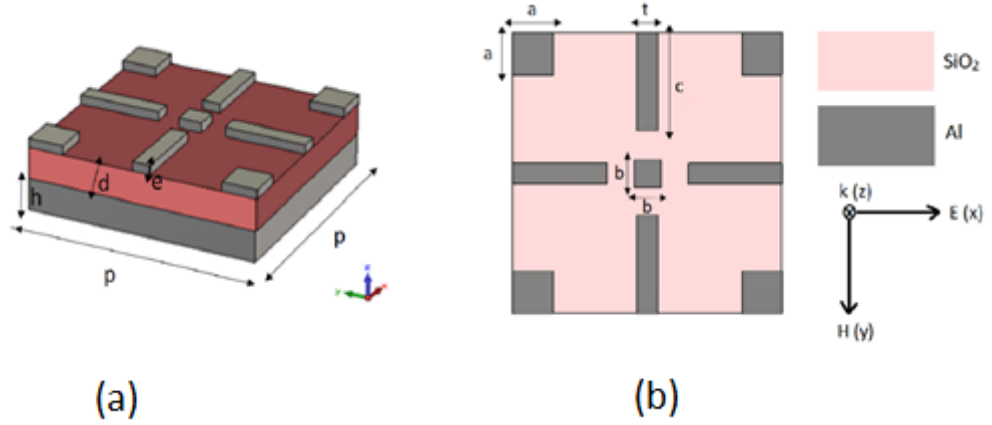


Figure 6-1. Geometry of the unit cell of the proposed metamaterial absorber structure. a) Perspective view b) Front view.

Table 6-1. Values associated with each parameter in nanometer.

Parameter	p	a	c	b	H	d	e	t
Value (nm)	400	40	140	60	50	50	15	30

Solar radiation covers the range between 100 THz and 1000 THz, from near infrared to ultraviolet region. Because of the higher solar irradiance in the visible frequency range, simulations are mainly carried out in this range. However the reflectance and absorption spectra of the proposed absorber in the infrared and ultraviolet regions are also presented in the following sections.

As the bottom continuous Al metallic plate has the thickness greater than the skin depth, it acts like an optical mirror and prevents the transmissions to pass through the structure. Under this circumstances, transmission becomes negligible (approximately zero).

Optical absorption behavior of the proposed structure can be calculated by using Equation (6.1) where the frequency dependent parameters  $A(\omega)$ ,  $R(\omega)$ , and  $T(\omega)$  represents the absorption reflectance and transmittance, in order. As it is mentioned

before,  $T(\omega)$  can be neglected because of the optical preventative characteristics of the bottom Al plate. Therefore, Equation 6.1 reduces to Equation 6.2. Using the obtained scattering parameters ( $S_{11}$  and  $S_{21}$ ) from the simulations, the absorption can be calculated and plotted via Equation 6.3.

$$A(\omega) = 1 - R(\omega) - T(\omega) \quad (6.1)$$

$$A(\omega) = 1 - R(\omega) \quad (6.2)$$

$$A(\omega) = 1 - |S_{11}|^2 \quad (6.3)$$

### 6.3. Results and discussion

The introduced metamaterial absorber has three absorption resonances in the interested frequency range (visible region due to the high solar radiation level). The first absorption resonance occurred at 445.85 THz while the second and the third resonances take place at 624 THz and 658.3 THz, respectively. Note that, because the second and the third resonances are very close to each other, they formed a wide-band absorption with the bandwidth of 34.3 nm where the absorption rate is more than 99.4 % in this wide-band region. The absorption levels are 98.2 %, 99.8 % and 99.9 % for the first, second, and third resonances, correspondingly. The absorption and reflectance spectra for the visible region are given in Figure 6-2. The inside graphic represents the zoomed form of the absorption bands for the second and the third resonances.

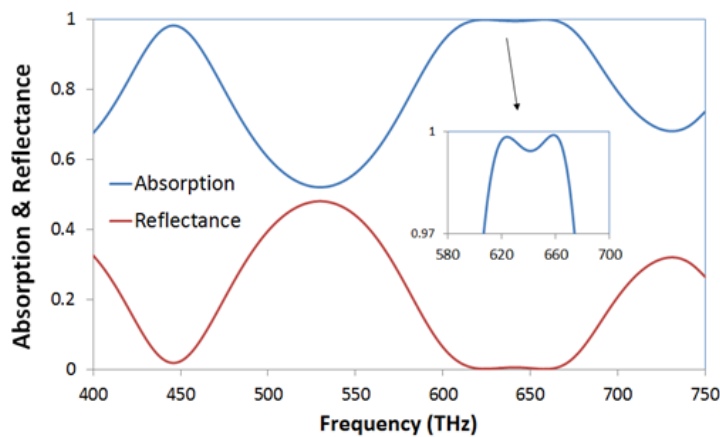


Figure 6-2. The reflectance and absorption spectra of the structure in the visible frequency region.

In addition to visible frequency range, the absorption behavior of the metamaterial absorber is investigated in the ultraviolet and infrared frequency ranges. The obtained results for these ranges are given in Figure 6-3. Figure 6-3a represents the spectra for infrared region while Figure 6-3b displays the spectra for ultraviolet region. For infrared region, the absorption peak is obtained at 201.4 THz with the percentage of 81.4%. This resonance can further be improved by altering the geometric dimensions of the structure as it is performed for the visible range in the following sections. For the ultraviolet region, the absorber does not provide any significant resonance peak. However, at the beginning of this region, the magnitude of the absorption is around 78 % and it is decreasing to 40% at the end of this region. Therefore, it can be concluded that, the proposed absorber not only absorbs the radiation in the visible range, but also absorbs the radiation almost in all solar spectrum with different magnitudes.

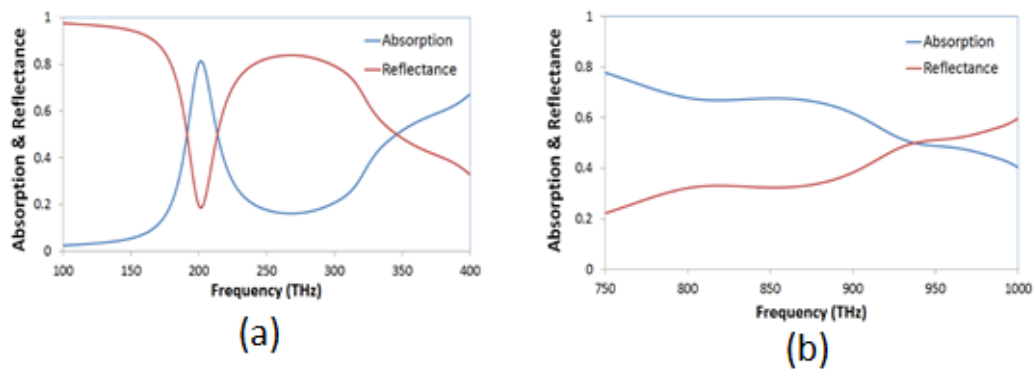


Figure 6-3. The reflectance and absorption spectra of the structure a) in infrared frequency region b) in ultraviolet frequency region.

In this part, the resonators of the structure have been divided into two groups in order to perform the characterization of these elements; first group consists of the square patches at the corner and the second group composed of the combination of the strips and the square patch at the center of the unit cell. The individual responses of the mentioned groups are given in Figure 6-4 (the first group is shown in Figure 6-4a while the second group is in Figure 6-4b). First group is responsible from the dual-band absorption along with perfect absorption in the visible regime caused by the interaction between the resonators and the bottom metallic plate (Figure 6-4a). Although, the resonators in the second group also provide two absorption bands along (one being in the infrared and the other in visible range). The absorption rate provided by this group is nearly 80% (Figure 6-4b) for both of the resonances. However, when all of the

resonators are combined, the absorption strength increases because of the coupling and plasmonic effects of the resonances. Here, the central square patch is added to the second group because it enhances the magnitude of the resonance provided by the strips in the visible range. Moreover, it also causes the shift in resonance wavelength as can be seen in Figure 6-4c. Magnified resonance peaks can be seen in the inset of the Figure 6-4c. The resonance wavelength takes place at 599.5 THz with the strength of 0.73, when only strips are used. However, when the strips and central patch are combined the, the wavelength shifts to 603.7 THz and the strength increases to 0.78.

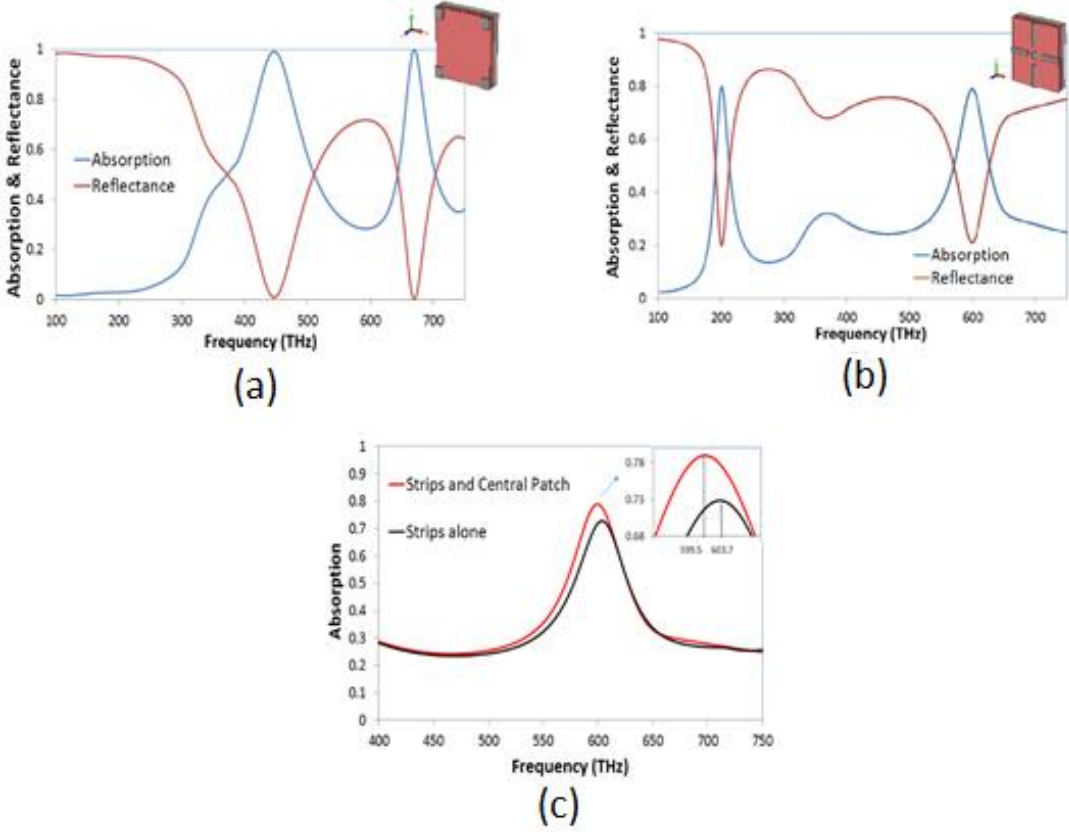


Figure 6-4. The contribution of the resonators to the absorption spectrum. a) Represents the contribution of the patches at the corners and b) represents the contribution of the strips and the patch at the central of the structure. c) Comparison of the effects of the central patch on the absorption spectrum.

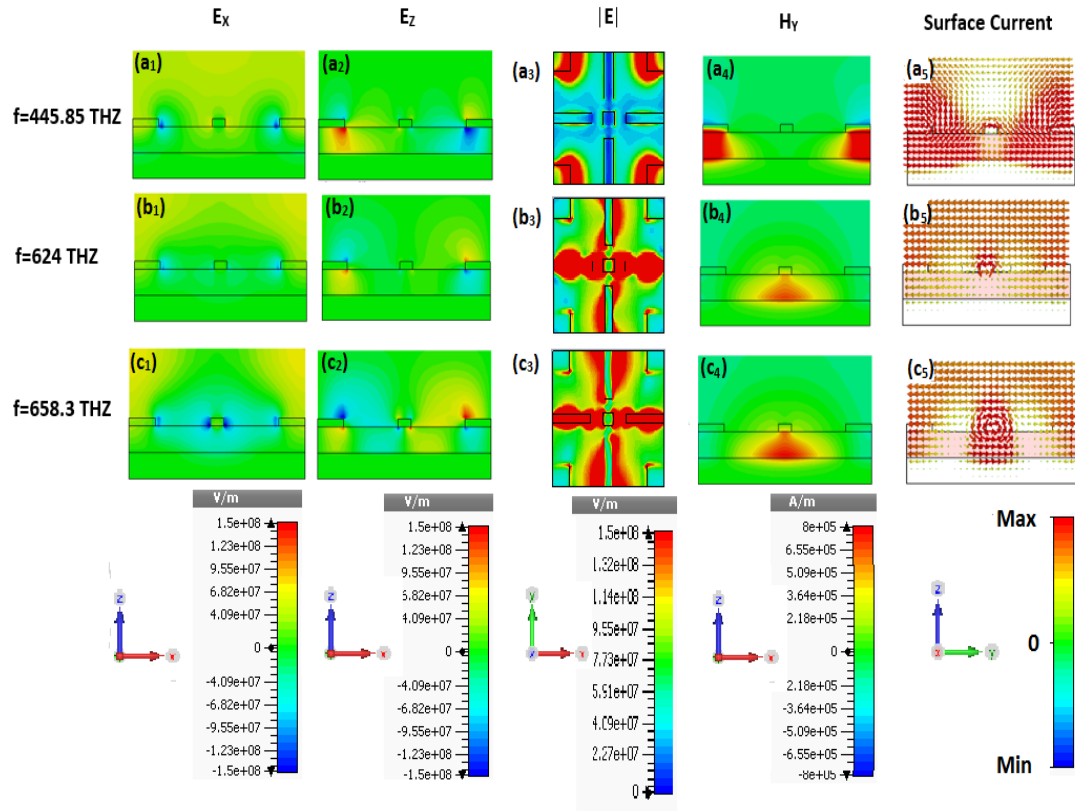


Figure 6-5. (a<sub>1</sub>)- (c<sub>1</sub>) X-component of the electric field distributions. (a<sub>2</sub>)- (c<sub>2</sub>), Z-component of the electric field distributions. (a<sub>3</sub>)- (c<sub>3</sub>), Magnitude of the electric field distributions on the dielectric layer. (a<sub>4</sub>)- (c<sub>4</sub>) Y-component of the magnetic field distributions. (a<sub>5</sub>)- (c<sub>5</sub>) Surface current distributions. All the Figures are given for the first second and third resonances respectively. The scales of the corresponding distributions are given at the bottom of each group.

In the next step, the dependence of the absorption peaks to the geometric parameters are examined. Keeping the other parameters fixed, dielectric layer thickness (parameter d), resonator thickness (parameter e), strip length (parameter c), and strip width (parameter t) are altered for characterization and better understanding the mechanism of the absorber. In order to obtain the optimum parameters for the proposed metamaterial absorber, all the mentioned parameters are changed and simulated simultaneously. Results for the mentioned parametric studies are given in Figure 6-6. Note that the red curves in all plots indicate the desired results with respect to the absorption rate and those parameters can selected as the optimum parameters for the perfect absorption.

First, the thickness of the dielectric layer is examined. The effect of the dielectric thickness to the resonant frequency and absorption rate is observed by altering parameter d. the response is given in Figure 6-6a. The optimum thickness for the dielectric layer is found to be  $d=50$  nm. The dielectric thickness mainly helps the coupling between the electric resonance occurred on the metallic resonators with the bottom metallic layer. Thus, this coupling creates a magnetic response and finally makes the effective impedance of the absorber to be equal to the impedance of the free-space (impedance matching). This situation was also verified by the electric and magnetic distributions given in Figure 6-5. Although, the thickness of the dielectric separation is enough to create a magnetic response for the  $d$  smaller and greater than 50 nm, it does not provide the impedance matching for some thicknesses. Thus the selection of the dielectric thickness for such structures is very important to have perfect absorption.

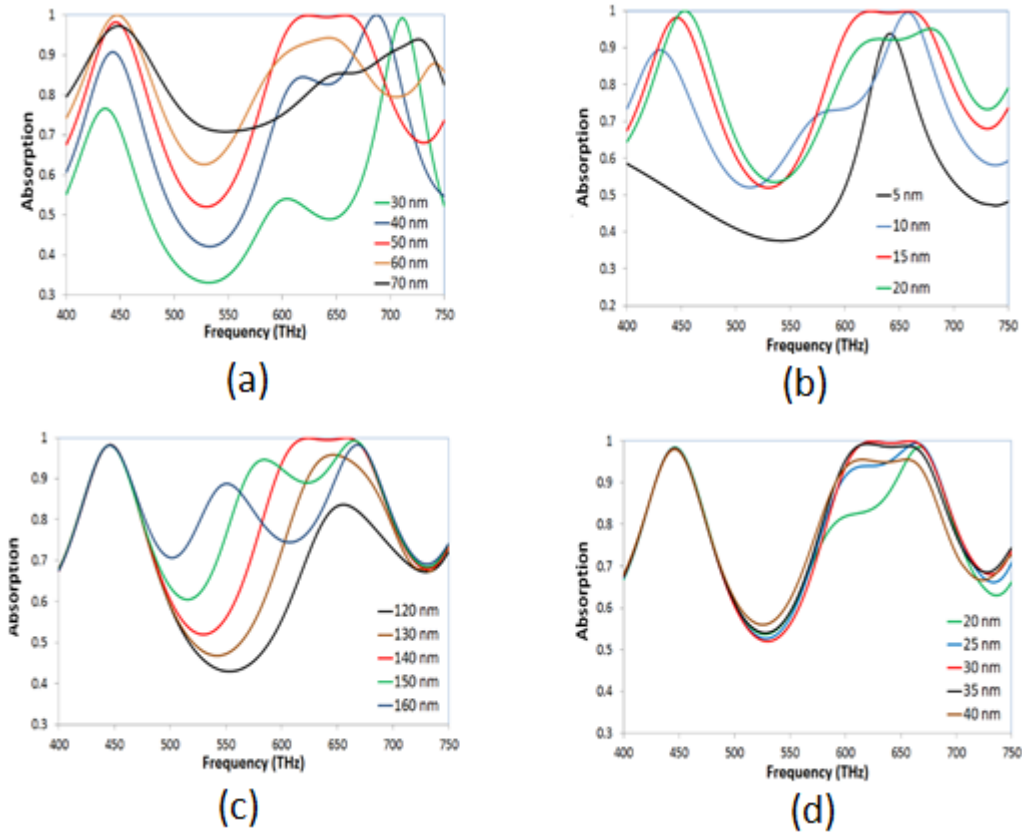


Figure 6-6. Variation of absorption spectra for a) dielectric layer thickness (parameter d), b) resonator thickness, (parameter e), c) strip length (parameter c), d) strip width (parameter t).

Resonator thickness ( $e$ ) is one of the other important parameter that determines the absorption strength/rate and resonant frequency. The variation can be seen in Figure 6-6b. As it is obvious from here, the structure gives only one resonance at around 650 THz when thin resonators are used. However, when the thicknesses are increased, the magnitude of the absorption is enhanced at three different frequency locations of the visible frequency region for different thicknesses. When “ $e$ ” is adjusted to the small values (like 5 nm), the thickness of the resonator becomes not enough to generate the perfect absorber response caused by the metallic resonators. However, when the thickness is higher than a certain value (such as 20 nm), the structure reflects some part of the incident wave. If the thickness continued to be increased, the metallic parts starts to behave like an optical mirror (results not shown here). Therefore, for the proposed structure,  $e=15$  nm can be selected for the perfect absorption which has a good harmony between the transmitted and reflected waves (almost zero reflection and transmission) and also creates the desired electric and magnetic responses.

As can be seen from Figure 6-6c, the resonances are also dependent on the length of the strips (parameter  $c$ ). Although the first resonance at 445.85 THz doesn't affected from the changes at parameter  $c$ , the second and the third resonances are strongly dependent on this parameter. This is expected because the electric and magnetic responses depend on the resonators of the first group (not the strips: second group) at the first resonance as can be seen in Figure 6-5a<sub>1</sub>-a<sub>4</sub>. As discussed in the previous section, the third resonance is contributed by the square patches at the corner when all the resonators are qualified separately. However when all the resonators combined in a unit cell, the individual resonators or the groups of resonators can affect each other. Therefore, in Figure 6-6c, it can be seen that the third resonance is affected from the strip length. This is mainly because of the interactions between the resonator elements. Therefore, by altering the length, the ideal case for the perfect absorption can be found when the length is adjusted to be  $c=140$ nm.

In addition, the absorption spectra for the variation of the strip width is also presented. As it is obvious from Figure 6-6d, the variation of this parameter (parameter  $t$ ), does not affect the first and the third resonances (except  $t=40$ nm). As discussed before, the first and the third resonances are mainly caused from the resonators of the first group (square patches at the corner) while the second resonance is caused by the second

group resonators (strips and the central patch). Therefore, the variation of the geometric dimensions of the strips mostly reduces the second resonance.

As discussed in the previous sections, perfect absorption takes place when the effective impedance of the absorber,  $z(w)$ , matches with the impedance of the free space. This condition ensures the zero reflection and transmission of the incident wave.  $z(w)$  is strongly related with the effective permeability,  $\mu(w)$ , and effective permittivity,  $\varepsilon(w)$ , of the absorber ( $z(w) = \sqrt{\mu(w)/\varepsilon(w)}$ ). Thus, impedance matching occurs when the electric and magnetic resonances exist simultaneously. The calculated normalized impedance of the proposed absorber is given in Figure 6-7. The real part,  $\text{Re}(z)$ , and imaginary part,  $\text{Im}(z)$ , of the impedance at resonance wavelength are given in the inset of Figure 6-7. In order to fulfil the matching condition, the normalized impedance should satisfy the conditions of: the  $\text{Re}(z) \approx 1$  and  $\text{Im}(z) \approx 0$ . At 624 THz and 658.3 THz, which have more than 99% absorption rate, the conditions for  $\text{Re}(z)$  and  $\text{Im}(z)$  are satisfied. For the first resonance which has relatively lower absorption strength with respect to the other resonances,  $\text{Re}(z) = 1.24$  which is a little bit higher than the matching condition and  $\text{Im}(z) = -0.19$  which is a little bit lower than the matching condition. This is mainly because of the relatively higher reflection rate (98.2 % absorption rate) occurred at this resonance.

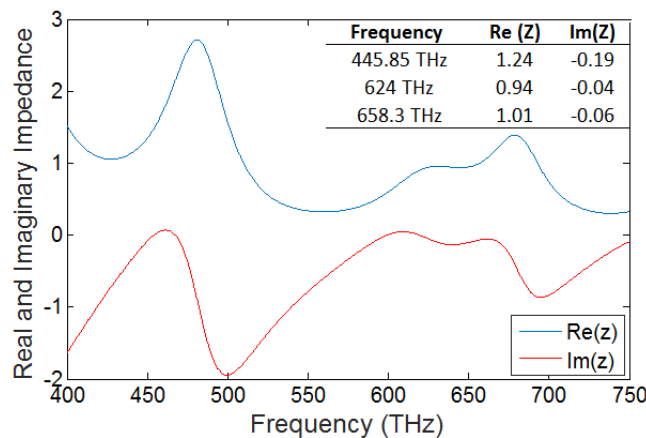


Figure 6-7. Normalized effective impedance of the absorber. The inner table shows the real and imaginary parts of the impedance at resonant frequencies.

For the next exploration, under transverse electromagnetic (TEM) polarization mode, the polarization angle  $\theta$  is changed in order to visualize the polarization dependency

of the absorber in the visible frequency range. The results are given in Figure 6-8. As Figure 6-8 represents, the absorber is completely polarization insensitive under TEM mode due to its four folded symmetric design.

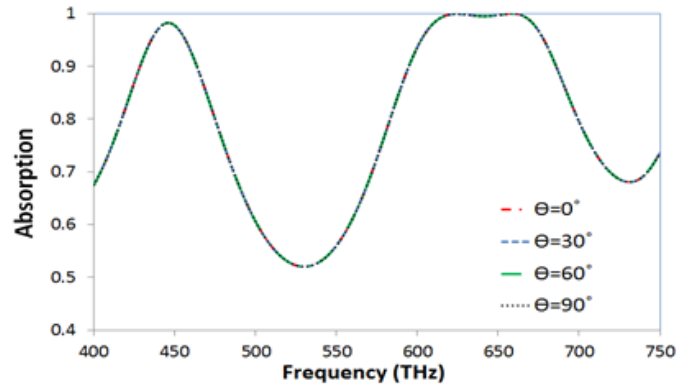


Figure 6-8. The absorption spectra under for various polarization angles.

#### 6.4. Theoretical Verification

In this section, verification of the numerical result (given in the previous sections) for the visible frequency range, is done by using interference theory model. As the main operation frequency range is defined to be visible range, the theoretical calculation is carried out only in this range. The theoretical and numerical results are compared in Figure 6-9. According to Figure 6-9, it can be commented on that, the numerical and theoretical results are in a good agreement.

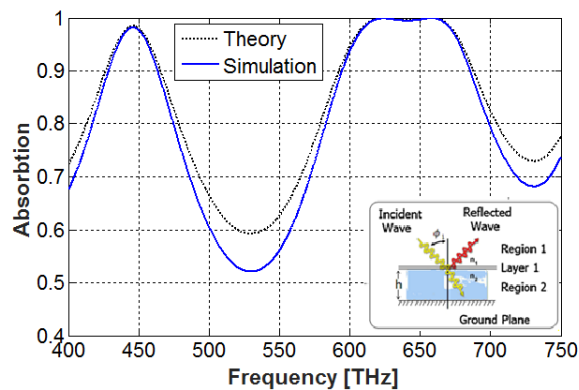


Figure 6-9. Comparison of the Theoretical and simulation results for absorption.

## **6.5. Conclusion**

In conclusion, in this chapter, a metamaterial absorber design formed by the combination of the three effective layers are introduced. Unlike the most of the studies based on multiple layers presented in the literature, the combination of only three layers are used to obtain the multiple and wide-band perfect absorption. The characterization of the multiband resonances is carried out by identifying the responses of each resonators and discovering the origins by using the electric and magnetic field distributions at resonant frequencies. The investigation of the dependency of the geometric parameters on the metamaterial absorber is also presented. As a conclusion, the introduced polarization insensitive, multiband metamaterial absorber can be used for the harvesting of solar energy, sensing applications, absorption of solar radiation, detection and imaging in the solar spectrum.

## CHAPTER 7

### MULTIBAND METAMATERIAL ABSORBER FOR PHOTOVOLTAIC APPLICATIONS

#### 7.1. Introduction

The perfectly absorptivity property of the metamaterials can be utilized in the photovoltaic cell to convert the solar energy directly into the electric energy. For photovoltaic response, generally the active material is needed to absorb and convert the absorbed energy into the useful forms. Active material is a semiconducting material where the absorbed energy is transferred into the electron hole pairs. These pairs are then separated to the electrodes and finally the energy can be taken as the form of electric current from these electrodes.

The losses occurred within or out of the solar cell reduce their performance and cause the inefficiently converting the solar energy into the usable forms. These losses include the optical losses, and thermal losses. This condition leads to the generation of heat which is a side effect for photovoltaic application.

Another disadvantage of current solar cells is the thickness of the active material. As the depth of this beneficial material increases, the previously created electron hole pairs recombined together. This result with an inefficient conversion of the solar energy. As the metamaterials are compact structures and they are small in dimension, they can help preventing of these losses occurred within the cell. Moreover, the plasmonics responses discussed above, can cause the creation of the new resonance and therefore the absorption behaviors.

In this chapter, a new metamaterial absorber design is introduced for photovoltaic applications of metamaterial absorbers.

#### 7.2. Design and Simulation

The geometric model of the unit cell as well as the dimension parameters and the electromagnetic field polarization are is given in Figure 7-1. Two metallic layers and an ultrathin semiconductor plate sandwiched between to metallic layers are employed for this design. The four isosceles triangle resonators at the top are embedded in the

semiconductor layer so that they can easily support surface plasmon polaritons. The materials which were utilized to form the proposed metamaterial absorber are silicon (Si) for semiconductor, and silver (Ag) for the metallization. Silicon is chosen as it is low costed and abundant in the nature and silver is selected as it has a good conductivity in these frequencies and support surface plasmon polaritons [94]. Moreover Ag can also be used as the front contact for the photovoltaic applications. The parameters shown at Figure 7-1,  $a$ ,  $d$ ,  $p$ ,  $h$  and  $t$  represented the length of the isosceles triangular resonators, the thickness of the Si layer, the period of the unit cell, the thickness of Ag plate, and the thickness of the isosceles triangular resonators correspondingly. The optimum values for these parameters for higher absorption rates are:  $a=250$  nm  $p=590$  nm  $h=50$  nm  $t=10$  nm  $d=10$  nm.

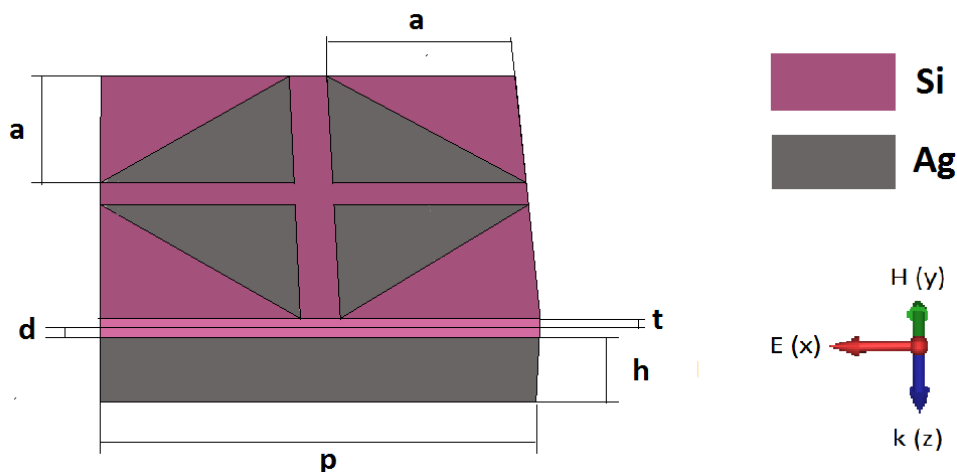


Figure 7-1. Proposed metamaterial absorber design.

### 7.3. Results and Discussion

The outputs of the numerical simulation software for absorption and reflectance are represented in Figure 7-2. The given frequency ranges include the visible and the ultraviolet regions. These results indicate that the introduced absorber model has a dual band absorption response only in the visible regime. Therefore, throughout this chapter, the metamaterial absorber will be analyzed only in the visible frequency regime.

In general, the photovoltaic response of a photovoltaic cell is related with the absorption rate occurred in its active material which generates the electron hole pairs.

Here, the active material is amorphous silicon. Under these circumstances, the absorption rate in Si is important rather than the absorption in Ag. Thus, unlike the other chapters, the selection criteria for this chapter are the total absorption rates in a-Si material over the simulated frequency range.

The two absorptions peaks are located at 439.95 THz and 508.35 THz with the rates of 99.69% and 96.25% in order. Additionally, between 420.5 THz and 541.7 THz, the absorption rates are higher than 85% which corresponds for more than 121 THz frequency range.

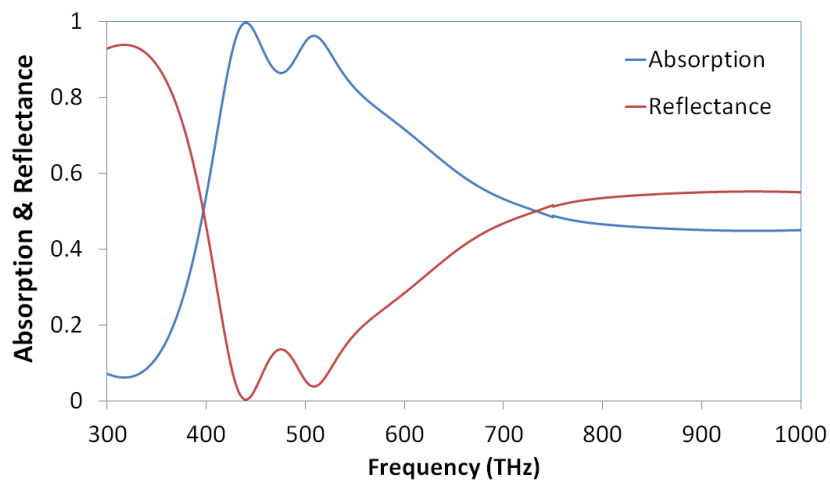


Figure 7-2. Absorption and reflectance response of the proposed absorber. The values taken for the parameters are:  $a=250$  nm,  $d=10$  nm,  $h=50$  nm,  $t=10$  nm and  $p=590$  nm.

The underlying resonance mechanism can be understand explained by examining the field distributions which are demonstrated in Figure 7-3. At 439.95 THz, the electric field is mainly confined at the corners of the structure and between the triangular resonators in *y-direction*. These places are the main source of the electric effect for this resonance. The differences between the resonances at 439.95 THz and 508.35 THz is visible when Figure 7-3a and Figure 7-3b are compared. Unlike to the electric effect at first resonance, at 508.35 THz electric effect is localized in *x-direction*. In addition to the compressed fields between the isosceles triangles, electric effects are also generated at the edges of the triangular resonators.

The magnetic effect at 439.95 THz is initiated by the isosceles triangles. This is obvious from Figure 7-3c. However, the magnetic effects at the regions near both sides

of the structure between the triangular resonators in the *x-direction*, are almost non-existing. This exhibits a very big contrast when the strong magnetic effect just near that regions are considered. This type of concentration and the localization of the magnetic response strongly couples with the basement Ag plate so that the reverse directional currents between these two mentioned regions occurs which is demonstrated in Figure 7-3e. Note that Figure 7-3a, Figure 7-3b, Figure 7-3c and Figure 7-3d are given on *x- y* while Figure 7-3e and Figure 7-3f are given on *y-z* plane. Unlike the resonance at  $f=439.95$  THz, at  $f=508.35$  THz the magnetic density is confined between the isosceles in *x-direction*. In addition, the localization also took place at the edges of these triangular elements similar to the electric effect occurred at this frequency. This strong concentration produces the rotating current loop at the middle portion of the structure (Figure 7-3f).

For both of the resonances, magnetic effect together with the electric effect, provide the ideal condition for the matching of the impedance and at the end, this condition results with the perfect absorption.

In order to reveal the functional parameters for absorption, the parametric sweep is carried out and the variation spectra are shown in Figure 7-4. For all the plots, the absorption marked with red color indicates the chosen and the best option in terms of the absorption rate in a-Si. As mentioned before, the absorption rate of the individual materials are important for photo-voltaic applications. For this design the photo active material is Si. Therefore, the absorption rate in a-Si is decisive rather than the total absorption rate and due to this reason, the absorbance spectrum of amorphous silicon is also given in the inset of all the graphical representations in Figure 7-4.

The variation of the total absorption spectra when parameter “p” is altered are given in Figure 7-4a. Here, total absorption includes the absorption in both a-Si and absorption in Ag. as all the other dimensions are fixed and they are all independent from the variation of “p”, the enhancement or the reduction of this value only changes the used material amount and the gap between the isosceles triangles. The variation mainly and significantly affected the resonance at 508.35 THz while the resonance at 439.95 THz is not affected much. This situation can be explained by the field distributions given in Figure 7-3. The peak point at 508.35 THz is mainly created by the interaction of the

isosceles triangles between each other. As explained before, this condition caused the electric and magnetic responses occurred at the position between the isosceles triangles which is visible from Figure 7-4b and Figure 7-4d. The surface current distribution which demonstrate the rotating current loop at the middle portion of the structure also proves this condition. Increasing the gap causes the changes of the electrical character (capacitive effect occurred between the triangles) and so that it enhances the absorption rates and changes the resonant frequency [80]. Although the enhancement of the absorption rates of the second resonance, the absorption spectrum becomes narrower. In order to clarify this circumstances, total absorption rates in a-Si layer is also figured out and represented in Table 7-1. Notice that the optimum parameters are given in bold in Table 7-1. It is clear that the highest absorption rates are observed at  $p=590$  nm. Hence the “p” is defined as 590 nm.

The depth of a-Si (parameter “d”) in other words the separation distance between two Ag plates, is one of the critical variable. Figure 7-4b indicates the variation of the spectrum in the case that “d” is altered with the steps of 5 nm. When the basement Ag plane and the isosceles triangular Ag layers are close enough to each other, this cause the coupling between these two silver plates. When these layers are close enough to each other, this sufficient distance induces the magnetic resonances as realized here. Moreover, the calculation of the total absorption rate of amorphous silicon layer suggest that this material has the highest rate of 48.0% when “d” is in its optimum value ( $d=10$  nm).

The critical role of the properly selected dimensions of the isosceles triangular resonator (parameter “a”) are analyzed in Figure 7-4c. The explanations for “a” goes similar to the parameter “p”. The alteration of both of these parameters varies the gap between the isosceles triangular resonators in the same way. The amount of the total absorption rates in a-Si material are also given in Table 7-1. Note that the absorption rates of the a-Si is same when  $a=250$  nm and  $a=260$  nm. However when  $a=260$  is selected the absorption rate of the Ag increases by 7.7% when compared to  $a=250$  nm. Therefore  $a=250$  is chosen as the optimum parameter. Because, enhancement in the absorption rate of the Ag causes some side effect like heat generation [95].

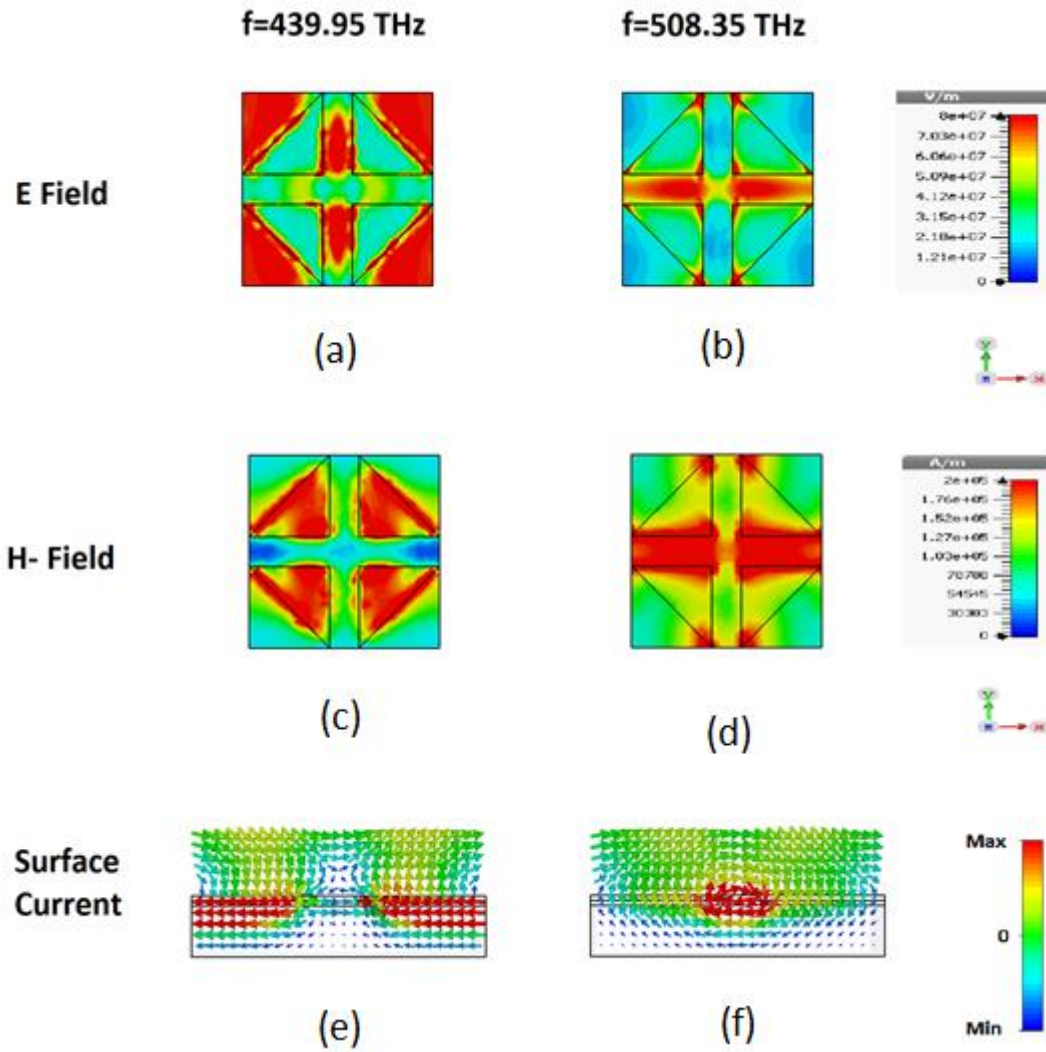


Figure 7-3. Distributions at resonance frequencies. (a) electric field at 439.95 THz, (b) electric field at 508.35 THz, (c) magnetic field at 439.95 THz (d) magnetic field at 508.35 THz, (e) surface current at 439.95 THz (f) surface current at 508.35 THz. Electric and magnetic field distributions are given on x-y plane where surface current distributions are given on y-z plane at  $x=295$  nm.

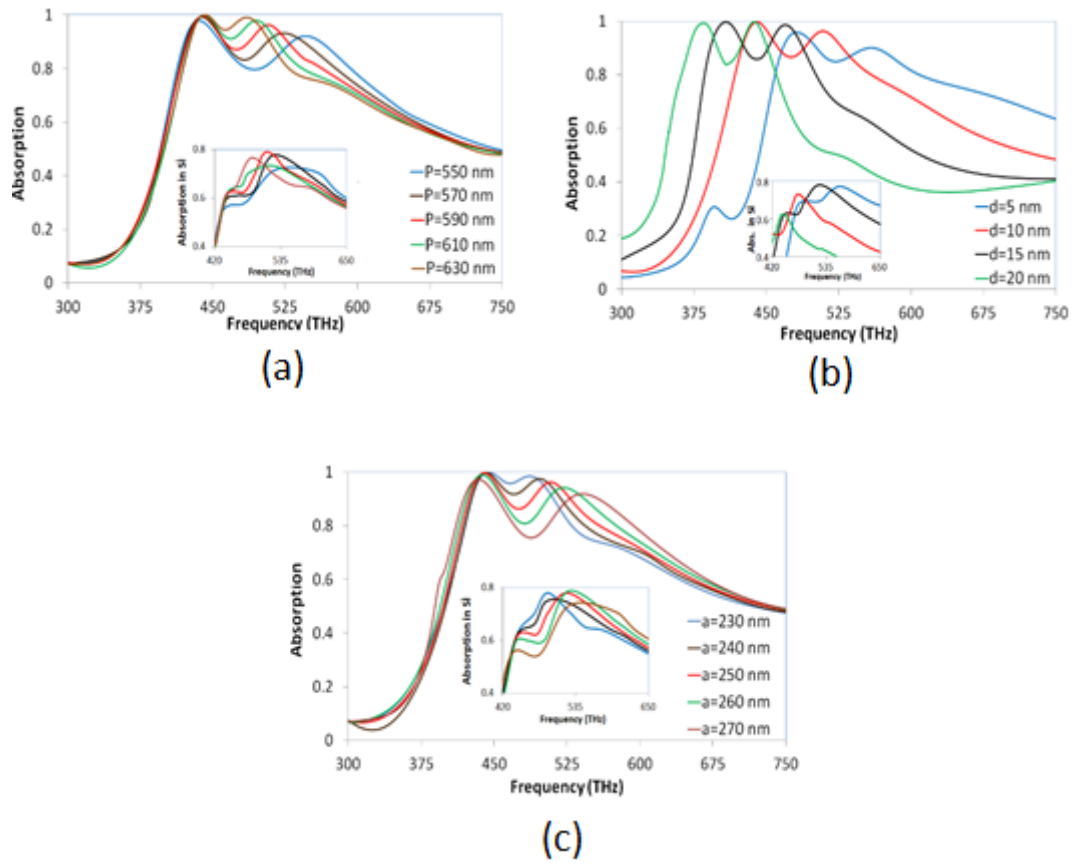


Figure 7-4. The dependence of the absorption spectra on the geometric variables. (a) Dependence on the unit cell period. (b) Dependence on the semiconductor height. (c) Dependence on the side length of the isosceles triangular resonators. The variation of the absorption spectra of amorphous silicon are represented in the inset of each of the figures.

Table 7-1. Total absorption rates of a-Si over the whole spectrum for various geometric dimensions.

Parameter "p"		Parameter "a"		Parameter "d"	
Value (nm)	Absorption rate (%)	Value (nm)	Absorption rate (%)	Value (nm)	Absorption rate (%)
550	47.6	230	46.8	-----	-----
570	47.7	240	47.1	5	47.7
<b>590</b>	<b>48.0</b>	<b>250</b>	<b>48.0</b>	<b>10</b>	<b>48.0</b>
610	47.1	260	48.0	15	42.3
630	47.0	270	47.4	20	36.6

The simplicity and symmetry of the model causes a significant advantage especially for the polarization independent property of the design. As demonstrated in Figure 7-

5, this design serves a polarization insensitive behavior under normal incidence case of the radiation.

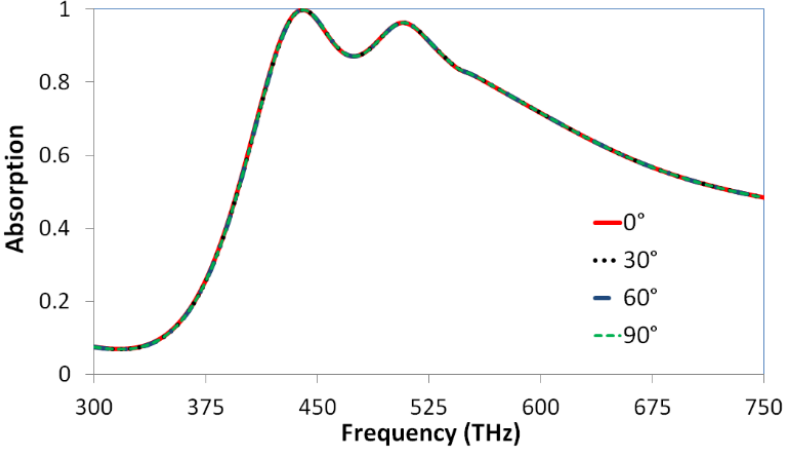


Figure 7-5. Dependence of the absorption on polarization angle under normal incidence mode of the electromagnetic radiation.

Figure 7-6 virtualize the response of the design under the various incident angles for TE and TM cases. Both For TE case (Figure 7-6a) and TM case (Figure 7-6b) the consistency in the absorption is achieved for a wide incident angle ranges. In fact, TM mode has a better and a wide absorption as the angles are increase up to 60°. This is mainly due to the influencing of the magnetic effect of the structure with the external magnetic field [96].

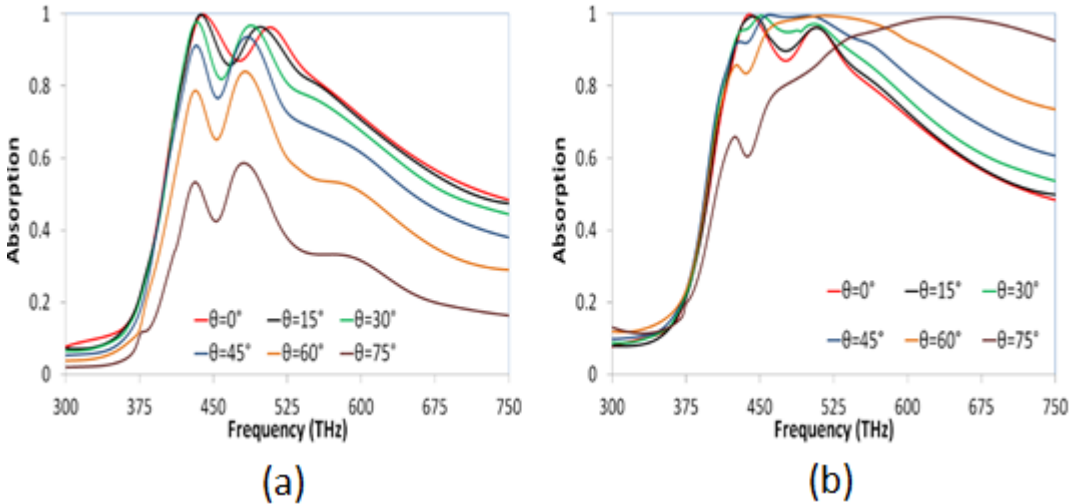


Figure7-6. Absorption response under various incident angles (a) TE mode (b) TM mode.

As the mentioned designed is proposed for photovoltaic application, the direct effect of the sun will heat the structure. Furthermore, not only the sun, environment conditions may cause the working of the structure under low temperatures. Therefore, in addition to the results given above the thermal characterization of the introduced absorber is also studied between 300 THz and 750 THz with temperatures varying between 0° C and 60 ° C. the thermal and frequency dependent optical parameters for Ag is taken from [97] and a-Si is taken from [98-99]. The optical properties these materials are not much varying under different temperatures. As it is clear from Figure 7-7 in which the dependency on temperature is presented, the absorptivity mechanism of the absorber is not much effected remained stable. Under this circumstances, the mention structure is suitable for the photovoltaic applications.

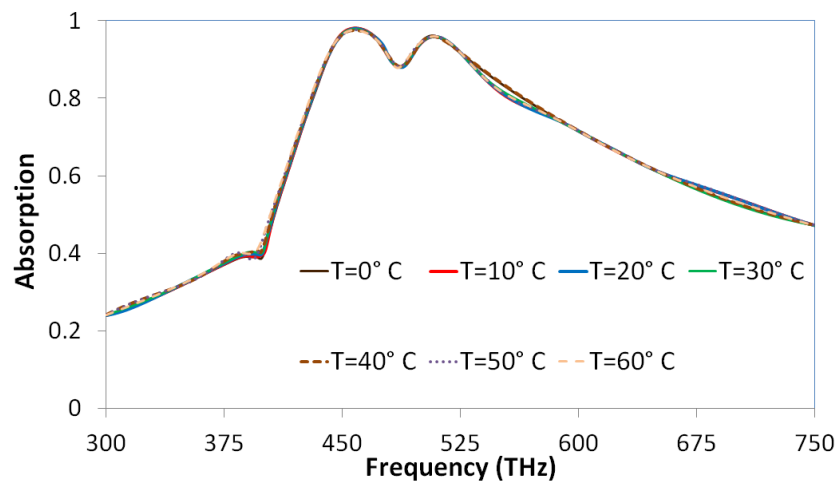


Figure7-7. Thermal characterization of the absorber between 0° C and 60 ° C.

#### 7.4. Conclusion

In this part a dual band metamaterial absorber is designed for photovoltaic application in which the geometric dimensions, polarization and thermal, characterizations are discussed. The photovoltaic response is mainly provided by the photo active material (a-Si). The increased absorption levels of the Ag is an adverse effect which reduces the photovoltaic response of the design. Moreover, the enhancement of the absorption band for utilizing the wide solar spectrum is essential for an enhanced photovoltaic effect.

## CHAPTER 8

### APPLICATIONS OF THE ABSORPTION ENHANCEMENT TECHNIQUES

#### 8.1. Introduction

Recently there are ongoing trends about improving the efficiencies of the metamaterial absorbers and the solar cells. These techniques include using graphene in the structure of absorber, changing the geometric structure of the back metallic plate, and utilizing Indium Tin Oxide (ITO) in the design. These techniques open a road for the new interactions which causes the generation of the plasmonics. Hence, the newly occurred plasmonics contribute to improve the absorption rates of the design. In addition, they may act as an interference film so that the reflected radiation can be utilized in the absorber. However, the absorption rates and the performance of the absorber are extremely rely on the geometric structure, as mentioned in the previous chapters. Thus, for some of the designs these polaritons may not be generated to form the enhanced absorption if the geometric dimensions are not set properly.

In this chapter, some improvement techniques will be introduced, explained, and applied to the design analyzed in the previous chapter.

#### 8.2. Hole at The Back Metallic Plate

For this section the shape of the back metallic plane is reformed by opening holes in different geometrical shapes. In this case the newly formed metallic Ag hole shaped resonator, supports the plasmon polariton at these frequencies. Thus, this method is capable to enhance and improve the absorption rates. As the back Ag plate acts as an optical mirror, reshaping it may increase the transmission which results with the reduction of the overall absorption rate. Therefore, in this study both the reflection and the transmission are also included into the calculations.

Three different geometrical shapes are designed and applied to the back metallic plate. The illustration of the reshaped silver plates are given in Figure 8-1. The first one (Figure 8-1a) is the square shape hole which takes place at the middle of the plate. The

second and the third ones are the cross shape and the isosceles triangular shaped holes and are represented in the Figure 8-1b and Figure 8-1c respectively.

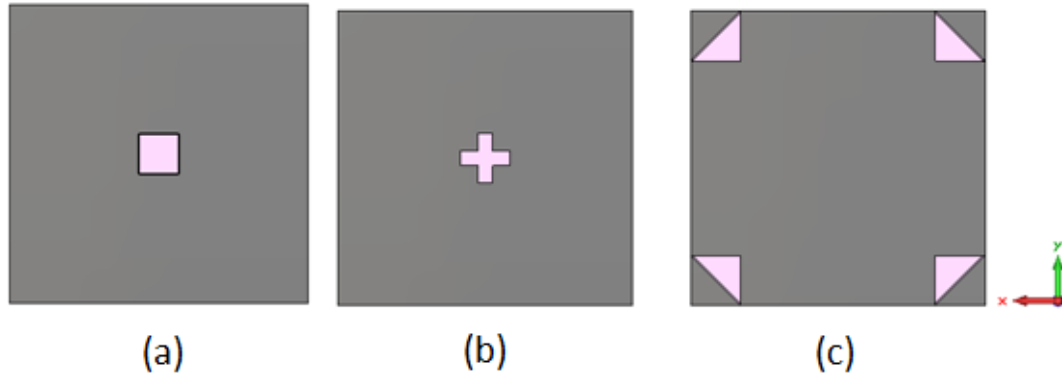


Figure 8-1. Illustration of the reshaped back silver plate. (a) Square shaped hole, (b) cross shaped hole, (c) triangular hole.

Although the absorption reaches to more than 96% at the peak points, it is hard to predict the absorption performance of the design due to the variations (enhanced levels for some regions and decreased levels for other regions for one parameter) of the absorption levels over the solar spectrum. Therefore, the total absorption rates of the design are calculated over the studied frequency spectrum. These rates represent the ratio of the absorbed energy to the total energy provided by the solar energy spectrum.

For each of the design, the total absorption rates of the absorber are analyzed for various dimensions of these shapes. The analyses and the calculations are carried out over the whole spectrum between 300 THz and 1000 THz.

For the square shaped hole, the absorption rates when the side lengths of the square are altered are calculated and given in Table 8-1. Here, the zero side length represents the condition which there is no hole on the silver plate and this value is accepted as the reference value. The magnitude of the absorption increases until the dimension of the square hole equals to 120 nm. The absorption rate reaches to 57.5% which is the maximum absorption level obtained for this geometric shape. The enhancement in the absorption was calculated as 3.2% with respect to the reference value. When the dimensions was increased above 120 nm, the rates start to become lower as can be seen from Table 8.1.

Table 8-1. The absorption rates over whole spectrum for various square hole dimensions

Side length of square (nm)	0	20	40	60	80	100	120	140	160	180	200
Absorption Rate (%)	55.7	55.7	55.8	56.3	56.8	57.1	57.5	57.4	57.1	56.7	56.1

The effects of cross shaped hole resonator (Figure 8-1b) are given in Table8-2. For this investigation, the length of the strip has been varied. The maximum absorptivity is observed when the length becomes to 90 nm. However the rate is almost constant between 90 nm and 100 nm. The dependence of the absorption rate to this geometric shape and the strip length dimensions are not high. The enhancement in the absorption at its highest value is 1.3% with respect to the reference value.

Table 8-2. The absorption rates over whole spectrum for various strip lengths.

length of strip (nm)	0	50	90	100	150	200	250	300
Absorption Rate (%)	55.7	56.0	56.4	56.4	56.3	56.2	55.9	55.4

Lastly the triangular shape is applied for reshaping method. Triangular shape is preferred as it has the same shape with the front resonators. The results of the calculations for various side length of the triangles are represented in Table 8-3. When compared with the reference absorption rates the total absorption rates are constantly increasing until the side length dimension reaches to 140 nm. The newly occurred shape causes new interaction between the back metallic plate and the silicon layer so that the total absorption rates increases. The highest absorption rate is obtained when the side length is 140 nm. At this length, the enhancement in the absorption is 2.9% with respect to the reference absorption rate. However, when the side length of the triangular hole is 150nm and above, the transmission increases due to the enlarged hole dimensions. This increment give rise to the decreasing of the absorption rates.

According to the results obtained in this section, square shape hole provides the highest enhancement in the absorption rate. The enhancement rates provided by square, cross and triangular hole shapes are 3.2%, 1.3%, and 2.9 % respectively.

Table 8-3. The absorption rates over whole spectrum for various side lengths of triangles.

Side Length of Triangle (nm)	0	20	40	60	80	100	120	140	150	160	180
Absorption Rate (%)	55.7	55.9	56.1	56.5	56.8	56.9	57.1	57.3	56.6	56.0	54.4

### 8.3. Graphene

Graphene is special form of the carbon atoms which exhibit strange and promising properties [100]. After the discovery of this material in the year 2004, electrical properties, optical characteristics thermal features and mechanical properties shows promising results for the application in optical an terahertz realms [101]. This material is composed of properly arranged carbon atoms with the depth of one atomic height. Hence it shows 2 -dimensioned structure and can be obtained as layers. One layer of this material has about 0.335 nm height [102].

Graphene supports plasmonics. Thus it can be a good candidate for the applications at higher frequencies where the surface plasmon polaritons are useful and necessary. For photovoltaic applications, the stimuli of these plasmonics can create new responses and can enhance the currently occurred absorption responses. Therefore, in this chapter, it has been decided to be apply and analyze the performance of graphene for photovoltaic applications. However as mentioned before, the suitability of graphene for this applications rely on the structure of absorber itself and the place of the structure that it has been utilized.

For introducing the graphene material into the simulation software, the surface conductivity of this material has been used which can be found by the known formulae of Kubo [60]. This relation gives both the real and imaginary parts of the conductivity where the contributions of inter and intra band relations are considered (equation (8-1)). The surface conductivity presented in Equation (8-1) depends on the angular frequency,  $\omega$ , Fermi energy,  $E_F$ , the rate of scattering,  $\tau$ , and the temperature, T. The expanded form of Equation (8-1) is represented in Equation (8-2). Here  $f_d$  is being the Fermi-Dirac distribution and can be calculated by  $f_d(\varepsilon) =$

$\left( e^{\frac{(1+e^{\varepsilon-E_F})}{k_B T}} \right)^{-1}$ . In this study the temperature of graphene sheet is assumed to be the room temperature of 300 K.

$$\sigma(\omega, E_F, \tau, T) = \sigma_{intra}(\omega, E_F, \tau, T) + \sigma_{inter}(\omega, E_F, \tau, T) \quad (8-1)$$

$$\sigma(\omega, E_F, \tau, T) = \frac{ie^2(\omega - j2\tau)}{\pi \hbar^2} \left( \frac{1}{(\omega - 2j\tau)^2} \int_0^\infty \varepsilon \left( \frac{df_d}{d\varepsilon} - \frac{df_d(-\varepsilon)}{d\varepsilon} \right) d\varepsilon - \int_0^\infty \frac{f_d(-\varepsilon) - f_d(\varepsilon)}{(\omega - 2j\tau)^2 - 4\left(\frac{\varepsilon}{\hbar}\right)^2} d\varepsilon \right) \quad (8-2)$$

In order to investigate the effects of graphene, it is applied to the different regions of the structure as given in Figure 8-2. Firstly, graphene is applied on the top of the structure covering all the areas (Figure 8-2a). Later, in order to investigate the differences between the effects of applying graphene onto silicon and applying it onto the silver, it is applied only on the a-Si layer on the top of the structure. (Figure 8-2b). For each of the cases, the number of applied graphene layers are altered and the variation of the absorption spectrum and the absorption rates are observed.

As mentioned before, the thickness of one sheet of graphene layer is 0.335 nm. Therefore the used layers here will be the multiply of 0.335 nm. In this study, the analyses is carried out for maximum 10 layers of graphene sheets.

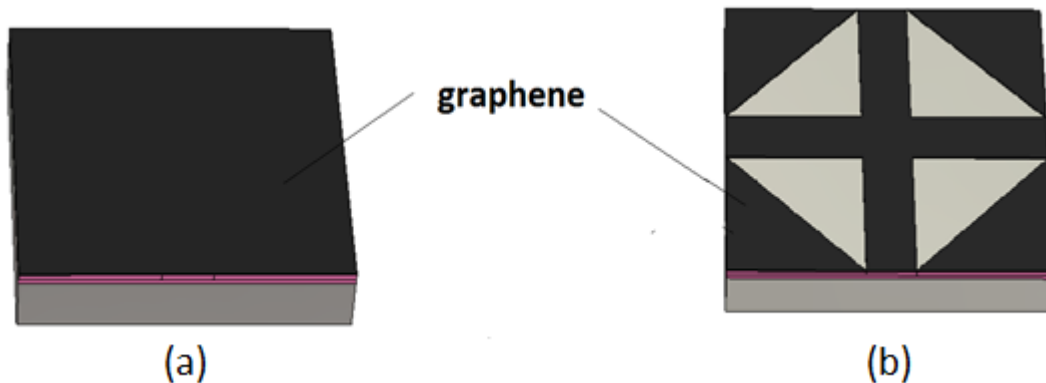


Figure 8-2. The place and the geometric structure of the applied graphene. (a) First design, (b) Second design.

The results for the structure given in Figure 8-2a are provided in Table 8-4. This table represents the absorption rates for various number of graphene sheets. All of the rates are calculated over whole absorption spectrum which takes between 300 THz and 1000 THz. The rates before graphene layers have been applied is indicated by the “zero graphene layer” in Table 8-4. These rates are the reference numbers and will be used for the indication of the enhancement in the absorption rates when graphene layers are applied. The result indicates that the total absorption rates are constantly increasing up to 8 layers. However, the rates are almost constant for 9<sup>th</sup>, and 10<sup>th</sup> layers. When above 10 layers was applied, the rates start to decrease. This is because of the damping of the plasmonic responses provided by the graphene sheets up to the 8th layer. The enhancement capability of graphene for this application is 15.9% when 8 layer was applied. The analysis show that, it is not practical to use more than 8 layers of graphene for this application as the highest rate is obtained at 8 layers. The enhancement capability onto the absorption spectrum of the graphene layers are visible in Figure 8-3. It is observed that applying graphene layer does not much affect the dual band resonances. However it enhanced the absorption level of the spectrum at around 300-350 THz and also it provided a new resonance at around 830 THz.

Table 8-4. The absorption rates over whole spectrum for various number of graphene layers. The rates are given for the fully graphene covered structure (Figure 8-2a).

<b># of graphene layers</b>	<b>0</b>	<b>1</b>	<b>2</b>	<b>3</b>	<b>4</b>	<b>5</b>	<b>6</b>	<b>7</b>	<b>8</b>	<b>9</b>	<b>10</b>	<b>11</b>	<b>12</b>
<b>Absorption rate (%)</b>	55.7	58.9	60.9	62.0	62.4	63.0	63.4	63.6	64.6	64.4	64.4	64.3	64.0

The second investigation for graphene is the analysis of structure given in Figure 8-2b. The only difference from Figure 8-1a is that: there is no graphene layer onto the isosceles triangular silver resonators. This type of graphene structure is used in order not to prevent the plasmonic response provided by the silver. The Variation of the absorption spectra according to the number of graphene layer used as well as data for the absorption rates for various number of graphene sheets are presented. The enhancement capability onto the absorption spectrum of the graphene layers are visible in Figure 8-3. It is observed that applying graphene layer does not much affect the dual

band resonances. However it enhanced the absorption level of the spectrum at around 300-350 THz and also it provided a new resonance at around 830 THz. The absorption rates for this application are provided in Table 8-5. Similar behaviors in terms of the absorption characteristics and absorption rates are obtained by the previous graphene application. The enhancement capability of graphene for this application is 15.9%.

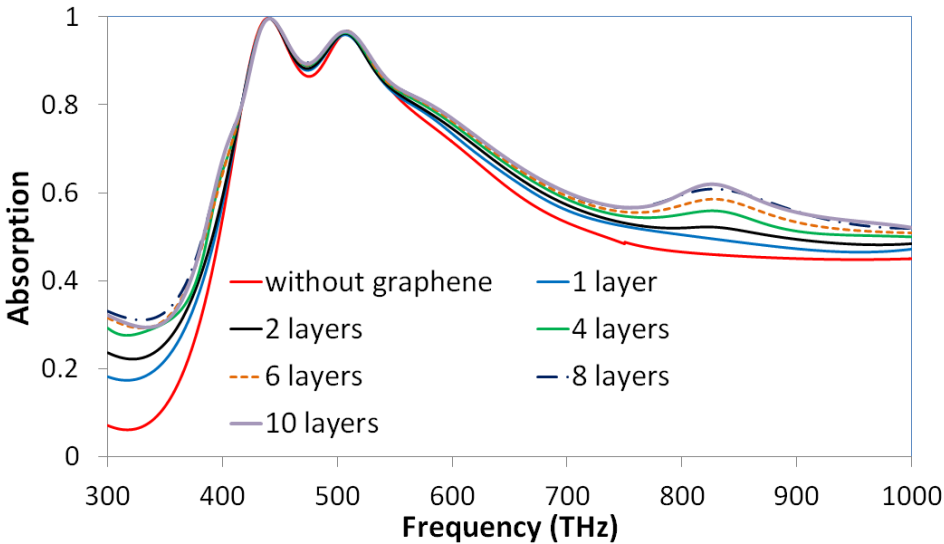


Figure 8-3. Variation of the absorption spectra according to the number of graphene layer used.

Table 8-5. The absorption rates over whole spectrum for various number of graphene layers. The rates are given for the partially graphene covered structure (Figure 8-2b).

# of graphene layers	0	1	2	3	4	5	6	7	8	9	10	11	12
Absorption Rate (%)	55.7	58.8	60.4	61.2	62.4	63.1	63.5	63.9	64.6	64.5	64.5	64.3	64.1

**8.4.Indium Tin Oxide**

The usage of the Indium tin oxide (ITO) acts as an interference layer for the incident radiation. Under this circumstance, the incident radiation finds new places to interfere with the absorber structure. Moreover, it also supports the surface plasmon polaritons [103]. ITO is a low loss material in the visible frequency region which means that it is optically transparent in the mentioned range [104]. Due to The optical characteristics (being transparent) and, electrical properties (high conductivity) of ITO, it is a preferred material for many application [105,106]. It has been using for solar cells as

transparent conductive oxides (TCO), solar collectors, windows etc. Therefore ITO might be a promising candidate for the applications for photovoltaic for enhancement of the absorption rates.

ITO was applied to the mentioned structure for two different cases which are illustrated in Figure 8-4. First case is the application of the ITO only at the top of the design (see Figure 8-4a). The observations are achieved by varying the depth of this material for the mention case. The second condition includes both the usage of the ITO by replacing the a-Si layer just near the triangular Ag plate and applying the ITO layer at the top of structure. The second condition is illustrated in Figure 8-4b. Note that, only the a-Si layer with the thickness of “t” ( $t=10$  nm) has been removed. The a-Si layer which takes place under the Ag resonators are remained as it was.

The variation of the absorption spectrum for the first case (Figure 8-4a) is demonstrated in Figure 8-5. The results indicates that the ITO has the grate enhancement capacity to the total absorption. As the thickness of applied layer are increase, the absorption response also get higher for absorption. However, in order to analyze the results in a more detailed way, it is better to check the absorption rates. The calculated rates for this conditions are presented in Table 8-6. In this case the great enhancement are observed in the total absorption when compared with the previously analyzed graphene and the reshaping methods. Moreover, the obtained values are also much higher than the reference rates. The optimum thickness for the ITO layer for this condition is 35 nm. For this case the interference and plasmonic occurred in a contractive way so that the maxima in the results are obtained.

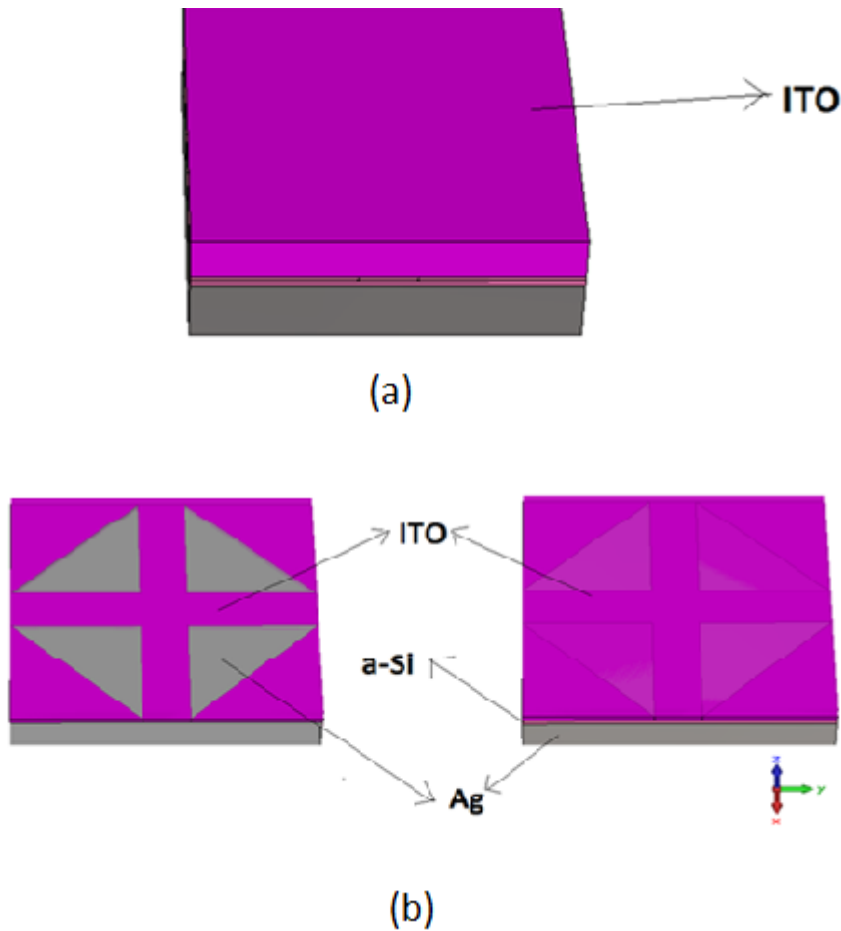


Figure 8-4. Illustration of the design after the usage of ITO layer. (a) Presence of ITO only the top of the design, (b) Simultaneously presence of ITO between the resonators and on the top of the design.

Moreover, the analysis of the absorption band given in Figure 8-5, show that when the depth of the ITO is 35 nm, 111 THz of wide absorption band with more than 90% is obtained in the visible frequency realm while in the ultraviolet range 205 THz of wide absorption band with more than 90% is obtained

The results for the second case where ITO was applied both near the silver resonators and on the top of the design are presented in Figure 8-6 and Table 8-7. Note that the depth of ITO layer provided in these results represent the thickness of the ITO which is placed on the top of the structure. It does not consist the thickness of the “ $t=10\text{ nm}$ ” which takes place between the silver resonators. According to the obtained results, the greatly enhancement in the absorption rates are obtained especially when the thickness of ITO is selected to be 30nm.

Among all of the techniques used in this chapter, ITO is the best option when the absorption rates are considered. The results show the best absorption rates when ITO is only applied to the top of the design (Figure 8-4a). The total absorption rate is found 81.5% where the optimum thickness of the ITO layer is obtained as 35 nm. Applying a 35 nm ITO layer, enhanced the absorption by 48.5% with respect to the reference rates.

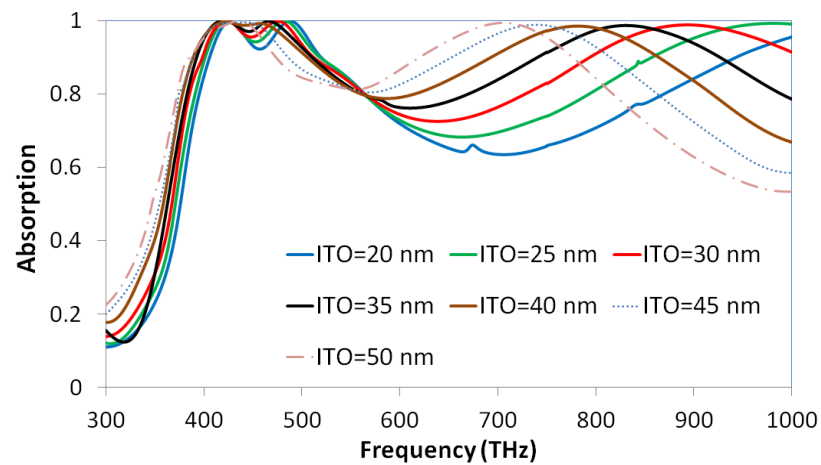


Figure 8-5. Variation of the absorption spectra according to the depth of ITO layer when ITO was utilized only the top of the design (Figure 8-4a).

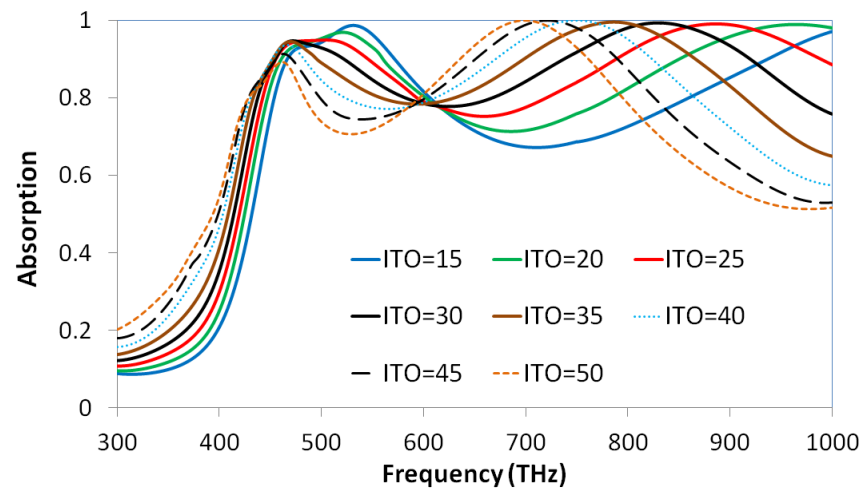


Figure 8-6. Variation of the absorption spectra according to the depth of ITO layer when ITO was utilized both on the design and between the resonators (Figure 8-4b).

Table 8-6. The absorption rates over whole spectrum for various ITO layer thicknesses. The rates are given for the design presented in Figure 8-4a.

<b>Thickness of ITO layer (nm)</b>	<b>15</b>	<b>20</b>	<b>25</b>	<b>30</b>	<b>35</b>	<b>40</b>	<b>45</b>	<b>50</b>
<b>Absorption Rate (%)</b>	67.57	73.3	78.2	81.5	82.2	82.2	80.6	78.7

Table 8-7. The absorption rates over whole spectrum for various ITO layer thicknesses. The rates are given for the design presented in Figure 8-4b.

<b>Thickness of ITO layer (nm)</b>	<b>15</b>	<b>20</b>	<b>25</b>	<b>30</b>	<b>35</b>	<b>40</b>	<b>45</b>	<b>50</b>
<b>Absorption Rate (%)</b>	69.0	73.5	76.0	76.5	75.5	73.9	71.8	69.9

## 8.5. Conclusion

As a conclusion, in this part, some of the absorption enhancement techniques are applied for the design provided in the previous chapter which can be utilized for photovoltaic applications. The results shows that each of the methods applied here has the capacity to enhance the absorption rates.

Among all the methods reshaping the back metallic plate has the minimal effects of increasing the total absorption rates.

Using graphene in the structure of the design also provides same improved results. However, the place of the application and the shape of the graphene is very important and directly effects the absorption rates of the absorber.

Among all the techniques, ITO provides the best absorption rates. It increased the absorption by 48.2%.

## CHAPTER 9

### CONCLUSION

#### 9.1. The Conclusion of the Thesis

One of the most popular and preferred energy source is the solar energy. This source can be used to supply clean and energy by the utilization of the solar cells. Photovoltaics and termo-photovoltaics being the two different forms of the solar cells which can be harvest the solar energy. However, the cost of these cells and the efficiency of these devices are the major difficulties that hinder this technology of becoming widespread. Metamaterial absorbers with their compact structure offer high efficiencies with the smaller unit cell dimensions and hence the lesser material costs. The existing metamaterial absorbers in the literature are general single and narrow band absorbers. In addition, there not much effort have been spent for the utilization of the higher frequencies (visible and ultraviolet).

In the beginning of the thesis, a single band absorber is introduced which is the combination of the strip type resonators. Although being a single band absorber, it has a wide half power bandwidth of 22.2%. Later, the dual band absorption is obtained by improving the strip type resonator. The main aim of the thesis which is obtained multiband absorption is formed by setting the topology in the solar spectrum is presented in chapter 5.

Two types of solar cell technology used in thesis to harvest energy is the PV and TPV. A multi band metamaterial absorber for TPV is introduced in chapter 6. The analysis of this device show that it has a polarization insensitive characteristics over the solar spectrum and it shows triple band response in the solar spectrum with the absorption rates higher than 90%. Moreover the theoretical validation is also carried out in order to validate the numerical results.

Dual band metamaterial absorber which has the capability to be used for PV applications is discussed and a new design is introduced in chapter 7. The polarization characteristics are analyzed while the geometric parameter dependencies and partial absorption rate of active material are also provided.

The enhancement of the absorption capacity of the devices is a critical issue for the improving the efficiencies of the designed structures. Therefore, in chapter 8 the improvement techniques are introduced and implemented to the design given in chapter 7. The results show that the improvement technologies have the functionality for improving the total absorption capability of the metamaterial absorber. The best improvement technique is found as applying ITO layer on to the top of the design. For the design presented in chapter 7, the enhancement of ITO is found as 48.5% when compared to the initial design.

Some of the results reported in this thesis have been presented in Turkish Physical Society 31<sup>th</sup> physic conference. Two journal papers from this thesis were published in Waves in Random and Complex Media journal and Plasmonics journal.

## **9.2. Future work**

In this thesis, numerical and theoretical analysis of metamaterial absorber designs were carried out. However, efficiency analysis of the designed metamaterial absorber models, implementation of the designed models into the solar cells for practical applications, and the experimental characterizations should be done as the future work.

## BIBLIOGRAPHY

- [1] Energy Matters: Global Energy Trends – BP Statistical Review 2014 [Internet]. 2014 August 27. Available from: <http://euanmearns.com/global-energy-trends-bp-statistical-review-2014>
- [2] S. Manabe, R. T. Wetherald. The Effects of Doubling the CO<sub>2</sub> Concentration on the climate of a General Circulation Model. *Journal of Atmospheric. Sciences.* 32(1975) 3-15.
- [3] M. I. Aslam, S. M. Ali. A Wideband Metamaterial Absorber for Solar Cell Applications. *Proceeding of International Conference on Energy and Sustainability;* Ned University of Engineering & Technology; Karachi Pakistan; 2013.
- [4] G. Hashmi, M. H. Imtiaz, S. Rafique. Towards High Efficiency Solar Cells: Composite Metamaterials. *Global Journal of Researches in Engineering Electrical and Electronics Engineering.* 13 (2013) 11-16.
- [5] F. Dincer, O. Akgol, M. Karaaslan, E. Unal, C. Sabah. Polarization angle independent perfect metamaterial absorbers for solar cell applications in the microwave, infrared, and visible regime. *Progress in Electromagnetics Research.* 144 (2014) 93-101.
- [6] Our Interesting Sun [Internet]. 2016 July 23. Available at [http://www.solarsystemcentral.com/sun\\_page.html](http://www.solarsystemcentral.com/sun_page.html)
- [7] L. Huang and H. Chen. Multi-band and polarization insensitive metamaterial absorber. *Progress in Electromagnetics Research.* 113 (2011) 103-110.
- [8] A. Vora, J. Gwamuri , N. Pala , A. Kulkarni , J. M. Pearce and D. Ö . Güney. Exchanging Ohmic Losses in Metamaterial Absorbers with Useful Optical Absorption for Photovoltaics. *Scientific Reports.* 4 (2014) 490. DOI:10.1038/srep04901
- [9] Y. Ra'di, C. R. Simovski, and S. A. Tretyakov. Thin Perfect Absorbers for Electromagnetic Waves: Theory, Design, and Realizations. *Physical Review Applied.* 3 (2015) 037001.
- [10] W. Withayachumnankul and D. Abbott, Metamaterials in the Terahertz Regime. *IEEE Photonics Journal.* 1 (2009) 99-118
- [11] J. Valentine, S. Zhang, T. Zentgraf, E. Ulin-Avila, D. A. Genov, G. Bartal and X. Zhang. Three-dimensional optical metamaterial with a negative refractive index. *Nature* 455 (2008) 376-379. Doi: 10.1038/nature07247;
- [12] W. J. Padilla, D. N. Basov, D. R. Smith. Negative refractive index metamaterials. *Materials Today.* 9 (2006) 28-35

- [13] V. M. Shalaev. Optical negative-index metamaterials. *Nature Photonics*. 1 (2007)41-48.
- [14] C. M. Watts, X. Liu, and W. J. Padilla. Metamaterial Electromagnetic Wave Absorbers. *Advance. Materials*.24 (2012), OP98–OP120
- [15] D. Schurig, J. J. Mock, B. J. Justice, S. A. Cummer, J. B. Pendry, A. F. Starr, D. R. Smith. Metamaterial Electromagnetic Cloak at Microwave Frequencies. *Science*. 314 (2006) 977-980.
- [16] V. G. Vesalago, P. N. Labedev. The electrodynamics of substances with simultaneously negative values of  $\epsilon$  and  $\mu$ . *Soviet Physics Uspekhi*. 10 (1968) 509-514.
- [17] W. Cai and V. Shalaev *Optical Metamaterials Fundamentals and Applications* 2010 Springer New York Dordrecht Heidelberg London.
- [18] T. S. Almoneef and O. M. Ramahi. Metamaterial electromagnetic energy harvester with near unity efficiency. *Applied Physics Letters* 106 (2015) 153902-1-153902-4.
- [19] N. I. Landy, S. Sajuyigbe, J. J. Mock, D. R. Smith, and W. J. Padilla, Perfect Metamaterial Absorber, *Physical Review Letters*. 100 (2008) 207402.
- [20] J. Hao, L. Zhou, and M. Qiu, Nearly total absorption of light and heat generation by plasmonic metamaterials, *Physical Review B*. 83, 165 (2011)107.
- [21] R. Feng, J. Qiu, Y. Cao, L. Liu, W. Ding and L. Chen, Wide-angle and polarization independent perfect absorber based on one-dimensional fabrication tolerant stacked array, *Optics Express*. 23 (2015) 21023 DOI:10.1364/OE.23.021023
- [22] Y. J. Kim, Y. J. Yoo, K. W. Kim, J. Rhee, Y. H. Kim, and Y. Lee, Dual broadband metamaterial absorber, *Optics Express*. 23(2015), 3861 DOI:10.1364/OE.23.003861
- [23] X. Liu, T. Starr, A. F. Starr, and W. J. Padilla. Infrared Spatial and Frequency Selective Metamaterial with Near-Unity Absorbance. *Physical Review Letters*. 104 (2010)207403-1 - 207403-4
- [24] A. Agrawal, A. Singh and M. Misra. A Multiband Metamaterial Absorber with Concentric Continuous Rings Resonator Structure. *International Journal of Advances in Microwave Technology*. 1 (2016) 5-9.
- [25] Z. Mao, S. Liu, B. Bian, B. Wang, B. Ma, L. Chen, and J. Xu .Multi-band polarization-insensitive metamaterial absorber based on Chinese ancient coin-shaped structures *Journal of Applied Physics*. 115 (2014) 204505.
- [26] W. Qin, J. Wu, M. Yu, and S. Pan. Dual-band terahertz metamaterial absorbers using two types of conventional frequency selective surface elements *Terahertz Science and Technology*. 5 (2012) 169-174.

- [27] C. Sabah, Metamaterial Absorber Based Multifunctional Sensors. *Journal of the Electrochemical Society*. 163 (7) (2016) B319-B324.
- [28] C. Sabah, F. Dincer M. Karaaslan, E. Ünal, O. Akgöl, E. Demirel, Perfect metamaterial absorber with polarization and incident angle independencies based on ring and cross-wire resonators for shielding and a sensor application. *Optics communication*. 332 (2014) 137-142.
- [29] M. Kafesaki, N. H. Shen, S. Tzortzakis and C. M. Soukoulis. Optically switchable and tunable terahertz metamaterials through photoconductivity. *Journal of Optics*. 14 (2012) 114008.
- [30] J.Y. Rhee, Y.J. Yoo, K.W. Kim, Y.J. Kim & Y.P. Lee. Metamaterial-based perfect absorbers. *Journal of Electromagnetic Waves and Applications*. 28 (2014) 1541–1580.
- [31] J. Yoon, M. Zhou, Md. A. Badsha, T. Y. Kim, Y. C. Jun and C. K. Hwangbo. Broadband Epsilon-Near Zero Perfect Absorption in the Near-Infrared. *Scientific Reports*. 5 (2015) 12788.
- [32] H. Li, L. H. Yuan, B. Zhou, X. P. Shen, Q. Cheng, and T. J. Cui. Ultrathin multiband gigahertz metamaterial absorbers. *Journal of Applied Physics*. 110 (2011) 014909-1-8.
- [33] B. Zhu, Z. Wang, C. Huang, Y. Feng, J. Zhao, and T. Jiang. Polarization Insensitive Metamaterial Absorber with Wide Incident Angle. *Progress in Electromagnetics Research*. 101 (2010) 231–239.
- [34] K. Wu, Yo. Huang, T. Wanghuang, W. Chen, and G. Wen. Numerical and theoretical analysis on the absorption properties of metasurface-based terahertz absorbers with different thicknesses. *Applied Optics*. 54 (2015) 299.
- [35] R. F. Huang, Z. W. Li, L. B. Kong, L. Liu, and S. Matitsine. Analysis and Design of an Ultra-Thin Metamaterial Absorber. *Progress in Electromagnetics Research B*. 14 (2009) 407–429.
- [36] HT. Chen, J. F. O’Hara, A. K. Azad, and A. J. Taylor. Manipulation of terahertz radiation using metamaterials. *Laser Photonics Rev*. 5 (2011) 513–533.
- [37] X. Liu, T. Tyler, T. Starr, A. F. Starr, N. M. Jokerst and W. J. Padilla. Taming the Blackbody with Infrared Metamaterials as Selective Thermal Emitters. *Physical Review letters*. 107 (2011) 045901-1-4.
- [38] F. Ding, Y. Cui, X. Ge, Y. Jin, and S. He. Ultra-broadband microwave metamaterial absorber. *Applied Physics Letters*. 100 (2012) 103506-1.
- [39] S. Gu, J. P. Barrett, T. H. Hand, B.-I. Popa, and S. A. Cummer. A broadband low-reflection metamaterial absorber. *Journal of Applied Physics*. 108 (2010) 064913-1-6

- [40] B. Wang T. Koschny and C. M. Soukoulis. Wide-angle and polarization-independent chiral metamaterial absorber. *Physical Review B*. 80 (2009) 033108-1-4
- [41] S. V. Boriskina, H. Ghasemi and G. Chen. Plasmonic materials for energy: From physics to applications. *Materials Today*. 16 (2013)
- [42] L. DeSio, T. Placido, R. Comparelli, M. L. Curri, M. Striccoli, N. Tabiryan, T. J. Bunning. Next-generation thermo-plasmonic technologies and plasmonic nanoparticles in optoelectronics. *Progress in Quantum Electronics*. 41(2015)23–70.
- [43] K. Yao and Y. Liu. Plasmonic metamaterials. *Nanotechnology Reviews* 3(2) (2014) 177–210.
- [44] C. Wu, B. Neuner, J. John, A. Milder, B. Zollars, S. Savoy and G. Shvets. Metamaterial-based integrated plasmonic absorber/emitter for solar thermo-photovoltaic systems *Journal of Optics*. 14 (2012) 024005.
- [45] C. Shemelya, D. DeMeo, N. P. Latham, X. Wu, C. Bingham, W. Padilla, and T. E. Vandervelde. Stable high temperature metamaterial emitters for thermophotovoltaic applications. *Applied Physics Letters*. 104 (2014) 201113.
- [46] S. Ayas, G. Bakan, and A. Dana. Rounding corners of nano-square patches for multispectral plasmonic metamaterial absorbers. *Optics Express*. 23 (2015) 11763.
- [47] K. Liu, S. Jiang, D. Ji, X. Zeng, N. Zhang, H. Song, Y. Xu, and Q. Gan. Super Absorbing Ultraviolet Metasurface. *IEEE Photonics Technology Letters*. 27(2015)1539.
- [48] Q. Liang, W. Yu, W. Zhao, T. Wang, J. Zhao, H. Zhang, and S. Tao. Numerical study of the meta-nanopyramid array as efficient solar energy absorber. *Optic Material Express*. 3(2013) 1187
- [49] J. Wu, C. Zhou, J. Yu, H. C. S. Li, W. Jia. TE polarization selective absorber based on metal-dielectric grating structure for infrared frequencies. *Optics communication*. 329 (2014) 38
- [50] B. Paridaa, S. Iniyamb, R. Goicc. A review of solar photovoltaic technologies. *Renewable and Sustainable Energy Reviews*. 15 (2011) 1625–1636
- [51] B. M. Kayes and H. A. Atwater. Comparison of the device physics principles of planar and radial p-n junction nanorod solar cells. *Journal of Applied Physics*. 97(2005) 114302-1-11.
- [52] M. Dhankhar, O. P. Singh, V.N. Singh Physical principles of losses in thin film solar cells and efficiency enhancement methods. *Renewable and Sustainable Energy Reviews*. 40 (2014) 214–223.
- [53] E. Klampaftisa, D. Rossa, K. R. McIntoshb and B. S. Richardsa. Enhancing the performance of solar cells via luminescent down-shifting of the incident spectrum: A review. *Solar energy materials and solar cells*. 93 (2009) 1182-1194.

- [54] M. A. Green . Third generation photovoltaics: solar cells for 2020 and beyond. *Physica E: Low-dimensional Systems and Nanostructures*. 14 (2002) 65–70.
- [55] H. A. Atwater and A. Polman. Plasmonics for improved photovoltaic devices. *Nature Materials*. 9 (2010) 205-213.
- [56] D. Sievenpiper, L. Zhang, R. F. J. Broas, N. G. Alexopolous, and E. Yablonovitch. High-Impedance Electromagnetic Surfaces with a Forbidden Frequency Band. *IEEE Transactions on Microwave Theory and Techniques*. 47 (1999) 2059-2074.
- [57] A. Vial, T. Laroche, M. Dridi, and L. L. Cunff. A new model of dispersion for metals leading to a more accurate modeling of plasmonic structures using the FDTD method. *Applied Physics A*. 103 (2011) 849. DOI: 10.1007/s00339-010-6224-9
- [58] K. R. Catchpole and A. Polman. Design principles for particle plasmon enhanced solar cells. *Applied Physics Letters*. 93 (2008) 191113-1-191113-3.
- [59] K. H. Lee, I. Ahmed, R. S. M. Goh, E. H. Khoo, E. P. Li, and T. G. G. Hung. Implementation Of The FDTD Method Based on Lorentz-Drude Dispersive Model On GPU for Plasmonics Applications. *Progress in Electromagnetics Research*. 116 (2011) 441–456.
- [60] Q. Zhang, Q. Ma, S. Yan, F. Wu, X. He, J. Jiang. Tunable terahertz absorption in graphene-based metamaterial. *Optics Communications* 353(2015)70–75.
- [61] S. Walia, C. M. Shah, P. Gutruf, H. Nili, D. R. Chowdhury, W. Withayachumnankul, M. Bhaskaran, and S. Sriram. Flexible Metasurfaces and Metamaterials: A Review of Materials and Fabrication Processes At Micro- and Nano-Scales. *Applied Physics Reviews* 2 (2015) 011303 1-14.
- [62] M. Gil, J. Bonache, F. Martín. Metamaterial filters: A review. *Metamaterials*. 2 (2008) 186–197
- [63] C. Long, S. Yin, W. Wan, W. Li, J. Zhu, and J. Guan. Broadening the Absorption Bandwidth of Metamaterial Absorbers by Transverse Magnetic Harmonics of 210 Mode. *Scientific Reports*. 6 (2016)21431- 1-9 DOI: 10.1038/srep21431.
- [64] D. Wen, H. Yang, Q. Ye, M. Li, L. Guo and J. Zhang. Broadband Metamaterial Absorber Based On A Multi-Layer Structure. *Physica Scripta*. 88 (2013) 015402 (7pp).
- [65] S. Kawata and V. M. Shalaev. Tip enhancement. *Advances in nano-optics and nano-photonics*. Elsevier: New York; 2007.
- [66] S. Jahani and Z. Jacob. Photonic skin-depth engineering. *J. Opt. Soc. Am. B*, 32(2015)1346-1353.

- [67] P. W. Gilberd. The anomalous skin effect and the optical properties of metals. *J. Phys. F: Met. Phys.*, 12(1982)1845-1860.
- [68] K. M. Lebecki, M. J. Donahue and M. Gutowski. Periodic Boundary Conditions for Demagnetization Interactions in Micromagnetic Simulations. *Journal of Physics D: Applied Physics*. 41 (2008) 175005 (10pp)
- [69] P. Harms, R. Mittra and W. KO. Implementation of the Periodic Boundary Condition in the Finite-Difference Time-Domain Algorithm for FSS Structure. *IEEE Transactions on Antennas and Propagation*. 42 (1994). 1317-1324.
- [70] C.P. Huang and Y.Y. Zhu. Plasmonics: Manipulating Light at the Subwavelength Scale. *Active and Passive Electronic Components*. 2007 (2007)1-13.
- [71] Guy A. E. Vandenbosch and Alexander Vasylychenko (2011). A Practical Guide to 3D Electromagnetic Software Tools, Microstrip Antennas, Prof. Nasimuddin Nasimuddin (Ed.), Intech, DOI: 10.5772/14756
- [72] H. F. Álvarez, M. E. de C. Gómez and F. Las-Heras. A Six-Fold Symmetric Metamaterial Absorber. *Materials*. 8 (2015) 1590-1603.
- [73] L. Li, Y. Yang, and C. Liang. A wide-angle polarization-insensitive ultra-thin metamaterial absorber with three resonant modes. *Journal of Applied Physics*. 110 (2011) 063702-1-5
- [74] J. Zhong, Y. Huang, G. Wen et al. Single-/dual-band metamaterial absorber based on cross-circular-loop resonator with shorted stubs. *Applied Physics A*. 108 (2012) 329
- [75] J. Hao, Lei Zhou, and M. Qiu. Nearly total absorption of light and heat generation by plasmonic metamaterials. *Physical Review B*. 83 (2011) 165107-1-12.
- [76] Z. Rahimi. The Finite Integration Technique (FIT) and the Application in Lithography Simulations. Als Dissertation genehmigt von der Technischen Fakultät der Universität Erlangen-Nürnberg. 10. January, 2011.
- [77] K. S. Yee. Numerical solution of initial boundary value problems involving Maxwell's equations in isotropic media," *IEEE Transaction Antennas and Propagation*, 14(1966)302-307.
- [78] B. K. Li, F. Liu, and S. Crozier. High-Field Magnetic Resonance Imaging With Reduced Field/Tissue RF Artefacts—A Modeling Study Using Hybrid MoM/FEM and FDTD Technique. *IEEE Transactions on Electromagnetic Compatibility*. 48 (2006) 628-633.
- [79] W. Ross Stone. Review of Radio Science: 1999-2002. Chapter 11. The Finite Integration Technique as a General Tool to Compute Acoustic, Electromagnetic, Electrodynamic and Coupled Wave Fields René Marklein.

- [80] Hou-Tong Chen. Interference theory of metamaterial perfect absorbers. *Optics Express*. 20 (2012) 7165-7172.
- [81] T. Wanghuang, W. Chen, Y. Huang, and G. Wen. Analysis of metamaterial absorber in normal and oblique incidence by using interference theory. *American Institute of Physics Advances*. 3 (2013) 102118-1-8.
- [82] F. Dincer, M. Karaaslan, E. Unal, O. Akgol, and C. Sabah. Design of Polarization- and Incident Angle-Independent Perfect Metamaterial Absorber with Interference Theory. *Journal of Electronic Materials*. 43 (2014) 3949.
- [83] M. A. Ordal, L. L. Long, R. J. Bell, S. E. Bell, R. R. Bell, R. W. Alexander, Jr, C. A. Ward. Optical properties of the metals Al, Co, Cu, Au, Fe, Pb, Ni, Pd, Pt, Ag, Ti, and W in the infrared and far infrared. *Applied Optics*. 22(1983)1099-1120.
- [84] Edward D Palik. *Handbook of Optical Constant of Solids*. Academic press. 1985.
- [85] Y. Q. Zeng, J. Q. He, and Q. H. Liu. The Application of the Perfectly Matched Layer in Numerical Modeling of Wave Propagation in Poroelastic Media. *Geophysics*. 66 (2001) 1258–1266.
- [86] W. C. Chew, and Q. Liu. Perfectly matched layers for elastodynamics: A new absorbing boundary condition: *Journal of Computational Acoustics*. 4(1996) 341–359.
- [87] X. He, S. Yan, G. Lu, Q. Zhang, F. Wu and J. Jiang. Ultra-broadband polarization-Independent perfect absorber for solar spectrum. *RSC Advances*. 5 (2015) 61955-61959.
- [88] M. Li, HL. Yang, XW. Hou, Y. Tian, DY. Hou. Perfect metamaterial absorber with dual bands. *Progress in Electromagnetics Research*. 108 (2010)37-49.
- [89] F. Dincer, M. Karaaslan, E. Unal, K. Delihacioglu, C. Sabah. Design of polarization and incident angle insensitive dual band metamaterial absorber based on isotropic resonators. *Progress in Electromagnetics Research*. 144 (2014)123-132.
- [90] M. Diem, T. Koschny, CM. Soukoulis. Wide-angle perfect absorber/thermal emitter in the terahertz regime. *Physics Review*. (2009) B79:033101-1-033101-4 B79.
- [91] G. Dayal and S. Anantha Ramakrishna. Design of multi-band metamaterial perfect absorbers with stacked metal–dielectric disks. *Journal of Optics*. 15 (2013) 055106 (7pp).
- [92] J. Wang, C. Fan, P. Ding, J. He, Y. Cheng, W. Hu, G. Cai, E. Liang and Q. Xue. Tunable broad-band perfect absorber by exciting of multiple plasmon resonances at optical frequency. *Optics Express*. 20 (2012) 14871.

- [93] C. Sabah. Multiband Metamaterials based on Multiple Concentric open ring resonators topology. *IEEE Journals of Selected Topics in Quantum Electronics*. 9 (2013) 8500808.
- [94] K. Takano, Y. Chiyoda, T. Nishida, F. Miyamaru, T. Kawabata, H. Sasaki, M. W. Takeda, and M. Hangyo. Optical switching of terahertz radiation from meta-atom-loaded photoconductive antennas. *Applied Physics Letters*. 99 (2011) 161114-1-3.
- [95] M. A. Green. Third generation photovoltaics: ultrahigh conversion efficiency at low cost. *Progress in Photovoltaics: Research and Applications*. 9(2001) 123-135.
- [96] Y. Bai, L. Zhao, D. Ju, Y. Jiang, and L. Liu. Wide-angle, polarization-independent and dual band infrared perfect absorber based on L shaped metamaterial. *Optics Express*. 23(2015) 8670-80.
- [97] E. L. Green. Optical Properties of the Alpha-Phase Alloys Ag-Zn and Ag-Cd. *Physical Review B*. 2 (1970) 330-339.
- [98] N. Do, L. Klees, P. T. Leung, F. Tong, and W. P. Leung. Temperature dependence of optical constants for amorphous silicon. *Applied. Physics. Letters*. 60 (1992) 2186-2188
- [99] O. Yavas, N. Do, A. C. Tam, P. T. Leung, W. P. Leung, H. K. Park, C. P. Grigoropoulos, J. Boneberg, and P. Leiderer. Temperature dependence of optical properties for amorphous silicon at wavelengths of 632.8 and 752 nm. *Optics Letters* 18 (1993) 540-542.
- [100] Q. Li, Z. Tian, X. Zhang, N. Xu, R. Singh, J. Gu, P. Lv, LB. Luo, S. Zhang, J. Han. Dual control of active graphene–silicon hybrid metamaterial devices. *Carbon*. 90 (2015) 146-153.
- [101] X. He, ZY. Zhao, and W. Shi. Graphene-supported tunable near-IR metamaterials. *Optics Letters*. 40 (2015) 178-181
- [102] X. He. Tunable terahertz graphene metamaterials. *Carbon*. 82 (2015) 229-237.
- [103] S. Franzen. Surface Plasmon Polaritons and Screened Plasma Absorption in Indium Tin Oxide Compared to Silver and Gold. *The Journal of Physical Chemistry C*. 112 (2008) 6027-6032.
- [104] H. Kim and C. M. Gilmore A. Pique', J. S. Horwitz, H. Mattoussi, H. Murata, Z. H. Kafafi, and D. B. Chrisey. Electrical, optical, and structural properties of indium–tin–oxide thin films for organic light-emitting devices. *Journal of Applied Physics*. 86 (1999) 6451-6461.
- [105] T. Minami. Present status of transparent conducting oxide thin-film development for Indium-Tin-Oxide (ITO) substitutes. *Thin Solid Films* 516 (2008) 5822–5828.

[106] G.V. Naik, A. Boltasseva, A comparative study of semiconductor-based plasmonic metamaterials, *Metamaterials* 5 (2011) 1 – 7.